Visualizing the dynamics of ionotropic glutamate receptors using atomic force microscopy

Submitted for the Degree of Doctor of Philosophy

Mohammad Fahim Kadir

November 2017

Department of Pharmacology

University of Cambridge

Christ's College

Visualizing the dynamics of ionotropic glutamate receptors using atomic force microscopy

Mohammad Fahim Kadir

Abstract

Glutamate is the major excitatory neurotransmitter in the mammalian brain. It binds to three different subclasses of ionotropic glutamate receptors (iGluRs): AMPA, kainate and NMDA receptors, and triggers a cation influx that generates synaptic currents crucial to brain function. Significantly, iGluRs are implicated in various neurological disorders, such as depression, schizophrenia, Alzheimer's and Parkinson's diseases, autism, seizure, and stroke. The iGluR subunits are composed of modular domains - the amino-terminal domain (ATD), ligand-binding domain (LBD), transmembrane domain, and carboxy-terminal domain - and assemble into tetramers to form ligand-gated ion channels.

Several crystal structures for intact iGluRs in various functional states (i.e. closed, activated and desensitized) have now been reported. The receptors have also been studied using single-particle cryo-electron microscopy. Together, these studies provide fascinating 'snap-shots' of the receptors as they transition between different states. What is lacking, so far, is information about the kinetics underlying these structural transitions, because the techniques used lack time resolution.

I have used fast-scan atomic force microscopy (AFM), in some cases in combination with UV photolysis of caged L-glutamate, to study activation-induced structural changes in GluK2 kainate receptors and GluA2 AMPA receptors. AFM provides single-molecule resolution under fluid, permitting the imaging of proteins 'in action'. Receptors were purified from transfected cells by immunoaffinity chromatography and imaged after integration into supported lipid bilayers. Activation of both receptors caused a rapid ~1-nm vertical compression of the receptor. In both cases, the height reduction did not occur in the presence of receptor antagonists. Further, the D776K mutant of the kainate receptor, which does not desensitize, did not undergo the height change, and cyclothiazide, which blocks desensitization of the AMPA receptor, also blocked the height change. I conclude, therefore, that the vertical compression is

associated with receptor desensitization, and suggest that it may reflect a weakening of the interaction between receptor subunits at the LBD dimer interface.

When imaged from the 'top' by AFM, the receptors appeared as double-blob structures, with each blob representing a pair of ATDs. By measuring the distance between the centres of the blobs in successive AFM images, I was able to monitor the mobility of the ATDs relative to each other before and during receptor stimulation. I found that for both kainate and AMPA receptors, the relative mobility of the ATDs became greater after stimulation. Further, at low glutamate concentrations, the ATDs of the (rapidly desensitizing) flop splice variant of the AMPA receptor were more mobile than those of the (more slowly desensitizing) flip splice variant. I suggest that the greater mobility of the flop splice variant might be connected with its more short-lived functional response to activation.

In a final series of experiments, in collaboration with two other groups, I used AFM to measure conformational changes induced by allosterically-bound halide ions. We found that anion substitution (i.e. chloride to bromide, or chloride to iodide) produced vertical compression of AMPA receptors prior to agonist binding, and also (in electrophysiological experiments conducted by collaborators) altered the duration of agonist-evoked channel activity. The anion binding site was identified (in X-ray crystal structures obtained by collaborators) within the ligand binding domain, where flip-flop alternative splicing occurs. Interestingly both anion effects were isoform-dependent. Together, these results demonstrate that resting-state allosteric interactions can 'prime' AMPA receptors for their eventual response to agonists.

Overall, my results obtained using fast-scan AFM imaging provide fascinating new information about the global dynamics of these key neurotransmitter receptors.

Declaration

This dissertation is the result of my own work and includes nothing which is the outcome of work done in collaboration except the results depicted in Figure 5.3, which were provided by my collaborators, Dr. Derek Bowie (McGill University) and Dr. Jette Katstrup (University of Copenhagen).

It is not substantially the same as any that I have submitted, or, is being concurrently submitted for a degree or diploma or other qualification at the University of Cambridge or any other University or similar institution. I further state that no substantial part of my dissertation has already been submitted, or, is being concurrently submitted for any such degree, diploma or other qualification at the University of Cambridge or any other University or similar institution.

It does not exceed the prescribed word limit for the relevant Degree Committee.

Mohammad Fahim Kadir

November 2017

Acknowledgements

It is my pleasure to acknowledge the roles of several individuals who were instrumental for completion of my PhD thesis.

First of all, I would like to express my deepest gratitude to my supervisor Professor Mike Edwardson for his unwavering support and mentorship throughout this project. His skilful guidance, innovative ideas and stoic patience are greatly appreciated.

I would like to thank my colleagues Dr. Pia Jeggle and Dr. Ioanna Mela for their encouragement, endless help and comprehensive advice during the study. Many thanks to Dr. Robert Henderson and all members of the Edwardson group for their help and advice.

I am highly indebted to Camilo Navarrete, a visiting researcher for his creative ideas, as well as for providing the necessary mathematical analysis regarding this research.

My thanks and appreciation also goes to our collaborators Dr. Derek Bowie and Dr. Nelson Barrera, who have contributed to this project with their resources.

I would like to express my gratitude towards my family for their encouragement, which helped me in the completion of my PhD. I am thankful to my mother Joytsna Ara and father Md. Manzur-ul Kadir Mia for all of the sacrifices they have made for me. Words cannot express how grateful I am to my wife, Mishu who has loved and supported me throughout an extraordinary four years and my lovable daughter Zuhayera who served as my inspiration to pursue this journey.

Finally, I wish to thank to the Islamic Development Bank and the Cambridge Commonwealth Trust for their financial support.

Table of Contents

List of figures

Abbreviations

AFM	atomic force microscopy
ALS	amyotrophic lateral sclerosis
ASIC	acid-sensing ion channel
ATD	amino terminal domain
ATP	adenosine triphosphate
AMPAR	α-amino-3-hydroxy-5-methyl-4 isoxazolepropionic acid
BPC	biotechnology performance certified
cDNA	complementary deoxyribonucleic acid
CHAPS	3-[(3-cholamidopropyl) dimethylammonio]-1-
CNS	central nervous system
CTD	carboxyl-terminal domain
CTZ	cyclothiazide
DOPS	1,2-dioleoyl-*sn*-glycero-3-phospho-L-serine
ECL	enhanced chemiluminescence
EDTA	ethylenediaminetetraacetic acid
EM	electron microscopy
EPSP	excitatory postsynaptic potential
FITC	fluorescein isothiocyanate
GABA	γ-aminobutyric acid
HA	haemagglutinin
HEPES	4-(2-hydroxyethyl)-1-piperazineethanesulfonic acid
HBS	HEPES-buffered saline
HPI	hexagonally packed intermediate
HRP	horseradish peroxidase
$5HT_3$	5-hydroxytryptamine
iGluR	ionotropic glutamate receptor
IPSP	inhibitory postsynaptic potential
KAR	kainate receptor
LBD	ligand binding domain

MAPT	microtubule associated protein tau
mGluR	metabotropic glutamate receptor
MSD	mean squared displacement
nAChR	nicotinic acetylcholine receptor
NETO	neuropilin and tolloid-like
NMR	nuclear magnetic resonance
NMDAR	N-methyl-D-aspartate receptor
PAGE	polyacrylamide gel electrophoresis
PBS	phosphate-buffered saline
PC	L-α-phosphatidylcholine
PDB	protein data bank
PMSF	phenyl methyl sulphonyl fluoride
PSD	postsynaptic density
SAP	synapse-associated protein
SDS	sodium dodecyl sulphate
SEM	scanning electron microscopy
SMA	spinal muscular atrophy
SMN	survival of motor neurons
SNARE	soluble NSF attachment receptor
snRNP	small nuclear ribonucleoprotein
TARP	transmembrane AMPAR regulatory protein
TBS	tris-buffered saline
TEM	transmission electron microscopy
TMD	transmembrane domain

1. General introduction

1.1 Ion channels

Ion channels are transmembrane protein complexes that form water-filled pores across lipid bilayers through which specific inorganic ions such as Na^+, K^+, Ca^{2+}, or Cl^- can pass. The ions diffuse down their electrochemical gradients at rates about 1,000 times greater than those achieved by any known carrier (Alberts *et al.*, 2002). Ion channels are responsible for establishing a resting membrane potential, as well as generating action potentials and other electrical signals. They are also involved in controlling ion flow across secretory and epithelial cells, and in regulating cell volume (Hille, 2001).

Ion channels have three unique properties: ion selectivity, gating, and high-speed transportation. Typically, more than 10^6 ions per second pass through an open channel. Moreover, the channels are selective to ions of appropriate charge and size and usually open transiently in response to a specific stimulus (Cooper, 2000).

According to their gating behaviour, ion channels can be classified as either voltage-gated (e.g. voltage-gated Na^+ channel or voltage-gated K^+ channels) and ligand-gated (e.g. ionotropic glutamate receptors or ATP-gated P2X receptors). Passage of ions through voltage-gated channels depends on changes in membrane potential, whereas opening of ligand-gated channels depends on the binding of a ligand. Here I define 'ligand' as a chemical messenger that may be either extracellular (e.g. neurotransmitters) or intracellular (e.g. ions and nucleotides). Other notable types of ion channels are light-gated channels, mechanosensitive ion channels, temperature-gated channels (Fig. 1.1; Alberts *et al.*, 2002).

A single neuron typically contains at least ten types of ion channel. Using stochastic nonlinear dynamics, Buchholtz *et al.* (2002) counted ~14,000 ion channels in a local neuron and ~70,000 ion channels in a projection neuron. These huge numbers of neurons work together in complex ways to control the behaviour of electrically excitable cells.

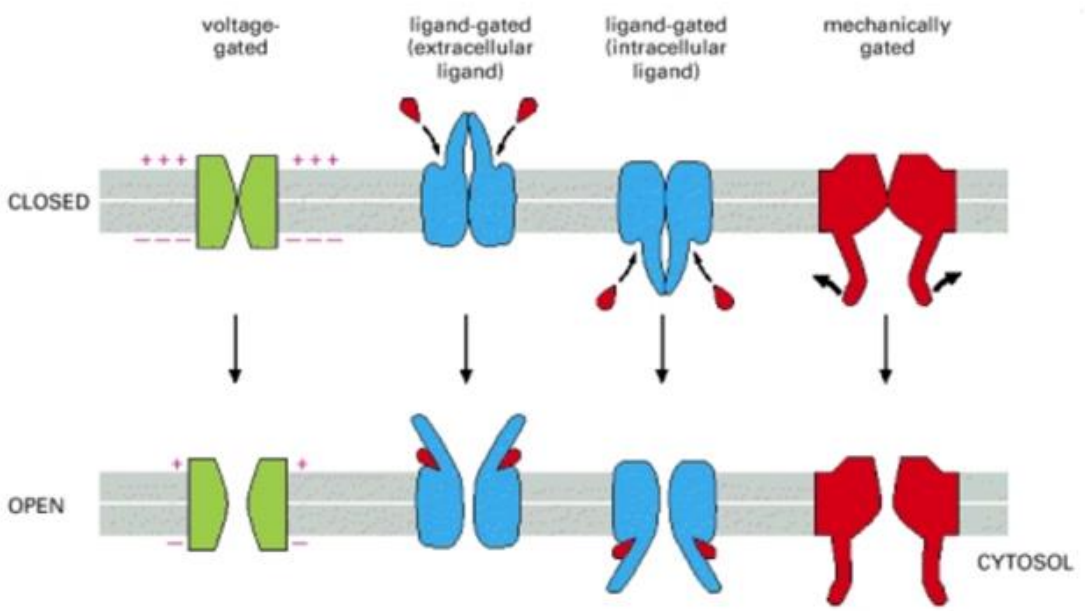

Figure 1.1. Ionic channel gating, showing different kinds of stimuli that open ion channels (Alberts *et al.*, 2002).

1.2 Synaptic transmission

Ionic composition and concentration are very different between intracellular and extracellular compartments. Specifically, Na^+, Cl^-, Ca^{2+} ion concentrations in the cytoplasm are much lower than in the extracellular compartment, whereas the K^+ ion concentration is much higher in the cytoplasm. These transmembrane differences in ionic concentrations of different ions in combination with the significant permeability of the membrane to K^+ ions at rest, generates a resting membrane potential close to the K^+ equilibrium potential (typically about -70 mV).

Synaptic transmission between a pre- and a postsynaptic neuron is initiated by the opening of voltage-gated Na^+ channels in the presynaptic nerve terminal caused by an action potential arriving down from presynaptic axon. The resulting membrane depolarization results in the opening of voltage-gated Ca^{2+} channels which allows Ca^{2+} ions to enter the presynaptic nerve terminal. The neuronal Ca^{2+} sensor synaptotagmin, located on the membrane of the synaptic vesicles, then interacts with SNARE proteins, triggering fusion of the synaptic vesicles with the presynaptic membrane. In this way neurotransmitters are released by exocytosis into the synaptic cleft (Purves *et al.*, 2008).

Once released in the synaptic cleft, a neurotransmitter encounters two types of receptors on the postsynaptic membrane: ionotropic receptors or G protein-coupled receptors. Binding of the neurotransmitter to ionotropic receptors triggers conformational changes that cause the built-in channels to open and allow the passage of ions. In contrast, G protein-coupled receptors generate intracellular responses in response to the binding of neurotransmitters.

Cessation of neurotransmission can be achieved in several ways. For example, the neurotransmitter can be taken up into the nerve terminal from which it was released or into neighbouring astrocytes; it can be metabolized by enzymes in the synaptic cleft such as acetylcholinesterase (in the case of acetylcholine), or it can simply diffuse away from the synaptic cleft.

1.3 Ionotropic receptors (ligand-gated ion channels)

Ionotropic receptors, or ligand-gated ion channels, open in response to the binding of a neurotransmitter to an orthosteric site(s), which triggers conformational changes that eventually result in the conduction of ions. There are two types of neurotransmitters - excitatory and inhibitory. Excitatory neurotransmitters are responsible for opening transmitter-gated cation channels which in turn causes an excitatory postsynaptic potential (EPSP). As a result, the postsynaptic neuron is more likely to fire an action potential. Examples of excitatory neurotransmitters are acetylcholine and glutamate. On the other hand, the action of inhibitory neurotransmitters such as γ-aminobutyric acid (GABA) and glycine lead to the opening of Cl^- channels, resulting in an inhibitory postsynaptic potential (IPSP) that reduces the rate of firing of action potentials (Alberts *et al.*, 2002; Purves *et al.*, 2008).

There are three major families of ionotropic receptors: (1) the 'Cys-loop' receptors, including the nicotinic acetylcholine receptors (nAChRs), the $GABA_A$ receptors and the 5-hydroxytryptamine ($5\text{-}HT_3$) receptors; (2) the ionotropic glutamate receptors, including the α-amino-3-hydroxy-5-methyl-4-isoxazolepropionic acid receptors (AMPARs), the N-methyl-D-aspartate receptors (NMDARs) and the kainate receptors (KARs); and (3) and the P2X receptors. Receptors within each family are composed of different numbers of subunits: the Cys-loop receptors are pentamers; the glutamate receptors are tetramers and the P2X receptors are trimers (Alexander *et al.*, 2011).

1.4 Glutamate receptors

Glutamate receptors (GluRs), mediate excitatory neurotransmission in the central nervous system (Watkins and Jane, 2006), and play a crucial role in memory formation and learning (Riedel *et al.*, 2003). They are also known to be involved in many acute or chronic neurodegenerative diseases, such as ischaemic brain damage, head trauma, epileptic seizures and Huntington's disease (Choi, 1988; Choi and Rothman, 1990; Meldrum and Garthwaite, 1990; Rothman and Olney, 1987). Consequently, glutamate receptors represent potential therapeutic targets, and understanding the mechanisms underpinning their function has become one of the most exciting areas of research in neuroscience and protein chemistry (Maragos *et al.*, 1988).

There are two broad categories of glutamate receptors, classified according to the mechanism by which their activation gives rise to a postsynaptic response: ionotropic glutamate receptors (iGluRs) and metabotropic glutamate receptors (mGluRs; Palmada and Centelles, 1998). Binding of glutamate activates iGluRs, leading to the opening of an ion channel. In contrast, activation of mGluRs controls the function of ion channels in the plasma membrane indirectly, via signalling cascades involving G proteins. Ionotropic receptors tend to be very fast in relaying information, whereas metabotropic receptors are associated with a slower and more prolonged stimulus (Madden, 2002; Muto *et al.*, 2007).

The iGluR family contains three major sub-families: AMPA, kainate and NMDA receptors (Fig. 1.2; Andersson *et al.*, 2001; Dingledine *et al.*, 1999; Madden, 2002). Collectively, AMPA and kainate receptors are known as non-NMDA receptors (Watkins and Jane, 2006).

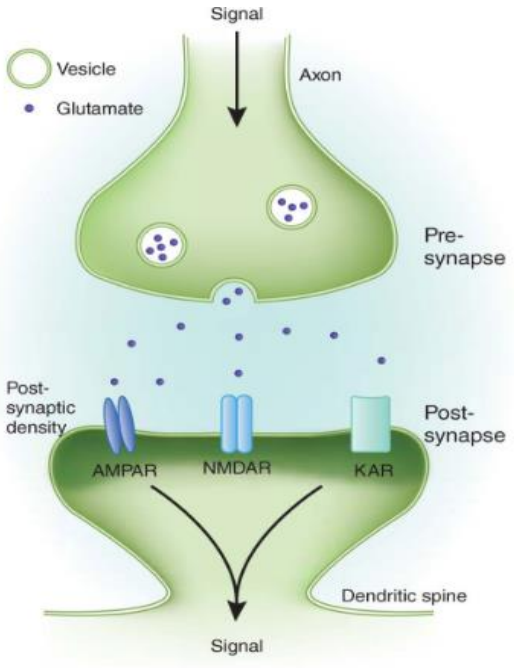

Figure 1.2. The glutamate synapse. Following release from presynaptic nerve terminals, glutamate can bind to AMPA, kainate and NMDA ionotropic receptor channels (Gecz, 2010).

1.4.1 AMPA receptors

Ionotropic glutamate receptors (iGluRs) with high affinity for the artificial glutamate analogue AMPA are homo- or hetero-oligomers composed of the subunits GluA1-GluA4 (or GluR1-GluR4) (Boulter *et al.,* 1990; Hollmann *et al.,* 1989; Keinänen *et al.,* 1990). The heterotetrameric AMPARs consist of GluA2 in combination with either GluA1, GluA3 or GluA4 (Greger *et al.,* 2007; Mayer, 2005). AMPARs are involved in fast excitatory synaptic signalling in the brain as well as in the generation of synaptic plasticity (Ross and Konnerth, 2000), which is responsible for learning and memory.

The subunit composition of an AMPAR determines its characteristics (Wright and Vissel, 2012). Of all the AMPAR subunits, GluA2 has the most impact on the biophysical properties of the resulting heteromeric complexes. AMPARs assembled from combinations of GluA1, GluA3, and GluA4 are highly permeable to Ca^{2+} as well as K^{+} and Na^{+} ions. However, when GluA2 is present within the AMPAR, the Ca^{2+} permeability is profoundly decreased (Hollmann *et al.,* 1991). Since the vast majority of AMPARs are hetero-oligomers consisting of GluA1/GluA2 or GluA2/GluA3

subunits, they are mostly Ca^{2+}-impermeable (Wenthold *et al.,* 1996). The Ca^{2+} permeability of AMPARs depends on RNA editing, whereby a post-transcriptional modification alters a codon encoding glutamine (Gln; Q) to a codon encoding arginine (Arg; R) (Sommer *et al.,* 1991). Though the unedited GluA2 (Q) subunit is permeable to Ca^{2+}, almost no unedited RNA exists in the brain; less than 1% of all RNA on average across the gray matter of the brain encodes unedited GluA2 (Q) (Kawahara *et al.,* 2003). Interestingly, some recent studies have shown that excitotoxic neuronal cell death in ischemia and amyotrophic lateral sclerosis (ALS) might be caused by the expression of unedited GluA2 (reviewed in Kwak and Kawahara, 2005; Kwak and Weiss, 2006; Liu and Zukin, 2007; Kwak *et al.,* 2010). Moreover, AMPARs lacking the GluA2 subunit are strongly inwardly rectifying in the presence of intracellular polyamines, which tend to block the AMPAR channel and thereby prevent the flux of K^+ ions through the channel pore. In contrast, AMPARs containing the GluA2 subunit have a linear or near-linear current-voltage (I/V) relationship (Cull-Candy *et al.,* 2006; Isaac *et al.,* 2007; Jonas, 2000).

To further complicate the picture, alternative splicing in the extracellular ligand binding domain of the AMPARs generates two variants, termed flip and flop. The region affected is an interchangeable sequence consisting of 38 amino acids located prior to the fourth transmembrane domain (Hollmann and Heinemann, 1994). The kinetic properties of the AMPARs are determined by the splice variant nature of the subunits. The flop variants of GluA2-GluA4 desensitize more rapidly than flip variants, but recover more slowly (Sommer *et al.,* 1990). On the other hand, GluA1 flip and flop variants exhibit the same rate of desensitization (Mosbacher *et al.,* 1994).

AMPARs are potential therapeutic targets for various neurological disorders. As mentioned above, in ALS, AMPAs allow cytotoxic levels of Ca^{2+} into neurons which results in motor neuron death. In the same way, over-activation of AMPARs causes neuronal damage in epileptic seizure and ischemia. On the other hand, decreased AMPAR activation sometimes causes Alzheimer's disease (Chang *et al.,* 2012).

1.4.2 Kainate receptors

KARs are homo- or hetero-oligomers of the subunits GluK1-GluK5 (GluR5-GluR7, KA1 and KA2) (Betler *et al.,* 1990, 1992; Egebjerg *et al.,* 1991; Werner *et al.,* 1991; Herb *et al.,* 1992) that respond selectively to the agonist kainate. Of these, GluK1-3 can

form functional homomeric or heteromeric receptors, whereas GluK4 and GluK5 only participate in heteromeric receptors, partnering any of the GluK1-3 subunits (Dingledine *et al.*, 1999).

KARs act principally as modulators of synaptic transmission and neuronal excitability, and they are distributed throughout the brain. Our understanding of the functions of KARs has been hindered by the lack of specific agonists and antagonists, since most of the compounds active at KARs also interact with AMPARs (Lerma *et al.*, 2001). However, the GluK1 subunit has proved to be relatively amenable to the development of selective pharmacological agents; these have been produced from structurally diverse templates, including synthetic decahydroisoquinolines as well as the natural products willardiine and dysiherbaine (Jane *et al.*, 2009). On the other hand, the discovery of the 2,3-benzodiazepines, such as GYKI 53655 and GYKI 52466, which antagonize AMPARs but not KARs (Paternain *et al.*, 1995; Wilding *et al.*, 1996), has made it possible to separate the responses mediated by each receptor. Hopefully, this will eventually permit the determination of the role played by kainate receptors in synaptic transmission and plasticity in the mammalian brain. KARs are potentially important targets for the development of therapeutics, especially KAR antagonists, which have been examined for amelioration of a diverse range of neurological conditions, including chronic pain, epilepsy and migraine (Contractor *et al.*, 2011). KARs cause both postsynaptic as well as presynaptic depolarization, and they carry part of the current during the synaptic response (Castillo *et al.*, 1997; Cossart *et al.*, 1998; Frerking *et al.*, 1998; Vignes and Collingridge, 1997), regulating both excitatory and inhibitory transmitter release (Clarke *et al.*, 1997; Kamiya and Ozawa, 2000; Rodríguez-Moreno *et al.*, 1997). Thus, overall, KARs are involved in the regulation of activity of synaptic networks.

The potential therapeutic utility of targeting KARs has mostly focused on the control of epileptogenic activity (Mulle *et al.*, 1998; Vissel *et al.*, 2001). Despite the confusion surrounding the targeting of KARs for the control of seizures in humans suffering from epilepsy, there is evidence that GluK1-selective antagonists can block seizures induced by pilocarpine in rodent models (Smolders *et al.*, 2002). KAR antagonists also reduce excitotoxicity in oligodendrocytes, which are very sensitive to complement-mediated attack following KAR activation (Alberdi *et al.*, 2006). This exciting observation might be particularly relevant to demyelinating diseases such as multiple sclerosis; however,

it needs to be established at least in mouse models that KAR antagonists retard disease progression before further progress can be made. In addition, potential linkages between neuropsychiatric disorders and KARs are emerging with the development of genetic epidemiology; for instance, a recent genetic study found that loss-of-function mutations in GluK2 co-segregated with non-syndromic autosomal recessive mental retardation in a consanguineous family (Motazacker *et al.*, 2007). This approach proves the crucial role of GluK2-containing receptors in normal brain function in humans. Finally, KARs show genetic association with neurodevelopmental disorders (Dutta *et al.*, 2007; Jamain *et al.*, 2002; Kim *et al.*, 2007; Motazacker *et al.*, 2007; Shuang *et al.*, 2004) and also play a role in the development of neuronal circuitry (Lauri *et al.*, 2005; Lauri *et al.*, 2006; Marchal and Mulle, 2004).

Though most research has focused on GluK1 because of the availability of selective antagonists, some functions of KARs are known to be associated with the other four subunits. For example, GluK4 is associated with schizophrenia in some populations (Pickard *et al.*, 2006); GluK2 and GluK3 are linked to obsessive-compulsive disorder (Delorme *et al.*, 2004; Sampaio *et al.*, 2011); GluK3 is linked with depression (Schiffer and Heinemann, 2007) and GluK2 is linked with autism (Dutta *et al.*, 2007; Jamain *et al.*, 2002; Kim *et al.*, 2007; Shuang *et al.*, 2004). These association studies in many cases have been limited to suggestive linkages to these disorders, and further scrutiny will be required to establish firmly a causative link to human disease.

1.4.3 NMDA receptors

As its name suggests, the NMDAR is selectively activated by NMDA. According to sequence homology, there are three subfamilies of NMDARs, consisting of seven different subunits (Traynelis *et al.*, 2010; Paoletti, 2011; Cull-Candy and Leszkiewicz, 2004). NMDARs are di- or tri- heterotetrameric assemblies typically containing GluN1 subunits in association with either GluN2 (GluN2A-GluN2D) subunits or a mixture of GluN2 and GluN3 (GluN3A-GluN3B) subunits (Paoletti, 2011). Most NMDA receptors require co-agonism by glycine (Johnson and Ascher, 1987) or D-serine (Mothet *et al.*, 2000), which bind to the GluN1 or GluN3 subunits, whereas glutamate binds to the GluN2 subunits. However, NMDA receptors composed of GluN1 and GluN3 subunits can be activated either by glycine or D-serine alone and are mostly unresponsive in presence of glutamate (Chatterton *et al.*, 2002; Awobuluyi *et al.*, 2007;

Balasuriya *et al.,* 2014). Another unique property of NMDARs is that, at resting membrane potentials, the channel pore is blocked in a voltage-dependent manner by extracellular Mg^{2+} (Nowak *et al.,* 1984; Mayer *et al.,* 1984). AMPAR activation causes depolarization of the postsynaptic neuron, which removes Mg^{2+}, thus allowing NMDAR activation. Unlike AMPA and kainate receptors, NMDA receptor activation leads to a Ca^{2+} influx into the postsynaptic cell, a signal that is involved in the activation of a number of signalling cascades (Mayer et *al.,* 1984; Nowak *et al.,* 1984). NMDARs are critical for the development of the central nervous system (CNS), generation of rhythms for breathing and locomotion, and processes underlying learning, memory and neuroplasticity (Blanke and VanDongen, 2009).

NMDAR dysfunction is believed to underlie numerous neurological disorders and pathological conditions. Hypofunction of NMDAR may cause cognitive defects, whereas overstimulation causes excitotoxicity and subsequent neurodegeneration. For these reasons, NMDARs are represent therapeutic targets for CNS disorders including stroke, hypoxia, ischemia, head trauma, Huntington's, Parkinson's, and Alzheimer's diseases, epilepsy, neuropathic pain, alcoholism, schizophrenia, and mood disorders (Kemp and Mckernan, 2002; Jansen and Dannhardt, 2003; Chazot 2004; Farlow 2004; Wood 2005; Cai 2006; Missale *et al.,* 2006; Brown and Krupp 2006).

1.5 Structure of ionotropic glutamate receptors

Quaternary glutamate receptor structures were initially provided by the low resolution (~40-20 Å) technique of electron microscopy (Safferling *et al.,* 2001; Tichelaar *et al.,* 2004; Nakagawa *et al.,* 2005, 2006; Midgett and Madden, 2008). The first high-resolution (3.6 Å) structure of an intact iGluR, the antagonist bound rat GluA2 homotetramer, was obtained using X-ray crystallography (Figs. 1.3-1.5; Sobolevsky *et al.,* 2009).

According to the crystal structure, iGluRs have a shape like the capital letter 'Y' and consist of four discrete semi-autonomous domains (>900 residues): the extracellular amino-terminal domain (ATD), the extracellular ligand-binding domain (LBD), the transmembrane domain (TMD), and the intracellular carboxyl-terminal domain (CTD). The TMDs comprise three domains (M1, M3, and M4) plus a cytoplasm-facing re-entrant membrane loop (M2), and form the ion channel. In the extracellular region, the ATDs sit at the 'top' of the receptor, while the LBDs are packed in between the ion

channel and the ATDs. Both ATDs and LBDs are ordered as dimers-of-dimers; however the TMDs exhibit 4-fold symmetry. Overall, the full-length receptor shows a 2-fold symmetry. All the known glutamate receptor subunits (AMPA, kainate, and NMDA) share a similar architecture (Sobolevsky *et al.*, 2009). Here, I will discuss the structure of AMPA receptor in detail.

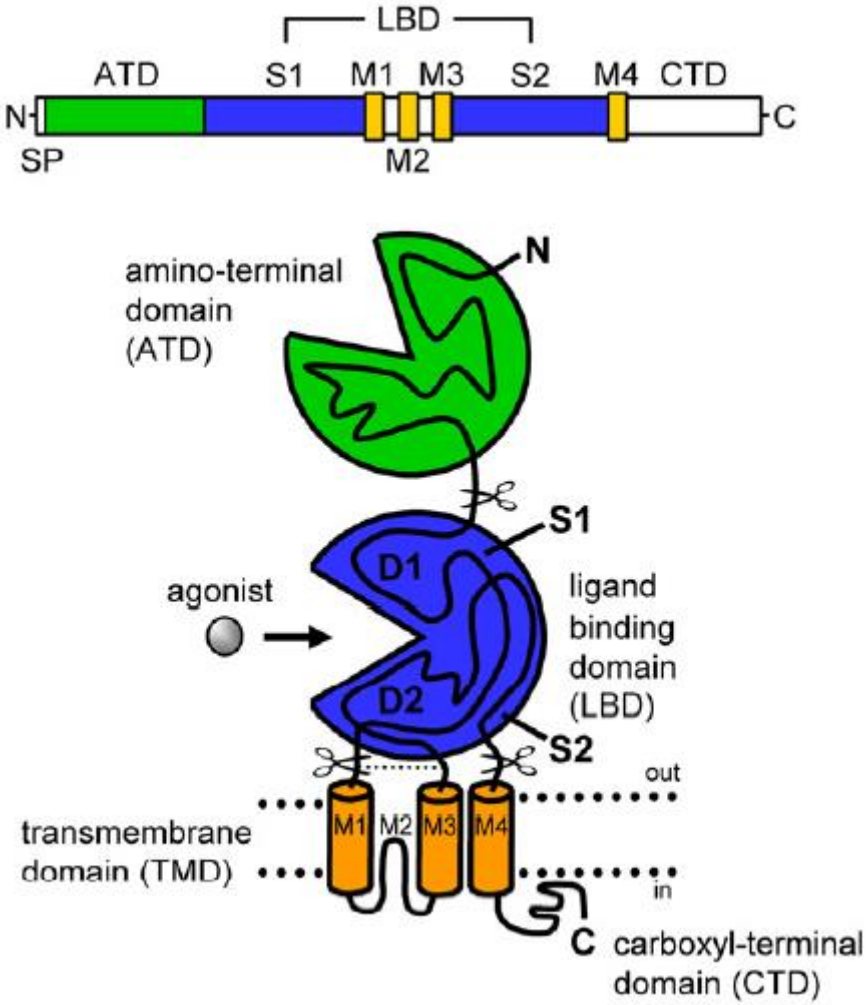

Figure 1.3. Linear representation of a subunit polypeptide chain, and schematic illustration of the subunit topology. Glutamate receptor subunits have a modular structure composed of two large extracellular domains [the ATD (green) and the LBD (blue)]; a TMD (orange) that forms part of the ion channel pore; and an intracellular CTD. The LBD is defined by two sequences of amino acids termed S1 and S2. The TMD contains three membrane-spanning helices (M1, M3, and M4) and a membrane re-entrant loop (M2) (Traynelis *et al.*, 2010).

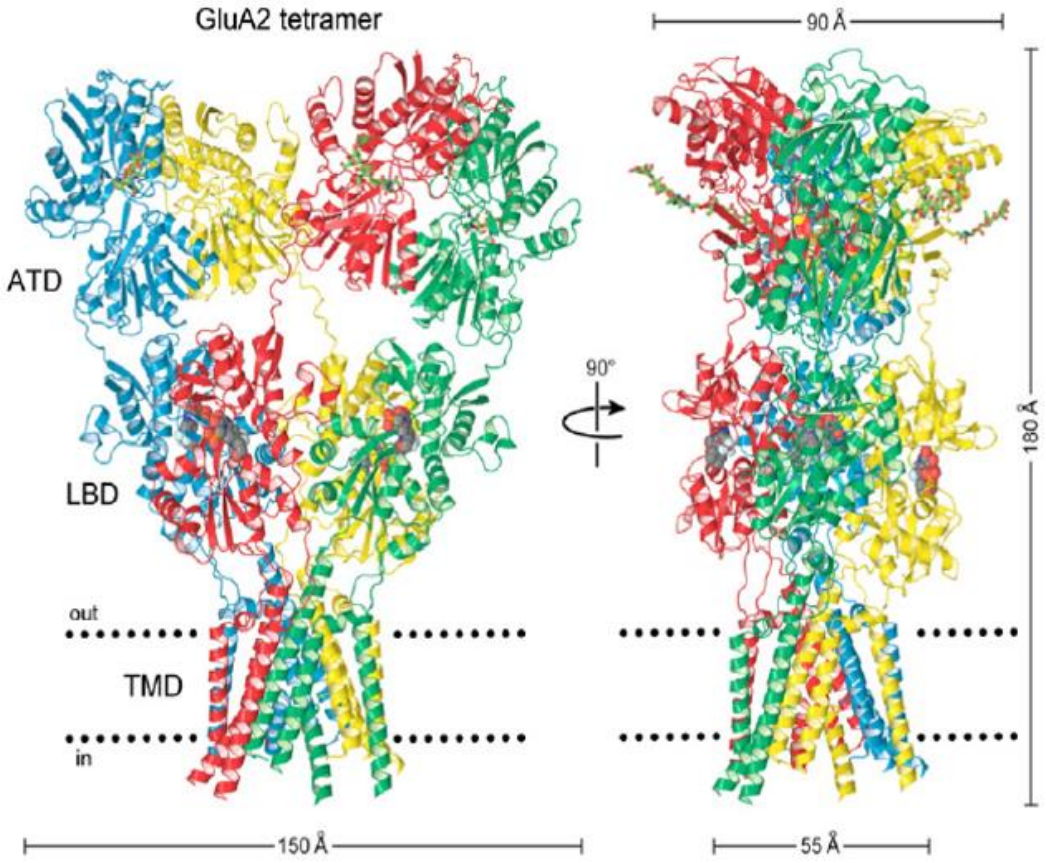

Figure 1.4. Crystal structure at 3.6 Å resolution of the membrane-spanning tetrameric GluA2 AMPAR (Sobolevsky *et al.*, 2009).

1.6 Domains of ionotropic glutamate receptors

1.6.1 Amino-terminal domain

All the iGluRs contain a short signal peptide (14-33 residues) at the beginning of ATD which is eventually removed by proteolysis after membrane insertion. In addition, the ATDs also contain sites for *N*-linked glycosylation (Hollmann *et al.,* 1994; Standley and Baudry, 2000). The ATD is a clamshell-like structure, composed of two parts (R1 and R2) connected by loops (Karakas *et al*., 2009). The N terminus is positioned at the top of R1, whereas the linker to the LBD is found at the bottom of R2. There are extensive interactions between the R1-R1 and R2-R2 domains of the non-NMDA receptors (Clayton *et al.,* 2009; Jin *et al.,* 2009; Kumar *et al.,* 2009).

The four iGluR subunits (A to D) form two cross-wise dimers, namely A/C and B/D, of which B/D and A/C subunits are proximal and distal, respectively, relative to the overall 2-fold axis of symmetry. There are two different interfaces between the ATDs of the four subunits: one between the A/B and C/D subunits, and another between the B and D subunits of the A/B and C/D dimers (Sobolevsky *et al.,* 2009).

1.6.2 Ligand binding domain

Domain swapping, or subunit crossover, causes a different subunit arrangement at the LBD layer compared to the ATD layer. Specifically, the LBDs are arranged as A/D and B/C dimers, with contacts between the A and C subunits of the dimers. In this case the A/C subunits and the B/D subunits are proximal and distal to the overall 2-fold axis, respectively (Sobolevsky *et al.,* 2009).

Each LBD adopts a clamshell-like conformation, where the polypeptide sequence S1 forms most of one half of the clamshell (D1), which is located at the extracellular portion of the M1 helix. The sequence S2 between the M3 and M4 membrane helices forms most of the opposite half of the clamshell (D2). The two lobes (D1 and D2) form the cleft of the ligand binding pocket (Stern-Bach *et al.,* 1994).

1.6.3 Transmembrane domain

Four GluA2 subunits arrange their transmembrane domains around an axis of ~4-fold rotational symmetry; each of these subunits has 3 transmembrane helices (M1, M3 and M4), a central pore-like helix (M2) and a polypeptide pore-lining loop.

The S1-TM1 segment is extended until it reaches the membrane where it turns through 90° and forms a short helix (pre-M1) parallel to the membrane. The pre-M1 helices from the four subunits resemble a cuff around the external surface of the ion channel pore that could be an important determinant for channel gating. TM1 resides on the exterior of the channel domain, whereas the TM2 helix lies at the pore, and the TM3 helices line the outer cavity, crossing each other near the extracellular surface to generate a closed conformation. The TM4 helix at the exterior, interacts with TM1 from the adjacent subunit through contacts via the S2 segment (Sobolevsky *et al.,* 2009).

1.6.4 C-terminal domain

In the various glutamate receptor subunits, the CTD is the most diverse in terms of amino acid sequence. Though the structural details of the CTD are yet to be confirmed, this domain is known to be responsible for the regulation of membrane trafficking and receptor function, since it possesses different phosphorylation sites and binding sites. The CTD is also believed to be involved in delivery of the receptor to the plasma membrane, stabilization in the membrane, post-translational modifications, and targeting for degradation (Traynelis *et al.,* 2010).

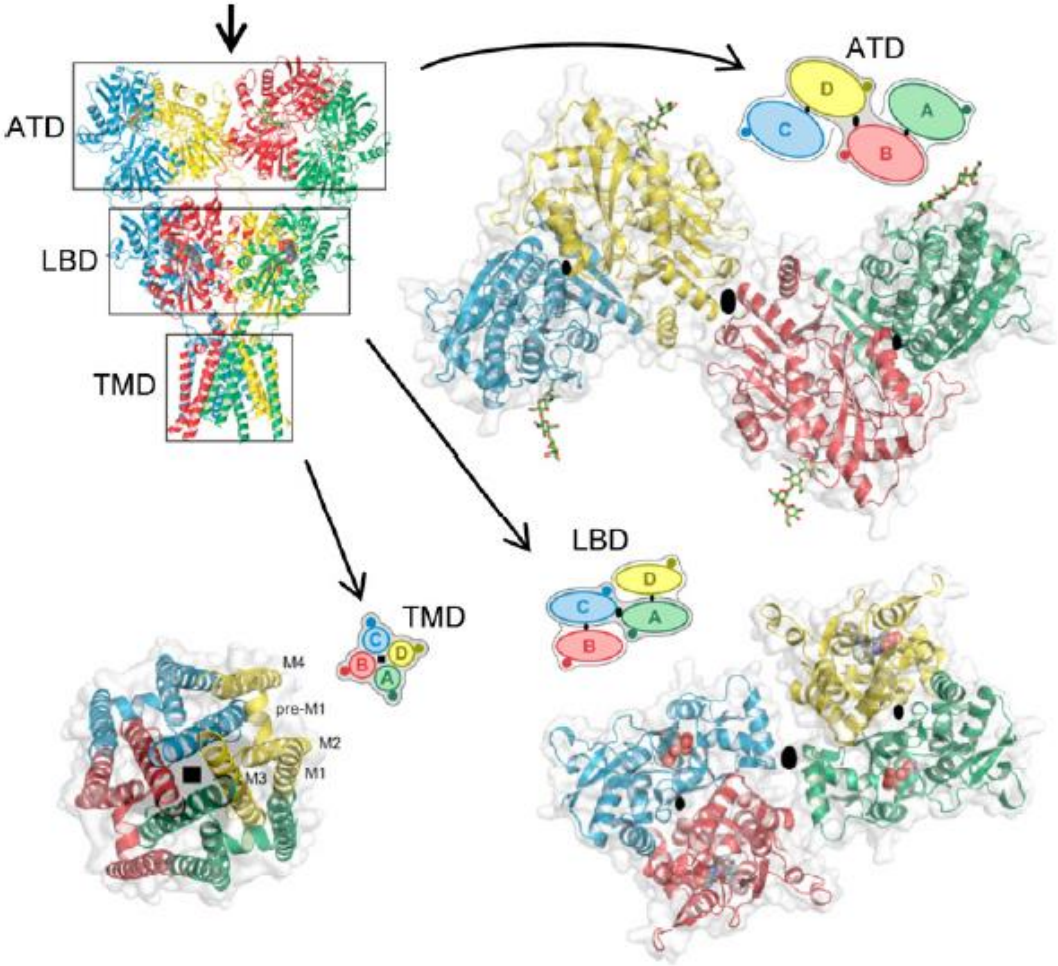

Figure 1.5. Subunit interfaces between the ATD, LBD, and TMD domains of the four subunits in the tetrameric GluA2 AMPA receptor. The subunits are viewed from top down the 2-fold axis of symmetry. The ATDs and LBDs have a 2-fold axis of symmetry, whereas the TMDs have a 4-fold axis of symmetry (Sobolevsky *et al.*, 2009).

1.7 Domain swapping

The swapping of domains in 'local' dimers between subunits in the AMPA receptor is a noteworthy feature. Within the ATD layer, subunits A and B interact with each other to form a local ATD 'dimer' (red, Fig. 1.6). In the same way subunits C and D form the other dimer (purple). Within the LBD layer, however, subunit A forms a LBD dimer with the corresponding domain of subunit D (blue, Fig. 1.6), while subunit B associates with subunit C (orange). In addition, in the transmembrane helices in the TMD, subunits A and B form extensive contacts with each other as well as with subunits C and D and form a tetramer (green, Fig. 1.6). Apparently, the ATD-S1 amino acid linkers between the ATD and LBD initiate this swapping of subunits. It seems from the crystal structure that the ATD-S1 linkers of the A/C subunits adopt a compact conformation, whereas the ATD-S1 linkers of the B/D subunits have an extended conformation (Sobolevsky *et al.*, 2009).

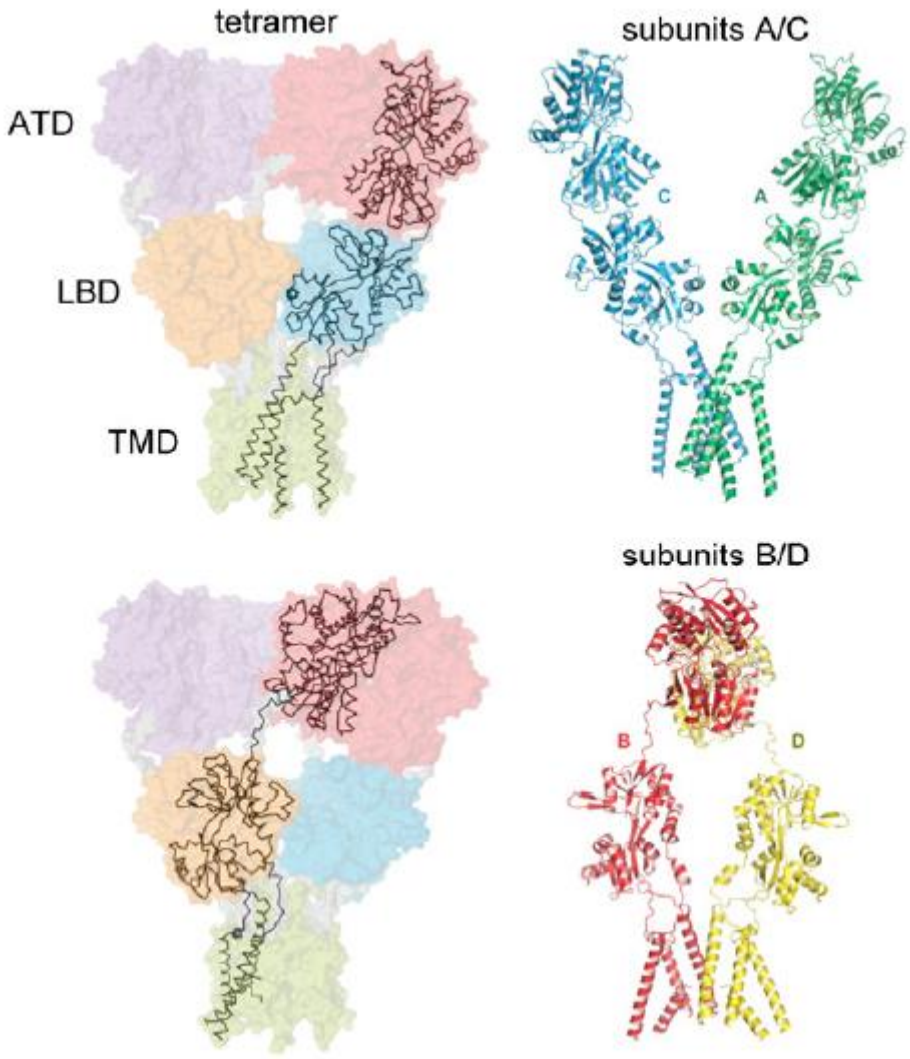

Figure 1.6. Symmetry mismatch between the TMDs and the extracellular domains (ATDs and LBDs) and the subunit crossover (or domain swapping) from the LBD to the ATD give rise to two distinct types of subunits in the homotetrameric GluA2 receptor with two distinct conformations. The subunits are referred to as the A/C and B/D subunits (Sobolevsky *et al.*, 2009).

1.8 Mechanism of gating of ionotropic glutamate receptors

Ionotropic receptors pass ions in response to the binding of ligands (agonists) to the extracellular domain of the channel. Once the receptor has been activated, the agonist either dissociates from the receptor and the receptor returns to its resting state (deactivation), or the agonist-bound receptor undergoes one or more additional conformational changes that decouple the action of agonist binding from receptor activation; that is, the receptor becomes desensitized to the activating action of the agonist (Armstrong *et al.*, 2006).

In all iGluRs, as mentioned above, there are two discontinuous polypeptide segments, called D1 and D2 (Stern-Bach *et al.*, 1994) linked together to form a clamshell-like structure (Armstrong *et al.*, 1998; Kuusinen *et al.*, 1995; Fig. 1.3) According to the Armstrong and Gouaux model (2000), activation of the AMPAR (GluA2) involves binding of glutamate to the LBD clamshell, followed by closure of the clamshell by approximately 21°, resulting in the opening of the conductive pore. Conversely, during deactivation, reopening of the clamshell closes the conductive pathway, and eventually glutamate is released from the LBD. In the desensitized state, the ligand remains bound but the ion channel is closed (Armstrong *et al.*, 2006; Fig. 1.7).

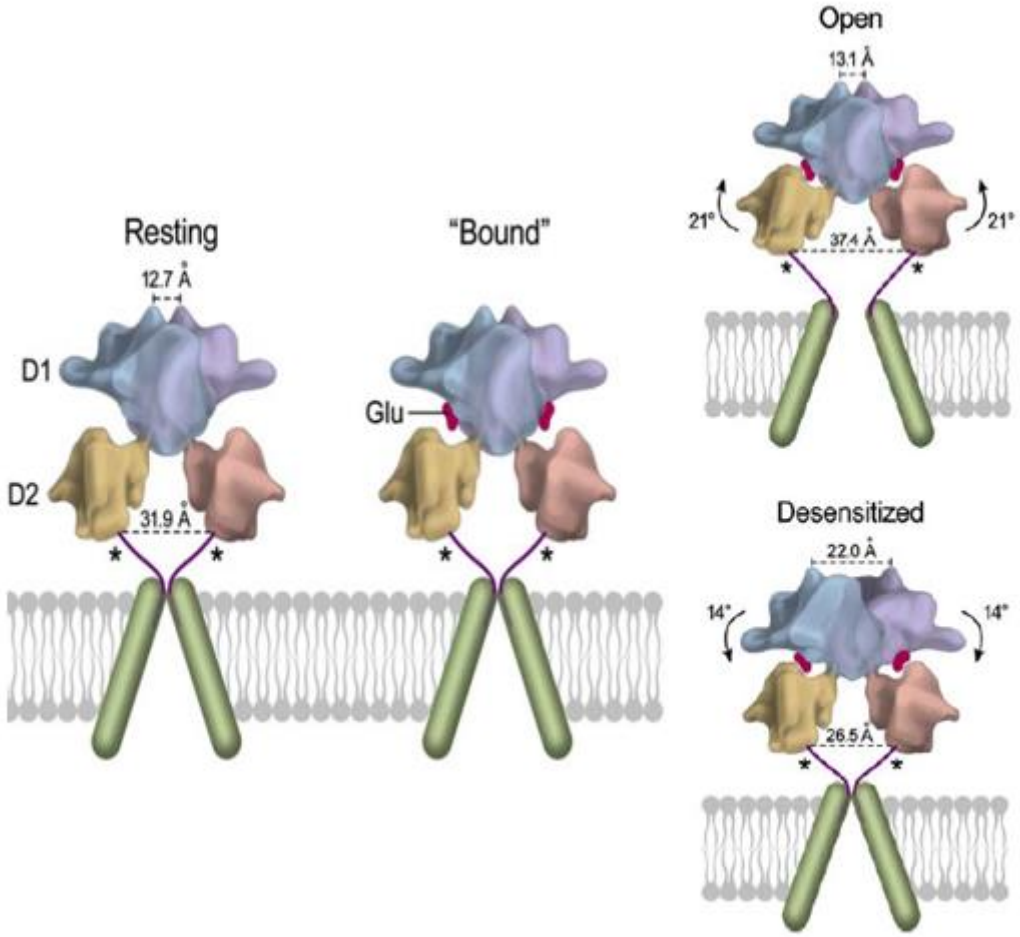

Figure 1.7. Mechanism of gating of iGluRs. Binding of glutamate to the LBD of an iGluR leads to two possible outcomes: either the D1-D1 interface remains fixed and the domain closure is translated into ion channel opening, or the D1-D1 interface ruptures and the ion channel closes, leading to the desensitized state (Armstrong *et al.*, 2006).

1.9 The membrane environment

The cell membrane, consisting of a phospholipid bilayer with integrated and associated proteins, separates the interior of all cells from the outside environment (Singleton, 1999). The phospholipid bilayer is composed of two layers of lipid molecules organized in two sheets, and is typically about 5-6 nm thick (Engelman, 1971; Mitra *et al.*, 2004). The bilayer is structurally and chemically heterogeneous, and consists of three distinct regions:

(i) The hydrophobic core, which is populated by the lipid acyl chains. The core is ~3-4 nm thick and largely impermeable to polar molecules and ions. Notably, bilayer thickness varies with chain length, chemistry and temperature (Lewis and Engelman, 1983; Rawicz *et al.*, 2000; Trauble and Haynes, 1971).

(ii) The hydrophilic headgroups, which constitute the hydrated fraction of the phospholipid bilayer. This layer is approximately 0.8-0.9 nm thick, and the phosphate groups are located ~0.5 nm outside the hydrophobic core (Nagle and Tristram-Nagle, 2000).

(iii) A partially hydrated intermediate region, which is approximately 0.3 nm thick (Marsh, 2001, 2002).

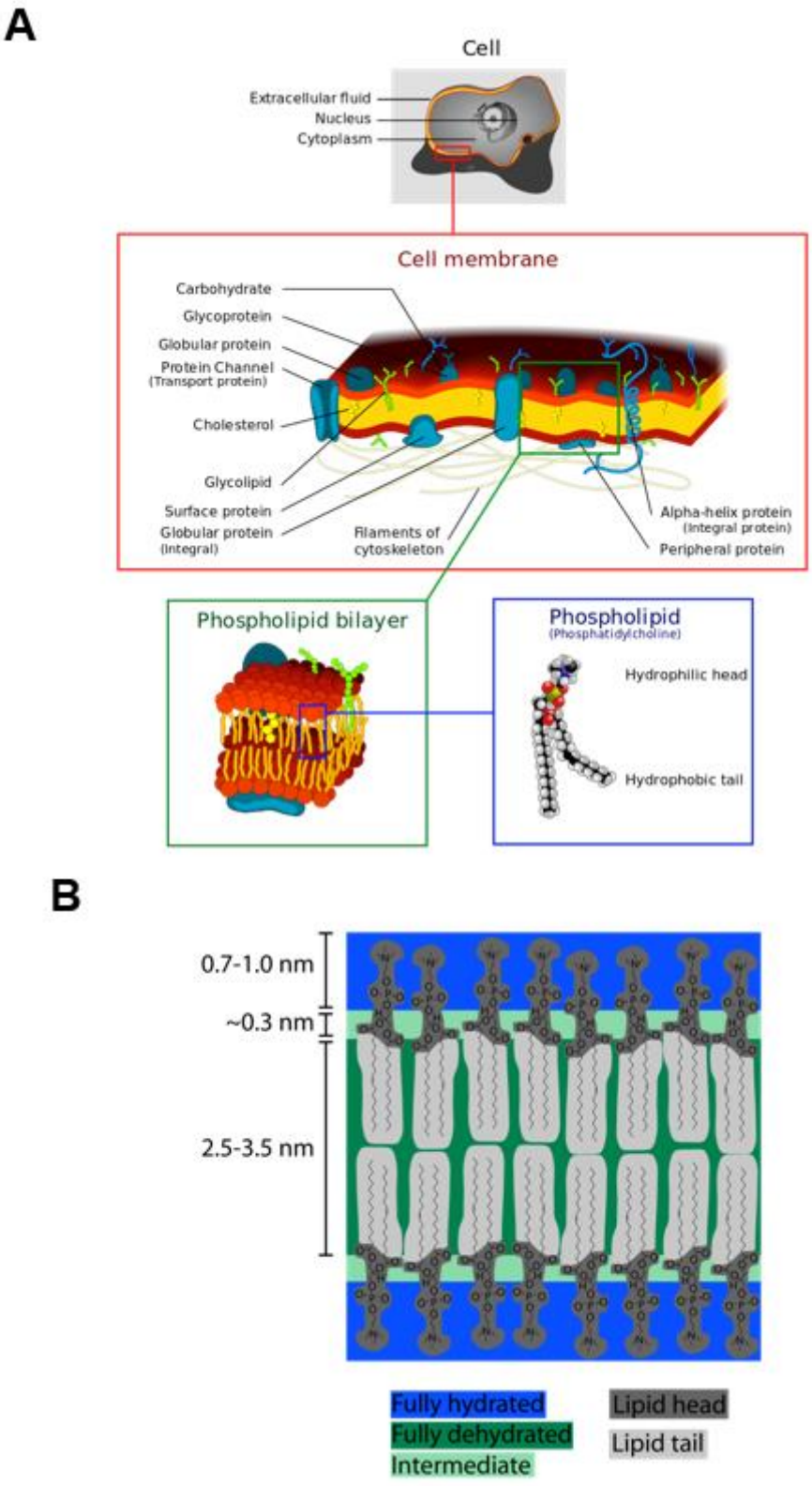

Figure 1.8. Structure of a eukaryotic cell membrane. (A) Illustration of a cell membrane. (B) Schematic cross-sectional profile of a typical lipid bilayer. There are three distinct regions: the fully hydrated head groups, the fully dehydrated alkane core and a short intermediate region with partial hydration.

1.10 Reconstitution of proteins in lipid bilayers

Since membrane proteins have crucial roles in all organisms, there is great interest in studying the various biochemical and biophysical properties of these proteins. Study of membrane proteins *in vivo* is challenging because there is a tendency of membrane proteins to associate with other proteins (Kucik *et al.*, 1999). Further, it is unlikely that a single protein species will represent a major peptidic constituent of the membrane; a notable exception is bacteriorhodopsin, which is the only protein present in the membrane of *Halobacteria salinaria* (Drew *et al.*, 2003). In addition, lipid bilayers are quite fragile, and this property limits the investigation of membrane proteins *in vivo* by standard biophysical methods such as nuclear magnetic resonance (NMR), X-ray crystallography or electron microscopy (EM; Seddon *et al.*, 2004).

Investigation of the behaviour of membrane proteins in lipid membranes can be achieved through formation of various model membranes, such as monolayers, bilayers, liposomes and nanodiscs. From an analytical point of view, the reconstitution of a purified membrane protein into a lipid bilayer allows a detailed exploration of the individual features and activities of that protein (Shen *et al.*, 2013). It should be borne in mind, however, that studying reconstituted proteins can be challenging, mostly because of the differences between the environments provided by the native cell membrane and a model phospholipid bilayer. Another complication is the likelihood that the composition of the model lipid bilayer, and specifically factors such as hydrophobicity of the lipid chains and the hydrophilicity of the lipid headgroups, will affect the interactions between the bilayer and the proteins (Aroca *et al.*, 2001), potentially leading to modifications of the functional activities of the proteins (Kucik *et al.*, 1999; Liao *et al.*, 2006). Furthermore, it is often not feasible to isolate membrane proteins in sufficient amounts from their native environment, necessitating overexpression of cloned constructs in *E. coli* or mammalian cells. This type of overexpression often results in aggregation of the protein (Frenkel *et al.*, 1980). Finally, it is difficult to provide a suitable environment for reconstituting purified proteins, since they are mostly insoluble in aqueous solution (Seddon *et al.*, 2004).

Liposomes (phospholipid vesicles), consisting of a self-closed phospholipid bilayer, have been used for more than 30 years in the investigation of the function of membrane proteins (Rigaud and Levy, 2003). Membrane proteins are usually inserted into liposomes by solubilizing the proteins with detergents during purification and then

mixing with phospholipid vesicles to form phospholipid-protein-detergent complexes (Fig. 1.9). Several methods are employed for removing the detergent from the complex, among which dialysis is the most common. When the detergent concentration reaches a critical level, the protein spontaneously associates with the phospholipid membrane, resulting in the desired proteoliposomes (Helenius and Simon, 1975; Paternostre *et al.*, 1988; Rigaud *et al.*, 1995). The procedure for formation of proteoliposomes usually needs to be optimized on a case-by-case basis, since the destabilization of the preformed liposomes by the addition of detergent and the subsequent removal of the detergent are crucial steps in reconstitution. Hence, it still remains a major challenge to find reconstitution conditions suitable to obtain a homogeneous proteoliposome preparation with a functionally integrated protein, with the desired protein-to-lipid ratio, and with the desired size and liposome integrity (Goñi and Alonso, 2000; Lichtenberg *et al.*, 2013).

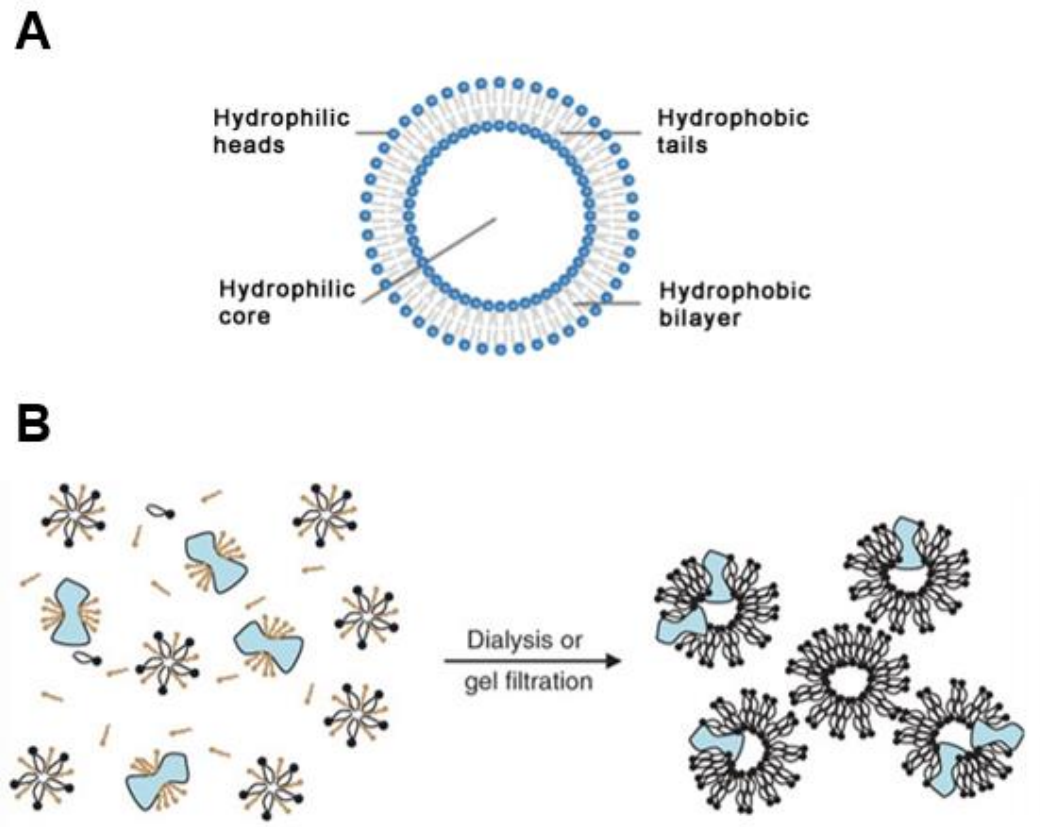

Figure 1.9. Liposomes. (A) Liposome structure. (B) Ion channel reconstitution. Blue, ion channel protein; brown, detergents; black, lipids (Nimigean, 2006).

1.11 Techniques for revealing structure and conformational changes of receptors

1.11.1 Electron microscopy (EM)

The electron microscope uses a high-voltage beam of electrons to create an image of the specimen. It is capable of much higher magnification and has a greater resolving power than a conventional light microscope, allowing it to see much smaller objects in finer detail. Unlike light microscopy, which is limited by diffraction to about 200 nm resolution and useful magnifications below 2000x, transmission electron microscopy can achieve better than 50 pm resolution and magnifications of up to about 10,000,000x (Erni *et al.*, 2009). It should be noted, however, that various super-resolution techniques are increasing the resolving power of light microscopes. Fig. 1.10 shows the structure of native AMPAR purified from rat brain, and viewed using single-particle EM.

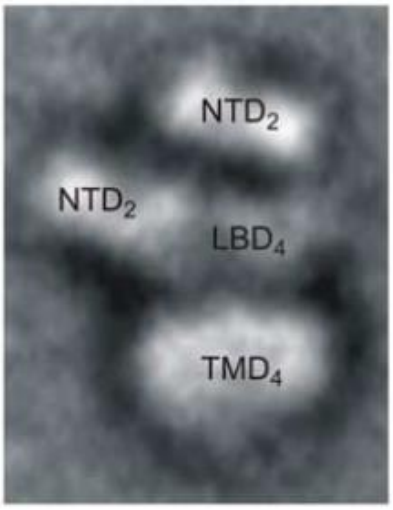

Figure 1.10. EM structure of an AMPAR, revealing the modular structure. NTD2, NTD dimers; LBD4, four LBDs; TMD4, tetrameric TMD (Nakagawa et al., 2005).

The major limitation of transmission EM is related to sample preparation, since in room-temperature conventional EM techniques, samples are prepared by chemical fixation and dehydration, resulting in conditions that are far from the native environment of the membrane protein. Further, electron microscopes are expensive to buy and maintain, and experiments have to be carried out in ultra-high vacuum, which along with the electron beam can damage biological samples (Fujiyoshi, 2011).

1.11.2 Electron crystallography

Membrane proteins can be imaged in their lipid environment by electron crystallography. This method was pioneered in the 1970s by Henderson and Unwin, who imaged bacteriorhodopsin in the form of two-dimensional (2D) sheets (Henderson and Unwin, 1975) The atomic structure of the same protein was eventually published in 1990 (Henderson *et al.,* 1990). A common problem with electron crystallography is radiation damage of organic molecules and proteins during imaging, limiting the resolution that can be obtained (Carpenter *et al*., 2008).

1.11.3 X-ray crystallography

X-rays have a wavelength of around 0.1 nm, which is much shorter than the wavelength of light (300-700 nm) or electrons (2 nm). For this reason, X-ray crystallography enables visualization of protein structures at the atomic level. In X-ray crystallography, a beam of X-rays are passed through a crystal of the protein, which diffracts the beam into many specific directions. The angles and intensities of these diffracted beams allow the construction of a 3-dimensional map showing the distribution of atoms in the structure.

The soluble proteins myoglobin was the first protein to be crystallized in the late 1950s (Kendrew *et al.,* 1958). Since that success, over 100,000 X-ray crystal structures of proteins have been reported of which most of them are soluble proteins (www.rcsb.org). The photosynthetic reaction centre *Phodopseudomonas viridis* was the first membrane protein solved by X-ray crystallography in 1985 (Deisenhofer *et al.,* 1985).

Transmembrane proteins such as ion channels are significantly harder to crystallise due to the presence of large hydrophobic domains (Ostermeier and Michel, 1997; Wallin and von Heijne, 1998). The detergents used to solubilize them often interfere with crystallization and when not embedded in the lipid bilayer membrane proteins usually lose their three-dimensional structures. To overcome this hurdle, membrane proteins are often subjected to several modifications and mutations. For instance, the crystallized rat GluA2 AMPA receptor is missing thirty-six residues from its CTD, six residues from the ATD-LBD domain linker, and multiple glycosylation sites. Moreover, another five residues were also replaced by alanine and one by glutamine (Sobolevsky *et al.,* 2009). These mutations result in a structure that may not completely reflect the native

protein structure. In addition, crystallized proteins are ‘dead’, and present in only one state, whereas native proteins are dynamic and flexible.

1.11.4 Cryo-EM

Cryo-electron microscopy (cryo-EM) is a form of transmission electron microscopy (TEM) where the sample is studied at cryogenic temperatures. For cryo-EM, the sample is frozen rapidly in liquid ethane and maintained at liquid nitrogen or even liquid helium temperatures, so that the water forms vitreous (non-crystalline) ice (Dubochet *et al.,* 1988). The advantage of cryo-EM over ‘conventional’ EM is that it allows the observation of specimens without staining or fixation, mimicking the conditions of their native environment. This is a particular benefit over the X-ray crystallography, which involves placing them in non-physiological environments, which might cause functionally irrelevant conformational changes. Cryo-EM has an atomic resolution of beyond 3 Å, which is comparable to that achievable using X-ray crystallography (Fischer *et al.,* 2015; Grant and Grigorieff, 2015; Bartesaghi *et al.,* 2015). Also, for single-particle cryo-EM, unlike EM, the total electron dose used to image each molecule is set very low to preserve structural information at the subnanometre-resolution level (Cheng, 2015). For instance, by trapping GluA2 AMPA receptor in their major functional states by cryo-EM, Meyerson *et al.* (2014) showed that desensitization is accompanied by disruption of the ATD tetramer.

However, maintaining such a narrow and low temperature range for the membrane protein is challenging, and in addition the low-dose imaging creates a very poor signal-to-noise ratio. Hence, a large number of 2D tilted images from many similar molecules must be averaged to enhance the signal-to-noise ratio as well as to provide the different views needed to generate a 3D reconstruction at atomic resolution (De Rosier and Klug, 1968). Further, an atomic model is built by fitting the known sequences into the density map from the reconstruction. Hence, the cryo-EM structures of proteins can sometimes be predetermined by relatively weak evidence. Therefore, the quality of the raw images needs to be checked even when a convincing final model is produced.

1.11.5 Nuclear magnetic resonance (NMR)

NMR spectroscopy is a technique in which the protein sample is exposed to a static external magnetic field and thus the intramolecular magnetic field around an atom in

the molecule changes the resonance frequency and provides details of the electronic structure of a molecule and its individual functional groups. Unlike X-ray crystallography, which provides only the static protein structures, NMR spectroscopy yields dynamic information as well as information about binding interactions (Fernandez and Wuthrich, 2003).

To date, over 10,000 structures of proteins have been determined by NMR (Berman *et al.*, 2000), but most are soluble proteins up to molecular masses of ~30 kDa and, in only a few cases, beyond. Typical membrane proteins in a model membrane system (protein/detergent/lipid) are usually too large for structure determination in solution. This is because in solution NMR, linewidths increase as the molecules get larger due to stronger spin-spin relaxation, which results in peaks overlapping or broadening so that ultimately they are undetectable (Arora and Tamm, 2001). Further, since membrane proteins have long stretches of hydrophobic residues, they require the presence of detergents or lipids to retain their native fold. This is a limitation for more conventional solution-state NMR spectroscopy because the incorporation of the protein into detergent micelles or detergent/lipid bicelles increases the rotational correlation time of this complex (Opella and Marassi, 2004). This leads to a cascade of difficulties that make membrane protein structure determination incomparably more challenging than structure determination of soluble proteins. Though solid state NMR can overcome some of these limitations, there are difficulties in producing highly ordered samples in solid-state NMR which are required to improve line-widths and resolution (Arora and Tamm, 2001).

1.11.6 Atomic force microscopy (AFM)

The atomic force microscope was invented in the late 1980s by Binnig, Quate and Gerber (Binnig *et al.*, 1986), combining the principles of the scanning tunnelling microscope and the stylus profilometer (Baro *et al.*, 1985; Teague *et al.*, 1982). Instead of using an incident beam, AFM measures the minute forces acting between a sharp probe and the sample (Dorobantu *et al.*, 2012; Dufrêne, 2008; Engel and Muller, 2000). Since its invention, the atomic force microscope has become an invaluable tool for the imaging of biological samples under near-physiological conditions (Fig. 1.11).

AFM works by scanning a fine pyramidal tip back and forth over a surface in a raster pattern. The tip is typically tenths of a nanometre in diameter, and is attached to the end

of a micro-engineered cantilever, which can be moved in three dimensions using a piezoelectric scanner. As a consequence of deflections caused by the attractive or repulsive forces between the tip and the surface, the cantilever bends. The extent of bending is measured by a laser beam that is reflected off the back of the cantilever and detected by a photodiode array. In this way, a topographic image of the surface can be generated (de Pablo and Carrion-Vazquez, 2014; Edwardson and Henderson, 2004).

According to the nature of the tip motion, AFM scanning can operate in three modes: contact, non-contact and tapping mode. In tapping mode imaging, the cantilever oscillates at or near the cantilever's resonant frequency just above the sample surface. Sample movement in the X, Y and Z directions are organized by piezoelectric motors. Piezo elements inside the cantilever holder also control the oscillation of the cantilever with a high amplitude as long as there is no drift or interaction of the tip with the surface. Throughout the scanning process, the vertically oscillating tip alternately contacts the surface and lifts off. When the oscillating cantilever comes close to the surface, its oscillation changes because of interaction forces such as van der Waals, dipole-dipole and electrostatic forces. Cantilever deflection is sensed by a laser beam directed onto the top edge of the cantilever which is then reflected onto a pair of semi-conductor photoelectric diodes. When the tip encounters a bump in the surface, the oscillation around the amplitude set point is reduced. In contrast, when the tip passes over a depression, there is more space for the cantilever to oscillate and the amplitude increases. In both cases the sample is moved relative to the tip by the piezo motor in order to keep the oscillation constant. This feedback loop adjusts the tip-to-sample distance and maintains a constant oscillation of the tip. The voltage required to maintain this oscillation is proportional to the height of the sample. Another two piezo-electric bodies move the sample in the X and Y directions. In this way, the three dimensional topography of the sample mapped. Tapping mode is preferred for imaging samples that are easily damaged or loosely bound to their substrate (such as biomolecules), since it applies minimal physical forces to the sample in comparison to other modes. The use of tapping mode also avoids many problems associated with friction, adhesion or electrostatic forces.

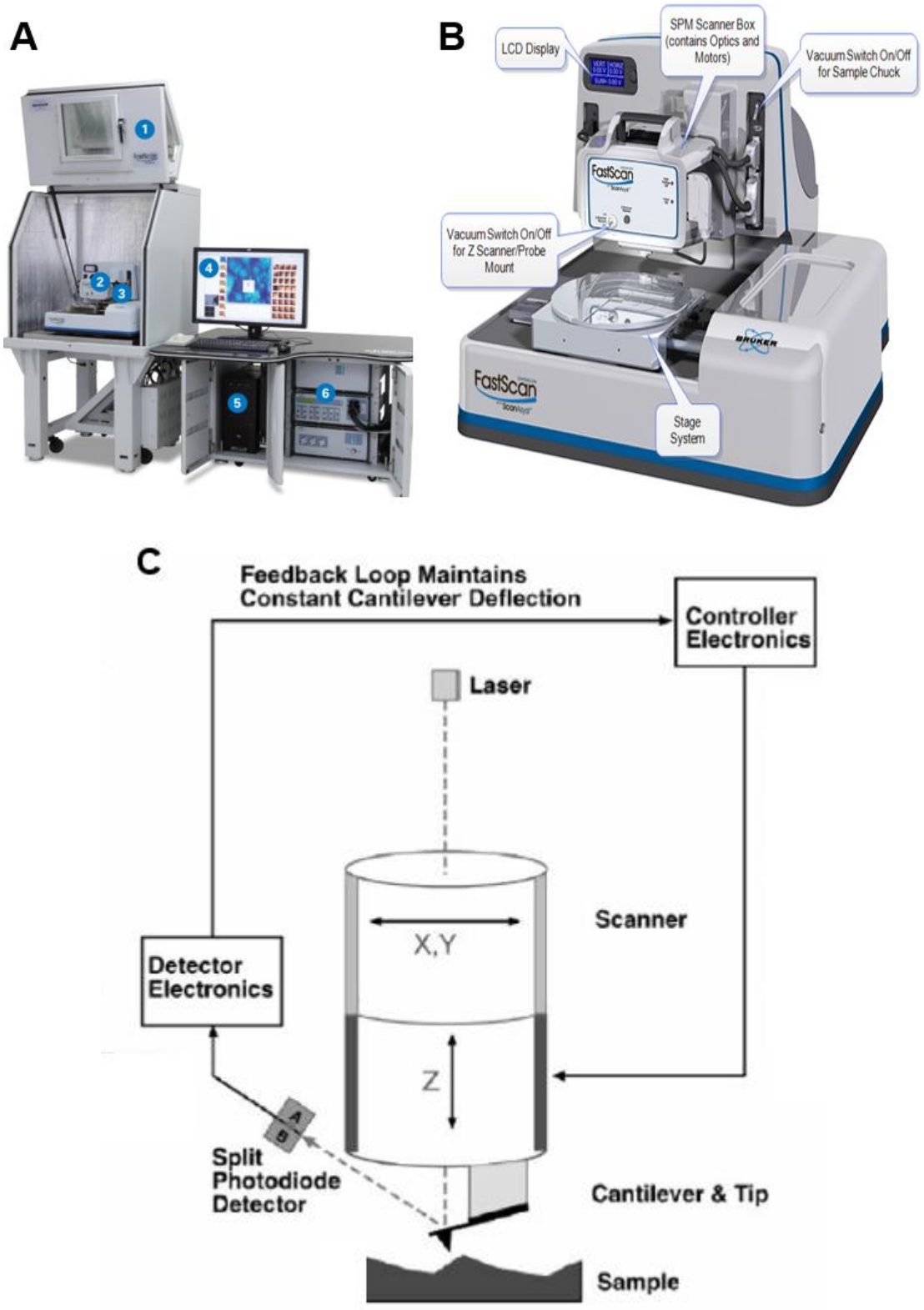

Figure 1.11. (A) Dimension FastScan system configuration: (1) Acoustic and vibration isolation enclosure; (2) Scanners; (3) Ultra-stable high-resonance microscope base; (4) Monitor and FastScan NanoScope software; (5) Computer; (6) NanoScope V, Stage Controller and HV amplifier. (B) Scanner and microscope base. (C) Schematic representation of the atomic force microscope.

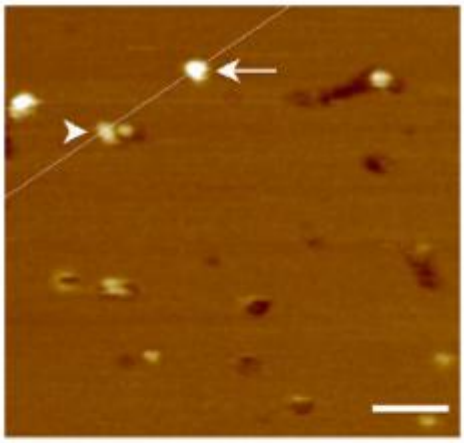

Bilayer containing GluN1/GluN3A receptors (Balasuriya *et al*., 2014)

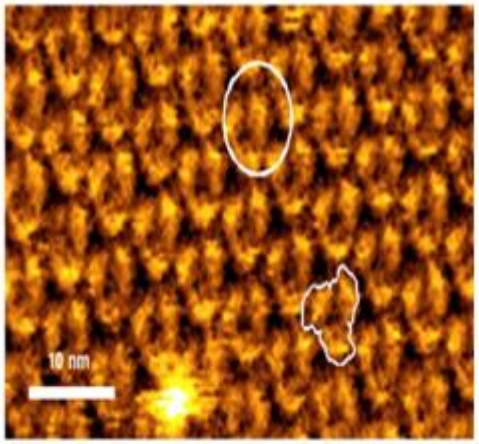

Single bacteriorhodopsin molecules in purple membrane (Oesterhel *et al*., 2000)

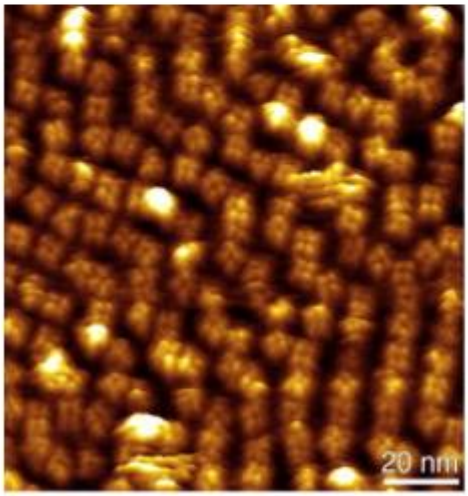

MlotiK1 potassium channel (Mari *et al*., 2011)

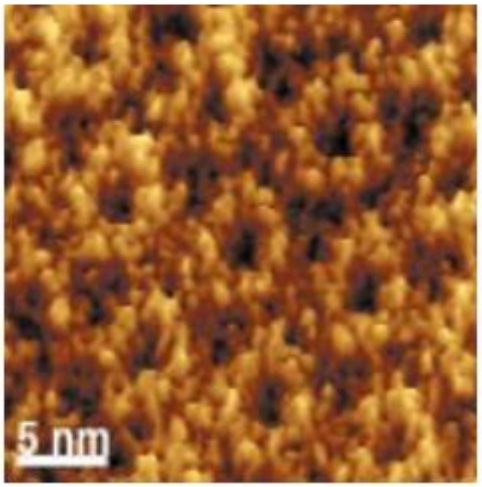

Trimeric porin OmpF (Müller and Engel, 1999)

Figure 1.12. Typical AFM images of various membrane proteins.

1.12 Advantages of AFM

There are several advantages of using AFM rather than other imaging techniques for imaging membrane proteins; for instance, it allows visualization of membrane proteins without any kind of labelling (e.g. fluorescent tags or staining agents) in the context of a lipid bilayer, and in a physiological buffer (Engel and Gaub, 2008; Fotiadis, 2012; Müller, 2008). AFM also has the greatest resolution among the various tools used to image living cells. It is capable of sub-nanometre resolution and can be used not only for the imaging of microorganisms or cultured mammalian cells, but also for the evaluation of many other phenomena, including molecular binding (Lesoil *et al.*, 2010), elastic properties of a membrane, and rigidity at the submicron level (Nakano *et al.*, 2008), as well as the physical properties of biological samples, such as Young's modulus and adhesion forces (Franz and Puech, 2008).

According to Ando *et al.* (2013) an ideal microscopy technique for observing a biological specimen must meet five conditions: (i) imaging under fluid, (ii) high spatial resolution, (iii) high temporal resolution, (iv) low invasiveness to the specimen and (v) direct imaging of the specimen without the use of markers. AFM meets the first, second and the fifth conditions and partly meets the fourth condition; however, the temporal resolution of a conventional AFM system (several seconds to minutes per frame) seriously limits its ability to observe structural changes occurring during cellular and single-molecule events in real time. Fast-scan AFM was a breakthrough since it provides a data acquisition rate of up to 10 frames per second for a scan area of 240 x 240 nm with 100 x 100 pixels. Another strength of AFM is its two measures of resolution; the plane of the measurement and in the direction perpendicular to the surface. Typically, the lateral resolution is about 1-5 nm and vertical resolution is ~30 pm. Therefore, it is possible to use fast-scan AFM to reach valid conclusions in a straightforward manner without intricate analyses and interpretations.

1.13 AFM resolution

It is very hard to describe the AFM resolution in straightforward as AFM is a computer-controlled local probe instrument. Lateral resolution of AFM is largely depends on the geometry of the tip (Gan *et al.*, 2009). In this case, a sharp tip is crucial to obtain a high resolution image. Some other factors also affect the lateral resolution:

- Moisture layer on the surface (in air)
- Ionic screening charges (in fluid)
- Tip engage robustness (AFM's ability to preserve the tip during engage)

The lateral resolution of the Bruker Dimension FastScan instrument used in my lab depends on the radius of the tip. In the case of the Fast Scan D tip, it is ~8 nm.

On the other hand, Vertical AFM resolution is limited by position noise (with mechanical, electrical and fundamental (thermal) contributions). These noise sources eventually translate into a certain amount of variation in the height signal and unfortunately height features that are smaller than this are simply lost in the noise and cannot be recovered. That's why measurements of nanoscale features with an AFM give an apparent height that is almost always lower than their known true height (Santos *et al.,* 2011). It is important to minimize the vibrations of the instrument to get the maximum vertical resolution. In case of the Bruker Fast Scan instrument the vertical resolution is <30 pm.

1.14 Limitations of AFM

One of the disadvantages of AFM compared with TEM or SEM (scanning electron microscopy) is the single-scan image size. With the Bruker Fast scan instrument, the maximum X-Y scan range is 35 µm x 35 µm, whereas in the case of TEM and SEM it is tens of µm and several millimetres, respectively.

The major limitation of AFM lies with the scanning tip and in particular the convolution error that it produces. Because of this error, protruding features appear wider than they really are, and holes appear smaller (both narrower and often less deep). This is because the size of the tip is similar to the size of the sample being imaged. For this reason, the radius of curvature of the tip needs to be very small in order to produce high-quality images.

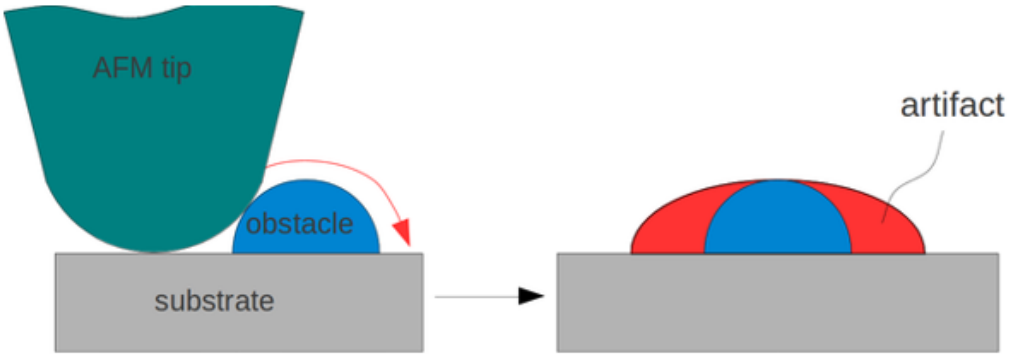

Figure 1.13. Convolution error in AFM.

1.15 Difficulties encountered in structural analyses of membrane proteins

Since membrane proteins are amphiphilic in nature; there are several problems associated with studying their structures. Currently, only ~1,200 structures are listed in the protein data bank (PDB) from ~600 different membrane proteins, whereas the number of the total deposited protein structure exceeds 120,000 (White, 2017).

Major limitations include the following:

(a) Overexpression. This is one of the major bottlenecks in the overall workflow for membrane protein production. Heterologous overexpression often causes toxicity to the cell, resulting in low expression levels. Further, inactive protein can often be produced because of the limited capacity of the cell to accommodate over-expression and the lack of correct folding or posttranslational modifications (Carpenter *et al.*, 2008).

(b) Preservation of biological activity. During the solubilization stage, membrane proteins are extracted from their native membrane environment, the lipid membrane, by the addition of detergents, which cover the hydrophobic surface areas of the proteins and the lipid ‘tails’, while hydrophilic parts of the proteins remain in contact with the aqueous environment. Detergents thereby break down lipid-protein and protein-protein interactions, thereby allowing the separation of proteins. Harsh solubilization and purification procedures may lead to inactivation of the protein, since the detergent cannot necessarily mimic the physical/chemical environment of the lipid bilayer. In particular, the heterogeneity, lateral pressure, and charge distribution of a biological membrane is impossible to replicate (Belandia and Stokes, 2010).

(c) The size of the protein. It is impossible, using solution NMR methods, to obtain high-resolution spectra of membrane proteins which are large, aggregated, or incorporated into supramolecular assemblies (Opella and Marassi, 2004).

(d) Difficulty in obtaining well-diffracting three-dimensional (3D) crystals. The amphiphilic nature of membrane proteins makes it difficult to obtain diffracting crystals for X-ray crystallography.

(e) Low abundance**.** The quantity of membrane proteins is often very low in their natural setting. This makes their natural source impractical as a starting material for their preparation.

1.16 Use of AFM in characterizing membranes and membrane proteins

Since the introduction of AFM, it has been applied in different areas of biology, including analyses of the structure and function of membrane and membrane-associated proteins (Gerber and Lang, 2006; Parot *et al.*, 2007; Muller and Engel, 2007; Whited and Park, 2014). As an example, Grandbois *et al.* (1998) investigated the rate of hydrolysis of a supported dipalmitoyl phosphatidylcholine bilayer by the lipolytic enzyme PLA_2. They also induced mechanical perturbation via the AFM tip, which inspired AFM-based nanolithography. In other studies by Kirat *et al.* (2008) and Nielsen *et al.* (1999), AFM imaging was used to investigate remodelling of lipid bilayers by enzyme hydrolysis.

AFM is also being used by several groups to reveal the dynamic behaviour of single protein molecules. Examples include the visualization of conformational changes in the hexagonally packed intermediate (HPI) layer that covers *Deinoccocus radiodurans*. High-resolution AFM identified two interchangeable conformations (plugged and unplugged) that coexist in the central pore of the hexameric units (Fig. 1.14; Müller *et al.*, 1996).

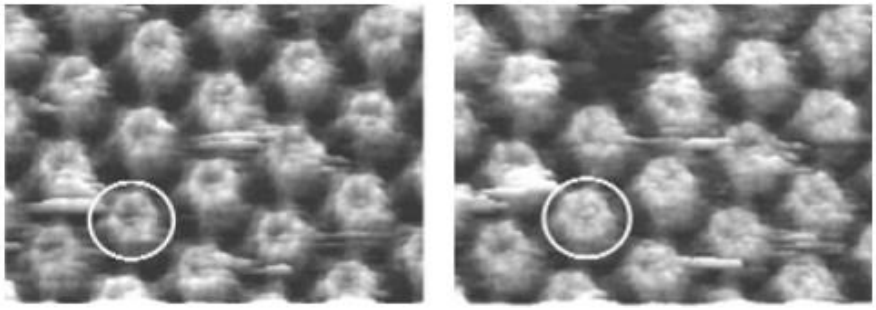

Figure 1.14. Conformational changes in the inner surface of the HPI layer, showing plugged or unplugged conformations of hexameric pores (circled) in sequential recordings (Muller *et al.*, 1996).

In another study, Shibata *et al.* (2010) applied high-speed AFM to monitor real-time structural changes in bacteriorhodopsin in response to light (Fig. 1.15).

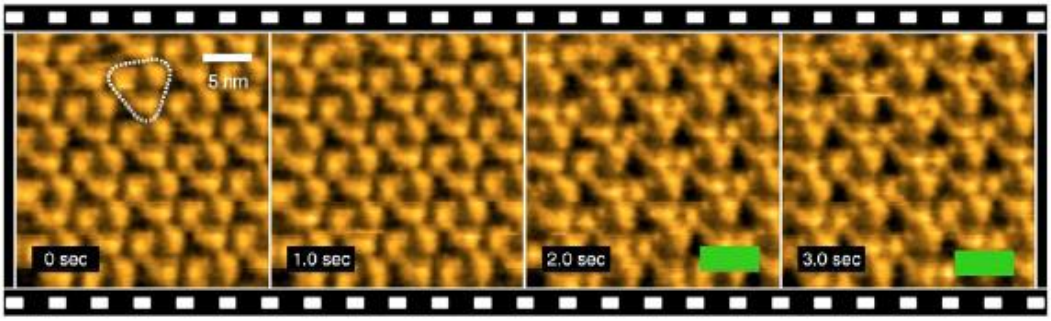

Figure 1.15. Dynamic high-speed AFM images of D96N mutant bacteriorhodopsin in purple membrane. Images were taken at a rate of 1 frame per second. The first two frames represent the inactive basal state (0-1 s), whereas last two frames were imaged after light activation (2-3 s). A bacteriorhodopsin trimer is outlined in the first frame. The green bars indicate illumination of 532-nm green light at 0.5 µW (Shibata *et al.*, 2010).

AFM imaging has also been used to show that the trimeric porin OmpF, an outer membrane protein of *E. coli*, forms a domain protruding 1.3 nm above the bilayer in the resting state, whereas the same domain becomes 0.6 nm shorter upon induction of a >200 mV electric potential, the generation of a K^+ gradient >0.3 M, or the application of an acidic environment (pH ≥3) (Müller and Engel, 1999). In addition, fast-scan AFM imaging was used to observe the ATP/ADP-induced conformational cycle of bacterial

chaperonin GroES/GroEL. Imaging showed not only the binding and separation of GroES and GroEL but also identified two distinct open-conformations of GroEL in the presence of different nucleotides (Fig. 1.16; Yokokawa *et al.*, 2006).

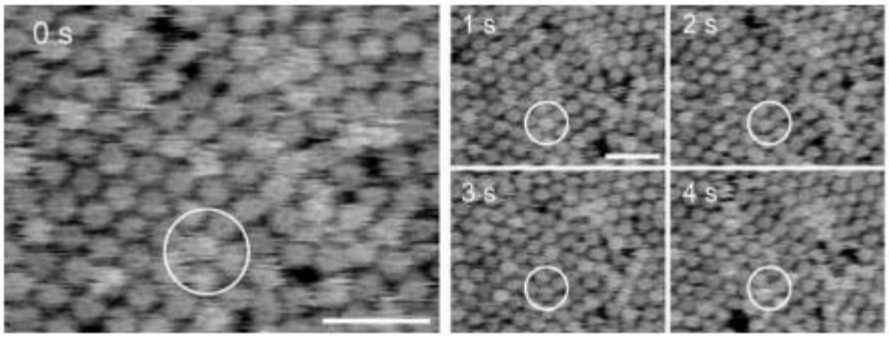

Figure 1.16. Single-molecule AFM imaging of chaperonin GroEL dynamics in the presence of ADP. A sequence of AFM images at a rate of 1 frame per second of GroEL in a buffer solution was taken in the presence of 50 μM ADP without GroES. Scale bars and the Z-scale are 50 nm and 7.5 nm respectively. GroEL molecules had at least two different conformations: one is the open conformation (at 0 sec, elevated by 1 nm) and the other is the closed (compact) conformation (Yokokawa *et al.*, 2006).

Moreover, because of its high resolution, AFM imaging can distinguish individual proteins within oligomers. An example in this context is the ~5 Å lateral resolution and ~1 Å vertical resolution images of individual peptide loops of bacteriorhodopsin molecules. AFM topographs revealed that the surface structures and elasticity of bacteriorhodopsin were largely be governed by its oligomeric state (Müller *et al.*, 1999).

1.17 The aims of my research

As mentioned above, several intact iGluR crystal structures have now been reported (Dürr et al., 2014; Sobolevsky *et al.*, 2009; Sun *et al*., 2002, Hansen *et al*., 2007; Mayer 2005; Armstrong and Gouaux, 2000; Armstrong *et al*., 2006). Notably, extensive mutation was required to stabilize these structures for crystallization, including the addition of cross-linking cysteine residues, suggesting that the native receptors are very flexible. The GluA2 AMPAR and the GluK2 KAR have also been studied using single-particle cryo-EM (Meyerson *et al.*, 2014; Nakagawa *et al.*, 2005; Chaudhry *et al.*, 2009). Together, these studies provide fascinating ‘snap-shots’ of the receptors as they

transition between different functional states. What is lacking, so far, is information about the kinetics underlying these structural transitions, because the techniques used lack time resolution. There is also the concern that the stabilizing mutations might lock the receptors into unnatural conformations.

I set out to use AFM to study activation-induced structural changes in native, full-length kainate and AMPA receptors. It has been shown previously by others in my lab that the co-agonists glutamate and glycine trigger a ~1-nm reduction in the height of the extracellular domain of the GluN1/GluN2A NMDAR integrated into supported lipid bilayers (Suzuki *et al.*, 2013). Here, I describe experiments using fast-scan AFM imaging, combined with UV photolysis of caged glutamate and line-scanning of individual receptors, to detect time-dependent reductions in the height of kainate and AMPA receptors, and to determine the significance of this height change with respect to the functional states of the receptors. I also describe the use of sequential imaging to study the effect of activation on the mobility of the extracellular domains of these receptors. My results demonstrate the ability of fast-scan AFM imaging to provide fascinating new information about the global dynamics of these key ionotropic receptors.

2. Materials and methods

2.1 Receptor constructs

The following receptor constructs were used:
KAR (Chapter 3). Rat GluK2 (Q) with a haemagglutinin (HA) tag at the N-terminus in the vector pRK5 (kind gift of Dr. Yael Stern-Bach, Department of Biochemistry, Hebrew University of Jerusalem, Israel). Point mutants (D776K and L783C) in the same construct were also used (kind gift of Dr. Derek Bowie, Department of Pharmacology and Therapeutics, McGill University, Canada).

AMPAR (Chapters 4 and 5). Rat GluA2 (Q) (flip and flop isoforms) with an HA tag at the N-terminus in the vector pRK5. GluA2 flip with point mutations S775N or L504A, ΔATD-GluA2 flip (minus ATD), ΔATD-GluA2-GFP flip and flop in the same construct were also used (kind gifts of Dr. Derek Bowie, McGill University).

2.2. Cell culture

tsA 201 cells (a subclone of HEK 293 cells stably expressing the SV40 large T-antigen) were grown in Dulbecco's modified Eagle's medium (Sigma) supplemented with 10% (v/v) fetal bovine serum, 100 μg/ml streptomycin and 100 units/ml penicillin (Sigma) in an atmosphere of 5% CO_2/air at 37°C.

2.3 Transfection

In all cases, 250 μg of DNA was used to transfect 5 x 162 cm^2 flasks using either calcium phosphate precipitation or polyethylenimine (Stewart *et al.*, 2011). After transfection, cells were incubated for 24-48 h at 37°C to allow expression of receptors.

2.4 Immunofluorescence

Glass coverslips were coated by incubation in poly-D-lysine (50 μg/ml) and collagen (50 μg/ml) solutions, and transfected cells were grown on the coverslips. Cells were fixed with 4% paraformaldehyde in phosphate-buffered saline (PBS) for 1 h at 4°C, washed three times in PBS, and permeabilized with 0.2% (v/v) gelatin, 0.1% (w/v) saponin in PBS for 1 h. After three washes, the coverslips were incubated for 1 h with mouse monoclonal anti-HA primary antibody in permeabilization buffer. After three more washes, fluorescein isothionate (FITC)-conjugated goat anti-mouse secondary

antibody was applied. After three final washes, coverslips were mounted on glass slides using Vectashield™ mounting liquid and sealed. Imaging was carried out using a Zeiss Axioskop 2 microscope.

2.5 Immunoaffinity chromatography

Proteins were isolated from transfected cells by immunoaffinity chromatography. HEPES-buffered saline (HBS; 100 mM NaCl, 50 mM HEPES, pH 7.6) containing 2 mM EDTA was used to remove transfected cells from 5 x 162 cm^2 flasks. All subsequent steps were carried out at 4°C. The cells were pelleted by centrifugation at 2,500 rpm for 5 min in a bench centrifuge. The cells were then resuspended in solubilization buffer [25 mM Tris-HCl, pH 7.5, 150 mM NaCl, 10 mM EDTA, 1 ml 10% Triton X-100, 1 mM PMSF, and protease inhibitor cocktail (Roche), prepared in Biotechnology Performance Certified (BPC) water (Sigma)]. The cell suspension was incubated on a rotating wheel for 1 h, and precipitated DNA was removed by low-speed centrifugation. The sample was then centrifuged in a T70i rotor at 35,000 rpm for 1 h. Solubilized extracts were incubated with anti-HA-agarose beads (Sigma) for 3 h. The immunobeads bearing captured protein were pelleted by centrifugation at 2,500 rpm for 5 min and the supernatant was aspirated. The beads were then washed extensively with 3-[(3-cholamidopropyl) dimethylammonio] propanesulfonate (CHAPS; Sigma), and the bound protein was eluted for 1 h with HA peptide (200 μg/ml).

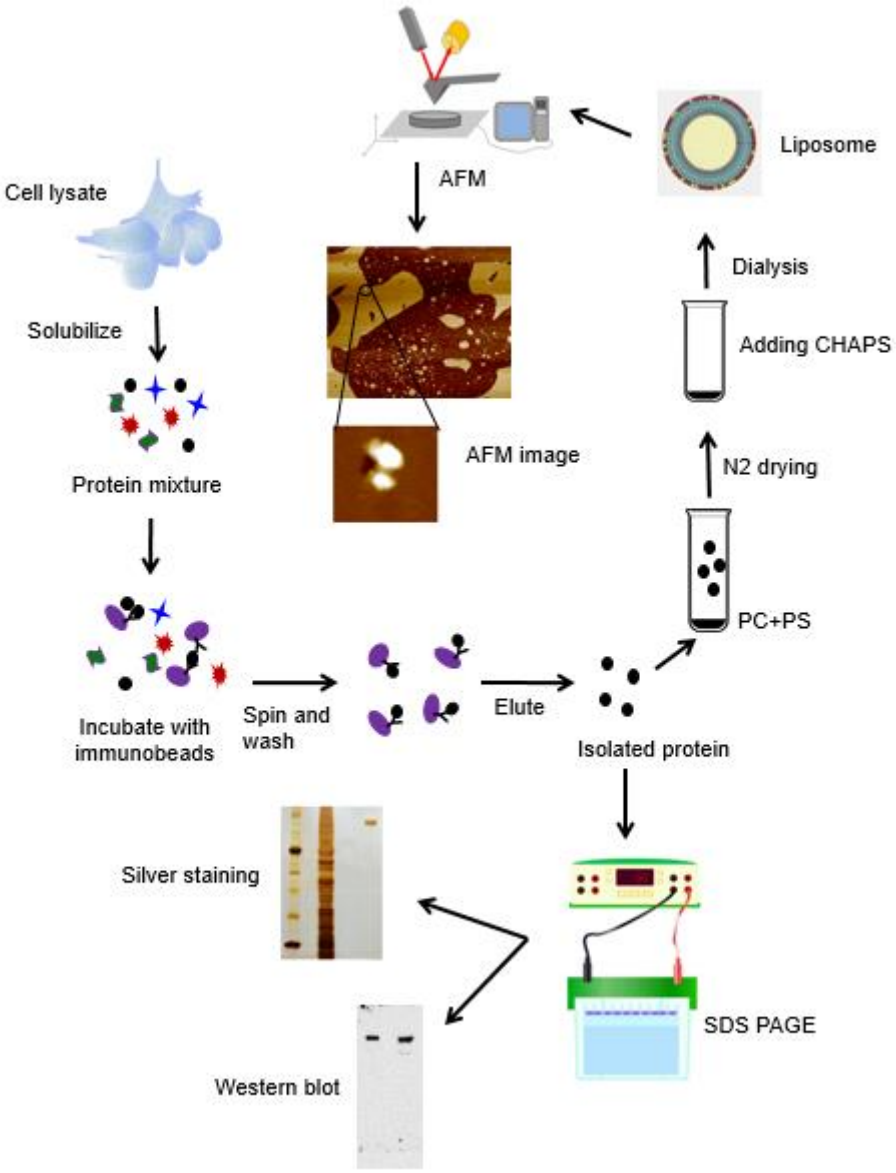

Figure 2.1. Schematic representation of the receptor isolation process and subsequent steps. The transfected cells were lysed and solubilized to remove any insoluble material. The soluble proteins were then trapped on anti-HA immunobeads and eluted with HA peptide. Isolated proteins were mixed with lipids and the mixture was dialysed to remove detergent, resulting in the formation of proteoliposomes. Protein purity was checked by silver staining and immunoblotting. Proteoliposomes were allowed to collapse onto mica supports to form supported lipid bilayers containing integrated receptors. Finally, receptor-containing bilayers were imaged using fast-scan AFM.

2.6 Integration of receptors into liposomes

Chloroform solutions of L-α-phosphatidylcholine (PC) and 1,2-dioleoyl-*sn*-glycero-3-phospho-L-serine (DOPS; Avanti Polar Lipids) were mixed at a molar ratio of 3:1. The chloroform was then evaporated under a stream of nitrogen gas, and the lipids were resuspended in HBS (100 mM NaCl; 50 mM HEPES, pH 7.6) and mixed with 200 µl of purified receptor in 2% (w/v) CHAPS to give a total lipid concentration of 2 mg/ml and a CHAPS concentration of 1%. The mixture was dialysed at 4°C against detergent-free buffer for 2 days, with several changes of buffer.

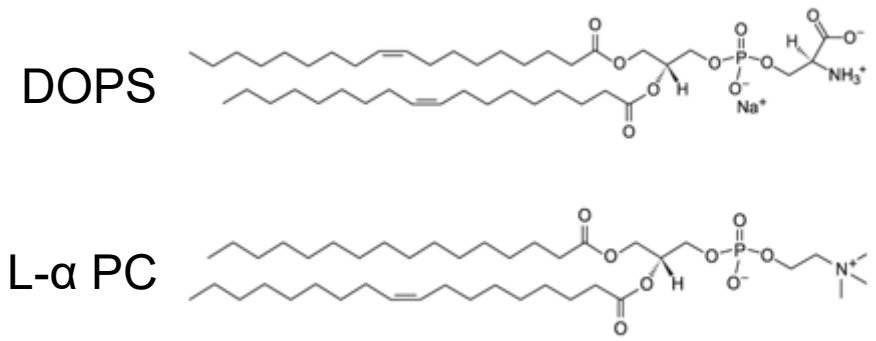

Figure 2.2. Structures of the phospholipids used.

2.7 Antibody decoration

The dialysed sample was incubated for 12 h at 4°C with either anti-HA or anti-V5 (negative control) monoclonal antibody at a dilution of 1:10,000.

2.8 Immunoblotting

Protein samples were prepared in Laemmli buffer and heated at 100°C for 5 min. SDS-polyacrylamide gel electrophoresis (SDS-PAGE) was carried out using a Bio-Rad Power Pac 200. Separated proteins were electrophoretically transferred onto a nitrocellulose membrane using a semi-dry system. The membrane was incubated in blocking buffer [5% (w/v) milk powder in Tris-buffered saline (TBS; 150 mM NaCl, 20 mM Tris base, pH 7.6) containing 0.01% (v/v) Tween] for 1 h to reduce non-specific binding. The membrane was then incubated overnight at 4°C with primary antibody (anti-HA), at a dilution of 1:1,000 in blocking buffer. The following day, the membrane was washed three times with blocking buffer and incubated with secondary antibody [horseradish peroxidase (HRP)-conjugated goat anti-mouse; Bio-Rad; 1:1,000 dilution

in blocking buffer] for 1 h. The membrane was again washed three times, and immunoreactive bands were visualized using enhanced chemiluminescence (ECL, Thermo Scientific).

2.9 Silver staining

The SDS-polyacrylamide gel was treated for 1 h with 50 ml fixative solution (200 ml ethanol, 50 ml acetic acid and Milli-Q water to 500 ml), followed by another 1 h incubation in 50 ml incubation solution (15 ml ethanol, 2.05 g anhydrous sodium acetate, 63.5 mg anhydrous sodium thiosulphate and water to 50 ml, to which 260 µl glutaraldehyde was added immediately before use). After washing three times in water, the gel was incubated for 40 min in 50 ml silver solution (50 mg silver nitrate and water to 50 ml, to which 100 µl of 4% paraformaldehyde was added immediately before use). Silver solution was removed and disposed of safely, and 50 ml of developer solution (1.25 g anhydrous sodium carbonate and water 50 ml, to which 100 µl of 4% paraformaldehyde was added immediately before use) was then added to the gel. Development was continued until protein bands appeared. Development was stopped by the addition of stop solution (7.3 g sodium-EDTA.2H_2O and water to 500 ml) for 10 min.

2.10 AFM imaging in fluid

A droplet (20 µl) of proteoliposome suspension was deposited onto the surface of a freshly cleaved mica disc (diameter, 1 cm). After incubation for 5 min at room temperature (20°C), the mica surface was gently washed several times with HBS to remove unadsorbed proteoliposomes. AFM imaging under fluid was carried out at room temperature using a Bruker-AXS FastScan Dimension AFM instrument. The instrument was used in micro-volume fluid mode to facilitate the application of agonist, antagonist or ions directly while imaging. All images were collected in ‘tapping’ mode, using FastScan-D silicon probes (Bruker). The cantilevers (with a typical spring constant of 0.25 N/m) were tuned to a resonance frequency of between 90 and 140 kHz. The microscope was engaged with a 2-µm scan area and 5-nm target amplitude to allow for tuning. The amplitude setpoint was adjusted to the highest setting that allowed imaging with little noise, to minimize the force applied to the sample. Images for receptor dynamics were captured at a rate of 1 frame/second with fixed integral gain of

2.5 and target amplitude of 1 nm. All other images were captured at a scan rate of 20 Hz (25 seconds/frame), and with 512 scan lines per area. High-magnification images were taken in a 120-nm scan area. 'Line-scanning' was carried out by disabling the Y scanning axis, allowing scanning of the receptor in the X dimension only. Each line took about 50 ms to capture.

2.11 Photolysis

UV photolysis (Optoflash; Cairn) was used to rapidly generate L-glutamate and thereby detect rapid changes in the height of individual GluK2 receptors using fast-scan AFM imaging. Samples were placed onto mica without the usual supporting metal puck to allow the transmission of UV light in order to uncage 4-methoxy-7-nitroindolinyl-caged-L-glutamate (MNI-caged-L-glutamate; Tocris Bioscience).

2.12 Data analysis

Image analysis was performed using the Nanoscope analysis 1.5 software and ImageJ. Data analysis was carried out using Microsoft Excel, OriginPro 8.5 or SigmaPlot 12.5.

Histograms were drawn with bin widths chosen according to Scott's equation:

$$h=3.5\sigma / n^{1/3},$$

where h is the bin width, σ is an estimate of the standard deviation and n is the sample size.

In order to quantitate ATD mobility, the centres of the ATD particles were obtained using Gaussian fitting (ImageJ plug-in: Adrian's FWHM). The significance of differences between two normal distributions was determined using a Student's paired two-tailed *t*-test. $P<0.01$ was taken as significant. A Mann-Whitney U-test was applied for nonparametric data. One-way ANOVA and post-hoc tests were used to compare different independent events in ATD mobility data. $P<0.05$ was taken as significant. All errors are reported as standard error of the mean (S.E.M.).

2.13 Antibodies

The following antibodies were used:

Mouse monoclonal anti-V5 (InVitrogen; R960-25), mouse monoclonal anti-HA (Covance; HA.11 clone 16B12, MMS-101P), horseradish peroxidase-conjugated goat anti-mouse; (Bio-Rad-1706516) and fluorescein isothiocyanate-conjugated goat anti-mouse (Sigma; F8771).

3. Visualization of structural changes accompanying activation of kainate receptors

3.1 Introduction

3.1.1 Activation and desensitization in iGluRs

Three conventional conformational states recognized in most iGluRs are the resting, activated and desensitized states. More than 150 structures of the isolated domains, as well as full-length iGluR receptors, have revealed many functional features of AMPA and kainate receptors (Mayer, 2011). However, even now, we are not completely confident about the structural basis of agonist activation, of the action of allosteric modulators, and of receptor desensitization (Dürr *et al.,* 2014). In particular, we still do not understand the molecular mechanisms underlying the conformational changes leading to the active and desensitized states.

Unlike trimeric P2X receptors (Marquez-Klaka *et al*., 2007) and pentameric Cys-loop receptors (Pedersen and Cohen, 1990), the crystal structures of iGluRs confirm that the agonist binding sites are placed within the clefts of individual subunit 'clamshells' and not at the interfaces between subunits (Sobolevsky *et al.,* 2009). This finding underlies the many structural and biophysical experiments on soluble LBDs of AMPA (Armstrong and Gouaux, 2000; Armstrong *et al.,* 2006), kainate (Mayer, 2005; Weston *et al.,* 2006), and NMDA receptors (Furukawa *et al*., 2005; Inanobe *et al.,* 2005; Yao *et al*., 2008).

The upper part of the LBD clamshell (D1) forms an interface with the LBD of an adjacent subunit within an LBD dimer, whereas the lower lobe (D2) appears relatively free to move (Horning and Mayer, 2004; Furukawa *et al.,* 2005; Mayer, 2005; Naur *et al.,* 2007; Sobolevsky *et al.,* 2009). Binding of glutamate to the D1 region of the LBD clamshell triggers activation of the receptor followed by clamshell closure through the movement of D2; as a result, a rotation of the LBD dimer assembly occurs. Eventually this rotation creates compensatory energy elsewhere in the protein, resulting in the opening of the channel pore (Meyerson *et al.,* 2014; Sun *et al.,* 2002).

Unfortunately, the exact mechanism of opening of the channel through conformational changes in the LBD region is as yet unknown. One of the reasons for this is the lack of an intact structure of the receptor in presence of full agonist. However, there is evidence

supporting the idea that movement of D2, which contains the anchor points in full-length receptors, extends to the ion channel-containing transmembrane segments M1 and M3, and exerts a 'pulling' force on the D2-M3 linker region, leading to channel opening. In fact, the M3 helix is crucial to channel gating, as mutations in the M3 segment significantly affect receptor function (Kohda *et al*., 2000; Jones *et al.*, 2002; Yuan *et al.,* 2005). Moreover, superimposition of *apo* and agonist-bound structures of LBD dimers reveals that the length between the linkers below the D2 region is longer in the agonist-bound structure. This is in agreement with the activation model for the AMPAR (Erreger *et al*., 2004; Mayer, 2006; Hansen *et al*., 2007). In addition, on the basis of homogeneity between the M3 segment of the glutamate receptor and the inner helix of the K^+ channel (Doyle *et al.,* 1998; Jiang *et al.,* 2002; Alam and Jiang, 2009; Yellen, 2002; Swartz, 2004), Sobolevsky *et al*. (2009) speculate that gating of iGluRs largely depends on the rotation of the M3 helices, which resembles the role of the inner helix in the opening of the K^+ channel.

The strain in the GluA2 AMPAR caused by the pulling down of the ATD by the D1 lobe and the opening of the channel by D2 lobe through lateral and upward forces can be released by the transition of the receptor to the desensitized state, in which the channel closes while the LBD remains in the closed-cleft, glutamate-bound conformation (Meyerson *et al.,* 2014). The initial step in desensitization is the rupture of the D1-D1 dimer interface between LBDs of adjacent subunits, which results in closing of the ion channel (Fig. 1.7; Sun *et al.*, 2002; Horning and Mayer, 2004). It is notable that GluA2-L483Y, a mutant that blocks desensitization, or the GluA2 desensitization inhibitor cyclothiazide (CTZ), stabilize this LBD dimer interface, suggesting that stabilization of the LBD dimer interface in full-length functional AMPARs can reduce desensitization (Sun *et al.,* 2002). Now the question is how in the desensitized state does the receptor maintain both a closed cleft in the LBD and a closed channel in the ion pore, since the molecular tension induced in the closed-cleft conformation should be released in the latter conformation? Meyerson *et al.* (2014) answered this question by establishing that the two-fold symmetry of the LBD layer is replaced by four-fold symmetry in the desensitized state, which matches the four-fold symmetry in the conducting pore of the transmembrane domain, so that eventually

tension shifts to the two-fold symmetrical ATD layer. In this way the receptor achieves a low-energy, stable conformation (Fig. 3.1B, C).

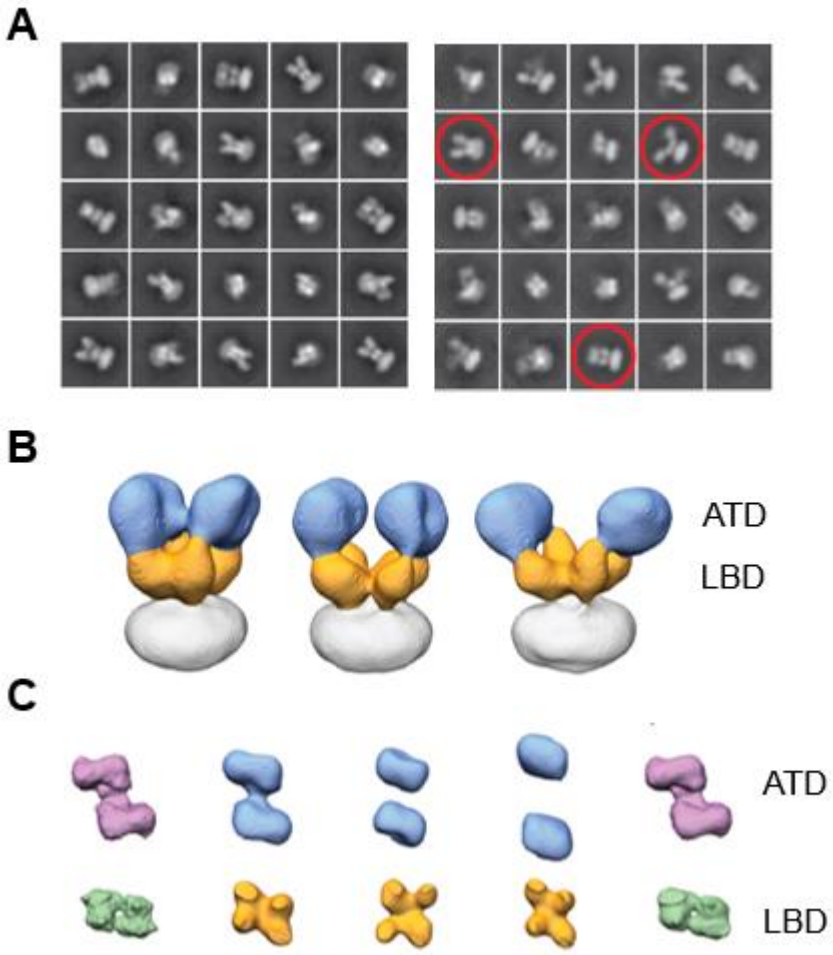

Figure 3.1. Cryo-EM images of GluA2 AMPARs in the active and desensitized states (Meyerson *et al.,* 2014). (A) Representative 2D class averages of cryo-EM structures of GluA2 in the active state (left montage) and the desensitized state (right montage). Selected images (red circles, right montage) indicate the range of observed conformations in the desensitized state. (B) Representations of three distinct desensitized states in GluA2 cryo-EM structures. ATD and LBD layers are identified in blue and orange, respectively. (C) Top views of ATD and LBD layers for the three desensitized states (centre) separating those for the active state (left) and the restored active state (right).

Another important feature in non-NMDA iGluRs is partial agonism, where drugs induce different degrees of cleft closure that correlate with their relative efficacy. In

this way, each subunit of the receptor can partially increase the opening probability of the gate (Partin *et al.*, 1994; Jin *et al*., 2003). For instance, a lesser degree of cleft closure has been observed in the GluK2 receptor complexed with the partial agonist kainate compared to the full agonist glutamate (Mayer, 2005). In contrast, no such relationship has been reported between the degree of agonist-induced cleft closure and agonist efficacy in NMDARs. A typical example in this regard is seen with the full agonist glycine and the partial agonist D-cycloserine, both of which show the same degree of domain closure upon activation of the receptor (Furukawa and Gouaux, 2003; Furukawa *et al*., 2005; Inanobe et al., 2005).

Although different iGluRs are alike in gating mechanism, they are diverse in their gating kinetics (Lester *et al.*, 1990); for example, there are different response time-courses among receptor subtypes, specific subunits within each subtype, and alternative RNA splice variants. Post-translational modifications, and the presence of accessory subunits, also affect gating kinetics. Among the three major iGluR types, AMPA and kainate receptors show fast activation and deactivation rates as well as both rapid and strong desensitization in the millisecond time-scale (Mosbacher *et al.*, 1994; Edmonds *et al.*, 1995; Erreger *et al.*, 2004); for instance, in the presence of glutamate, GluA2 desensitizes within 4-8 ms and exhibits a 98.5% decrease in current amplitude in the desensitized state (Horning and Mayer, 2004; Robert *et al.*, 2005). By contrast, NMDARs exhibit slower gating kinetics, activating in milliseconds and deactivating within tens or thousands of milliseconds, and a slower, weaker onset of desensitization, which is almost absent in GluN2C- and GluN2D-containing NMDA receptors (Monyer *et al.*, 1994; Krupp *et al.*, 1996; Wyllie *et al.*, 1998; Dravid *et al*., 2008).

3.1.2 Desensitization in KARs

GluA2 and GluK2 share about 73% amino acid sequence similarity in their ion channel domain (Meyerson *et al.*, 2014), but show some differences in gating behaviour. For instance, unlike the AMPAR, KAR desensitization cannot be blocked by allosteric modulators, though cross-linking or mutation at the dimer interface can attenuate desensitization (Priel *et al.*, 2006; Weston *et al.*, 2006; Nayeem *et al.*, 2009; Chaudhry *et al.*, 2009). Fig. 3.2 shows the positions of two well-characterized desensitization mutations of GluK2, namely D776K and Y521C/L783C. The figure also shows the presence of two Na^+ ions at the D1-D1 interface; dissociation of these ions in response

to activation leads to desensitization. The 776K residue acts as a tethered cation that substitutes for the Na^+ ions and also interacts with the adjacent subunit, thereby preventing desensitization. Another difference between GluK2 and GluA2 is that GluA2 has much weaker interactions between the ATDs compared with GluK2, which might at least partially account for the rapid desensitization rate in AMPA receptors.

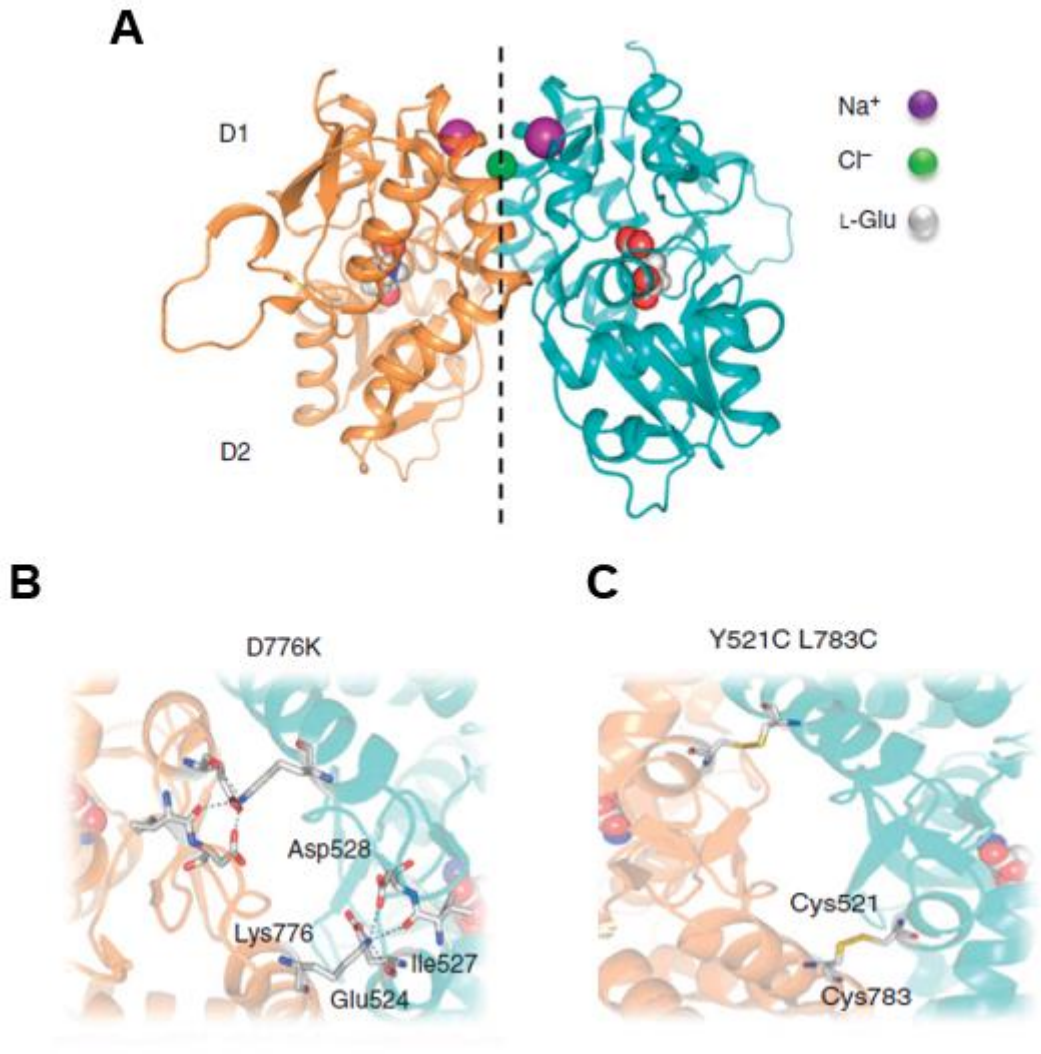

Figure 3.2. Control of desensitization at the level of the GluK2 LBD dimer. (A) Crystal structure of the wild-type GluK2 LBD dimer, including the upper (D1) and lower (D2) domains. (B) Top view of the LBD dimer interface of the desensitization blocking mutant GluK2 D776K, showing electrostatic interactions between K776 and the adjacent subunit. (C) Top view of the GluK2 Y521C/L783C LBD dimer interface showing covalent cross-linking between subunits, which attenuates desensitization (Dawe *et al*., 2013).

3.1.3 Aims

In this chapter, I describe the use of fast-scan AFM imaging to explore the effects of activation and desensitization of the GluK2 kainate receptor on the global structure of the receptor. I explore the effects of L-glutamate on the heights of wild type and mutant KARs, and use UV photolysis of caged L-glutamate to follow the kinetics of the observed height changes using AFM in 'line scanning' mode. Finally, I investigate the effect of activation on the mobility of the ATDs of the receptor.

3.2 Results

3.2.1 Immunofluorescence detection of GluK2 receptor in transiently transfected cells

Immunofluorescence was used to confirm the expression of GluK2 receptors in transfected tsA 201 cells. As shown in Fig. 3.3, at least half of the cells expressed GluK2, which was distributed throughout the cell cytoplasm.

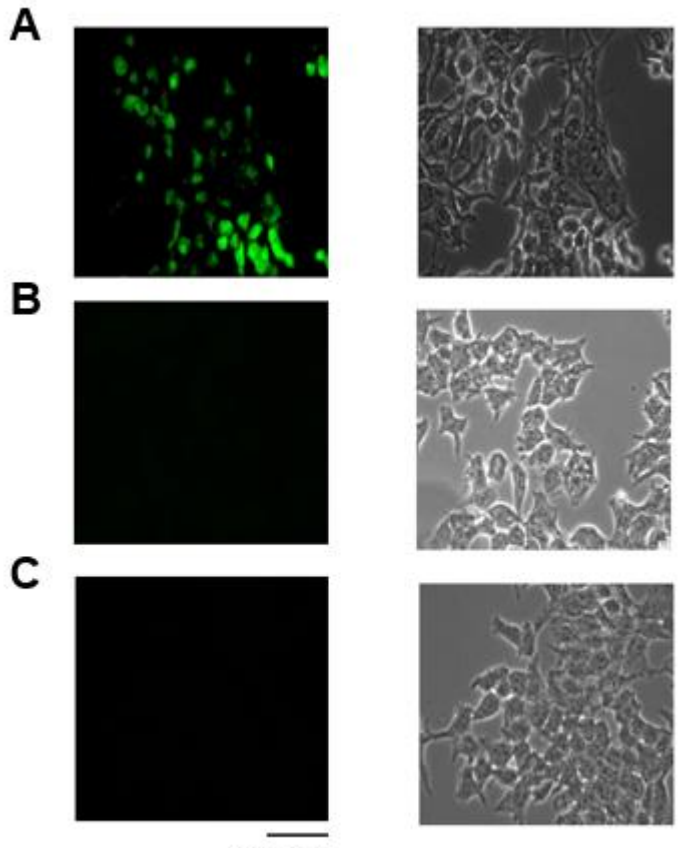

Figure 3.3. Immunofluorescence detection of GluK2; Scale bar, 50 µm (A) Cells were transfected with DNA encoding HA-GluK2. Cells were fixed, permeabilized and incubated with mouse monoclonal anti-HA antibody, followed by FITC-conjugated goat anti-mouse secondary antibody. (B) As in (A), except that the mouse monoclonal anti-HA antibody was replaced by mouse monoclonal anti-V5 antibody (control). (C) As in (A), except that cells were untransfected. The left-hand panels show the immunofluorescence images, and the right-hand panels show bright-field images of the same areas.

3.2.2 Immunoaffinity purification of the GluK2 kainate receptor

HA-GluK2 was isolated from a detergent extract of tsA 201 cells by anti-HA immunoaffinity chromatography. Analysis of the isolated GluK2 sample on a silver-stained gel revealed the presence of a single band at approximately 116 kDa, indicating the purity of the sample. Immunoblotting using an anti-HA antibody indicated that the band was indeed GluK2 (Fig. 3.4).

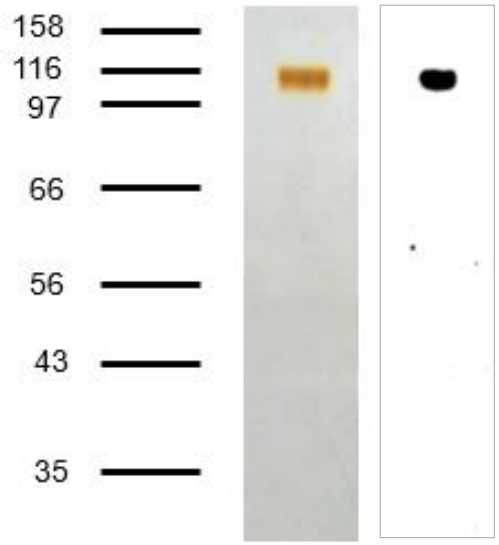

Figure 3.4. Analysis of isolated GluK2. Silver stain (left panel) and immunoblot (right panel), using an anti-HA antibody.

3.2.3 Visualization of the GluK2 receptor integrated in lipid bilayer by AFM

Isolated GluK2 was integrated into liposomes (3:1 PC/PS), and the proteoliposomes were deposited onto a mica surface to produce a supported proteolipid bilayer. Images were captured at a scan rate of 20 Hz with 512 scan lines per area (i.e. 25 s/frame). Fig. 3.5A shows an AFM image of a plain (protein-free) lipid bilayer. As can be seen, the bilayer is smooth and featureless. In contrast, a bilayer containing integrated GluK2 receptors has several protruding particles (Fig. 3.5B). Application of the AFM section tool revealed a bilayer thickness of 3.7±0.1 nm (n=24). A frequency distribution of heights of the particles in the bilayer revealed two height populations, at 3.65±0.10 nm and 6.37±0.20 nm (n=486; Fig. 3.5C).

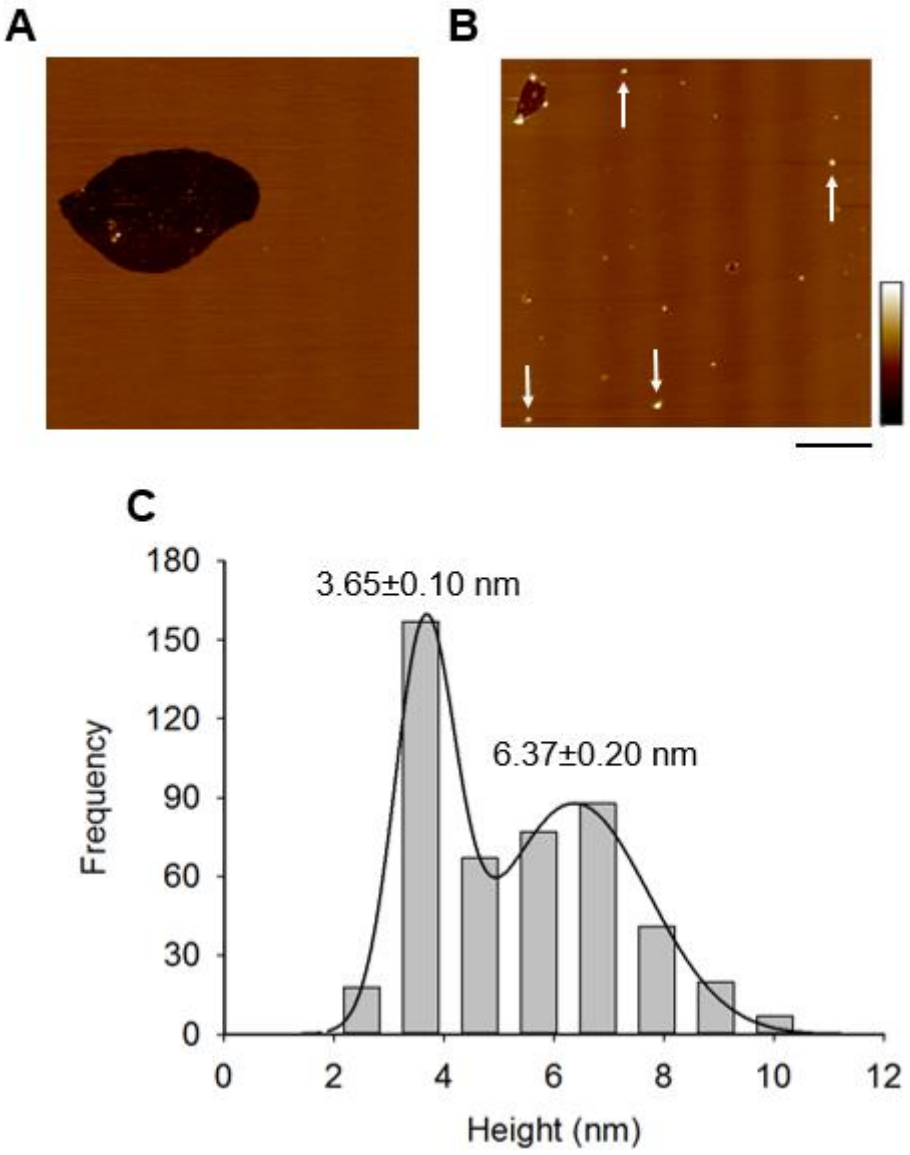

Figure 3.5. AFM imaging of bilayer-integrated GluK2. (A) Image of a protein-free bilayer. (B) Image of a bilayer containing integrated GluK2. Arrows indicate assembled receptors. Scale bar, 400 nm; colour-height scale, -5 to 5 nm. (C) Frequency distribution of heights of the GluK2 particles in the bilayer (n=486). The curve indicates the fitted Gaussian functions. The peaks of the distribution (±SEM) are indicated.

To understand the significance of the two particle populations, I decorated the receptors with an anti-HA antibody, which recognizes the HA epitope present at the N terminus of each subunit. When the anti-HA antibody itself was imaged in association with a lipid bilayer (Fig. 3.6A), the mean height of the particles was found to be 2.10±0.10 nm (n=7). Proteoliposomes were then incubated with the antibody. Fig. 3.6B shows an AFM image of a bilayer containing GluK2 that had been incubated with the anti-HA antibody. Antibody-decorated particles could occasionally be seen (arrow). A gallery of zoomed images of decorated GluK2 particles is shown in Fig. 3.6C. Importantly, no decorated particles were seen when a control antibody (anti-V5) was used. A frequency distribution of the heights of the antibody-decorated particles had a single peak at 6.57±0.14 nm (n=41; Fig. 3.6D), demonstrating that the larger particles in the original distribution (Fig. 3.5C) represent the extracellular regions of the receptor. From this point on, particles of height 6-8 nm were assumed to represent iGluR homotetramers, and were included in analyses. The smaller particles likely represent a mixture of unfolded or incompletely assembled receptors, together with receptors integrated into the bilayer cytoplasmic side-up.

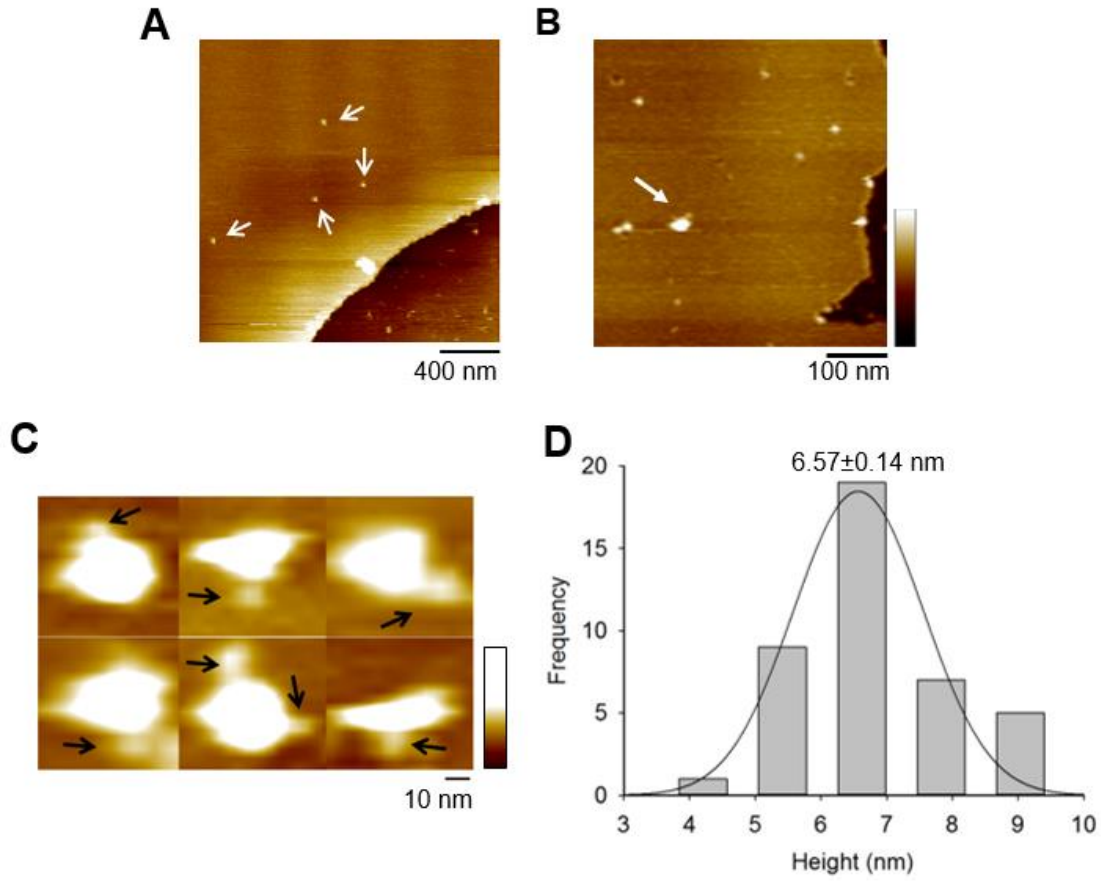

Figure 3.6. Decoration of bilayer-integrated receptors with anti-HA antibodies. (A) AFM image of anti-HA antibodies resting on a lipid bilayer. Scale bar, 400 nm; colour-height scale, -5 to 5 nm. (B) AFM image of a bilayer containing receptors after incubation with anti-HA antibody. A decorated GluK2 receptor is indicated by the arrow. Scale bar, 100 nm; colour-height scale, -5 to 5 nm. (C) Gallery of zoomed images of antibody-decorated GluK2 particles. Arrows indicate the bound HA antibodies. Scale bar, 10 nm; colour-height scale, 0-7 nm. (D) Frequency distribution of heights of decorated receptor particles (n=41). A fitted Gaussian curve is overlaid on the histogram. The peak of the distribution is indicated.

In high-magnification (120 nm x 120 nm) images, the receptors appeared as double-blob structures (Fig. 3.7). Based on X-ray and cryo-EM structures (e.g. Meyerson *et al.*, 2014), each blob is likely to contain ATDs from two subunits. A zoomed AFM image of one of these double-blob structures is shown in Fig. 3.7B, alongside a cryo-EM image of GluA2 ATDs for comparison (Meyerson *et al.*, 2014). A 3D representation of the same AFM image is shown in Fig. 3.7C. Note that the two blobs had different heights, suggesting a tilting of the extracellular region of the receptor. This phenomenon was seen in many images.

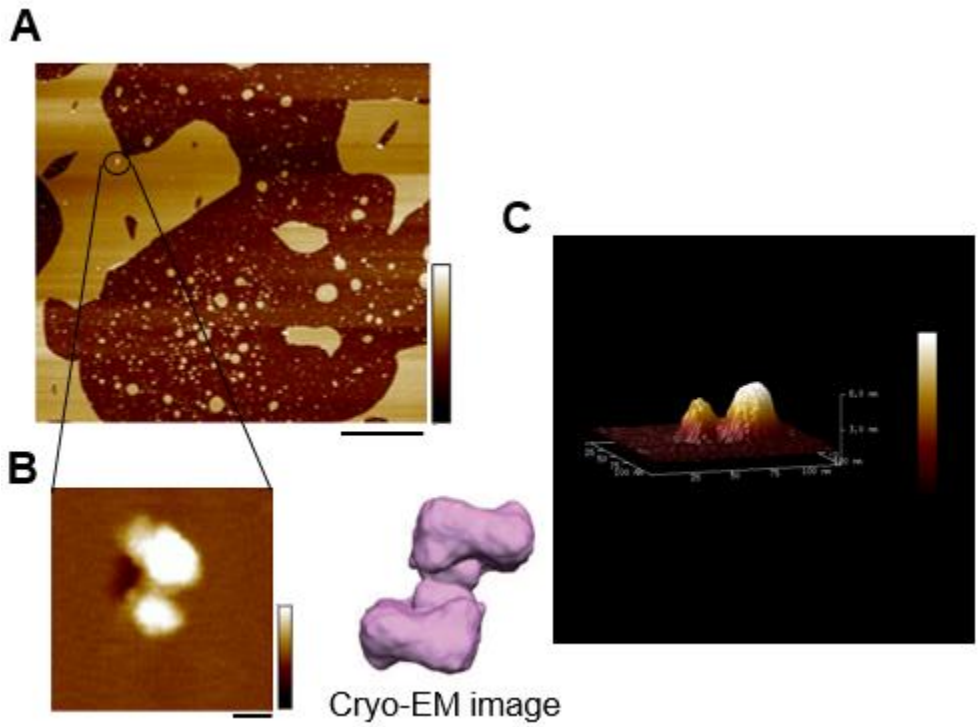

Figure 3.7. High-magnification AFM images of KARs reveal double-blob structures. (A) Overview of an area of bilayer, containing an individual KAR. Scale bar, 1 µm; colour-height scale, -5 to 5 nm. (B) High-magnification image of the same KAR. Scale bar, 20 nm; colour-height scale, -5 to 5 nm. A cryo-EM image of the ATD region of the GluA2 AMPA receptor is shown for comparison. (C) 3-D image of the same particle shown in (B). Colour-height scale, 0-8 nm.

A gallery of double-blob structures is shown in Fig. 3.8A. A common artefact of AFM imaging is ‘double tipping’, caused by a contaminating particle adhering to the tip, which scans the sample in parallel with the tip, creating a double image of every feature. A characteristic of double tipping is that the alignment of the pairs of structures remains fixed as the angle of scanning is changed. To exclude the possibility that the double particles were a result of double tipping, I captured images of the same particle by scanning at different angles (0°, 45°, 90°). As shown in Fig 3.8B, the alignment of the double-blob structure changed with the scanning angle, ruling out this artefact.

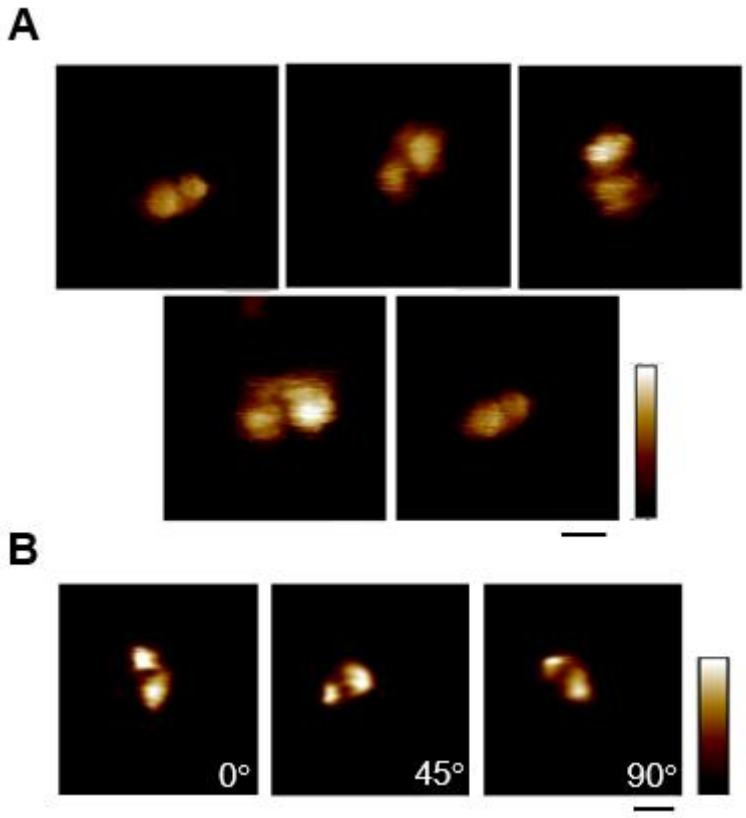

Figure 3.8. High-magnification images of KARs. (A) Gallery of zoomed (120 nm x 120 nm) AFM images of GluK2 particles. Scale bar, 20 nm; colour-height scale, 0-10 nm. (B) Images of the same particle taken at three scanning angles (0°, 45°, 90°). Scale bar, 20 nm; colour-height scale, 0-5 nm.

To confirm that the double-blob structures were individual GluK2 receptors, I captured high-magnification images (120 nm x 120 nm) of anti-HA antibody-decorated particles. Images of two large blobs (ATDs) singly or doubly decorated with smaller blobs (antibodies) are shown in Fig. 3.9.

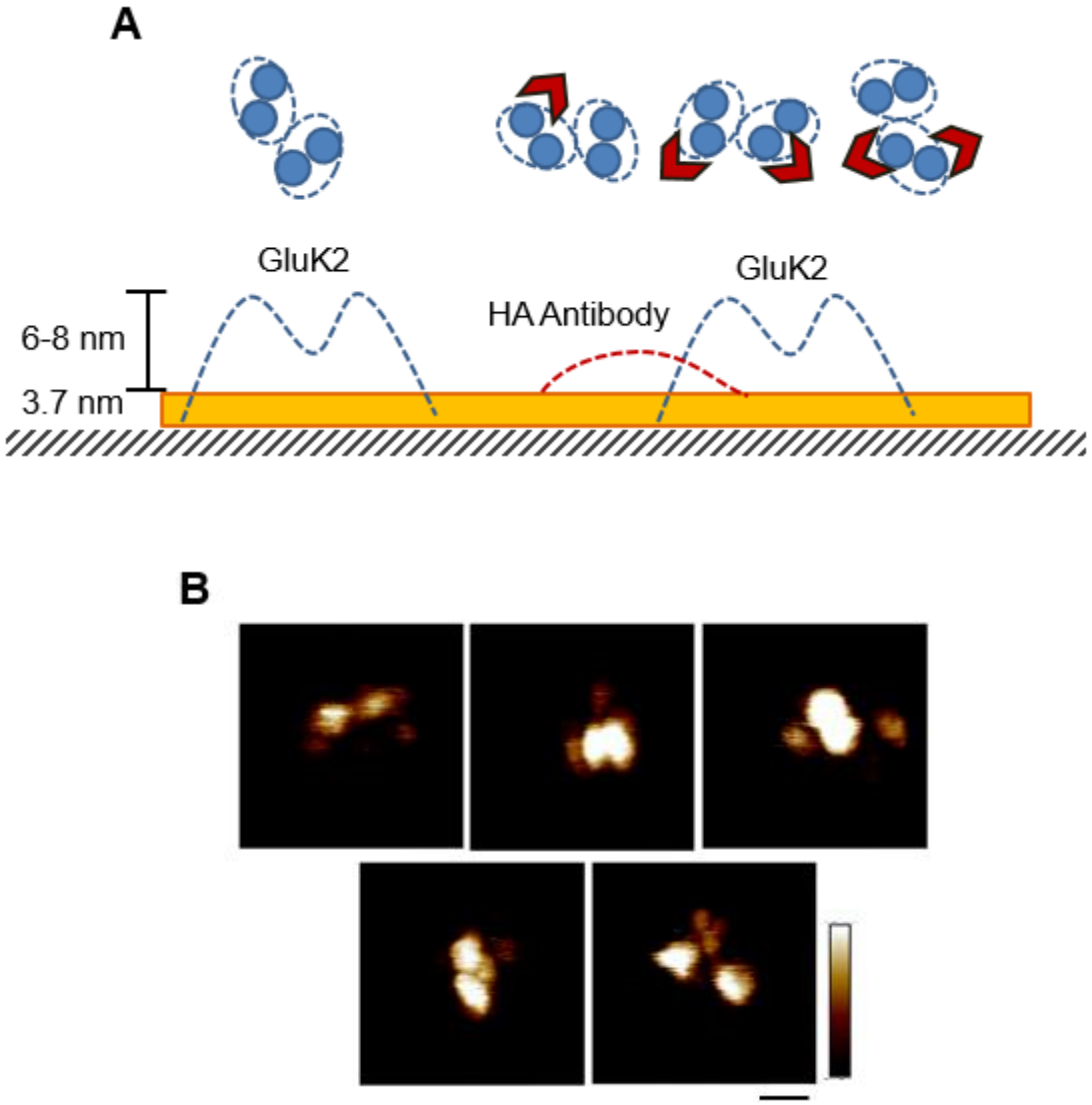

Figure 3.9. Antibody decoration of double-blob structures. (A) Schematic representation of antibody-decorated GluK2 receptors. Each large blob represents a dimer of ATDs (blue circles). These large blobs are decorated by with one or two antibodies (red chevrons). (B) Gallery of zoomed (120 nm x 120 nm) AFM images of immunoisolated GluK2 particles singly or doubly decorated with anti-HA antibodies. Scale bar, 20 nm; colour-height scale, 0-5 nm.

3.2.4 Effect of L-glutamate on GluK2 receptor height

In a first series of experiments to determine the effect of activation of GluK2 receptor height, I imaged the same area of bilayer sequentially at a rate of one frame every 25 s. A small volume of solution containing L-glutamate (final concentration, 100 μM) was then injected into the imaging chamber while particles of interest were imaged repetitively. Images of a representative particle before and after L-glutamate application are shown in Fig. 3.10A. The sections through the particle, shown in Fig. 3.10B, indicate that the particle height fell from 6.80 nm to 5.92 nm in response to L-glutamate application. Note that the thickness of the supported lipid bilayer was unaffected by L-glutamate. Significantly, no activation-induced height change was seen for particles that were less than 5 nm tall.

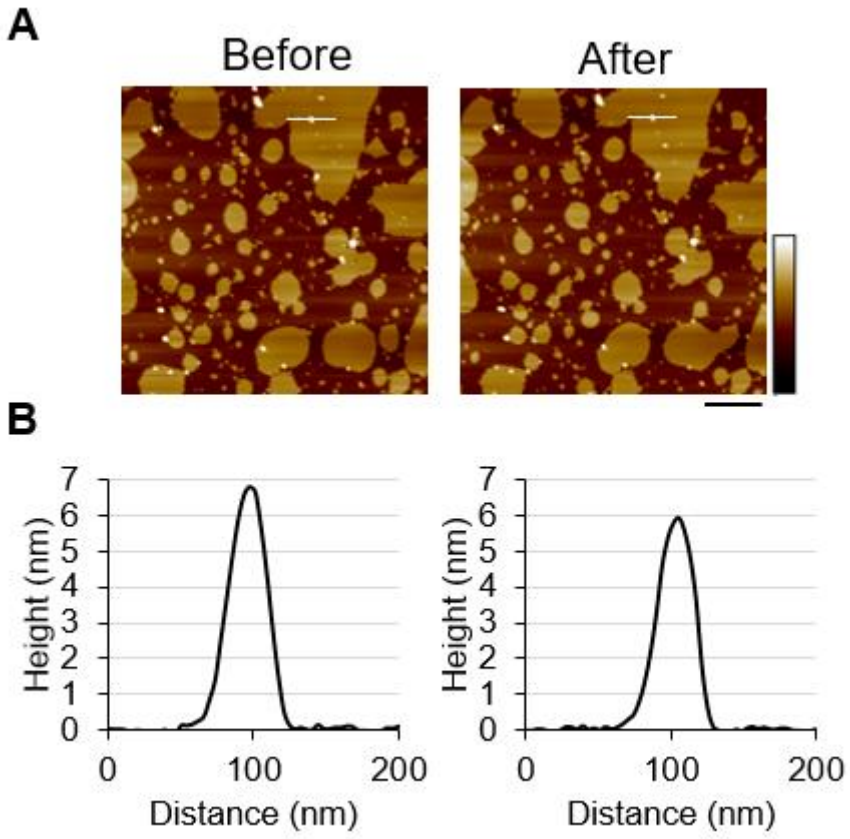

Figure 3.10. Effect of L-glutamate on GluK2 receptor height. (A) Representative AFM images of a bilayer containing GluK2 receptors before (left) and after (right) application of L-glutamate (100 μM). Scale bar, 400 nm; colour-height scale, -5 to 5 nm. (B) Sections through the receptor at the position indicated by the line in (A). Peak heights are 6.80 nm before and 5.92 nm after addition of L-glutamate.

I next tested the effect of the competitive GluK2 receptor antagonist CNQX (500 μM) on the change in height of the receptor in response to L-glutamate. Representative images before and after addition of L-glutamate in the presence of CNQX are shown in Fig. 3.11A. In this case the receptor heights were 6.80 nm before and 6.90 nm after addition of L-glutamate (Fig. 3.11B).

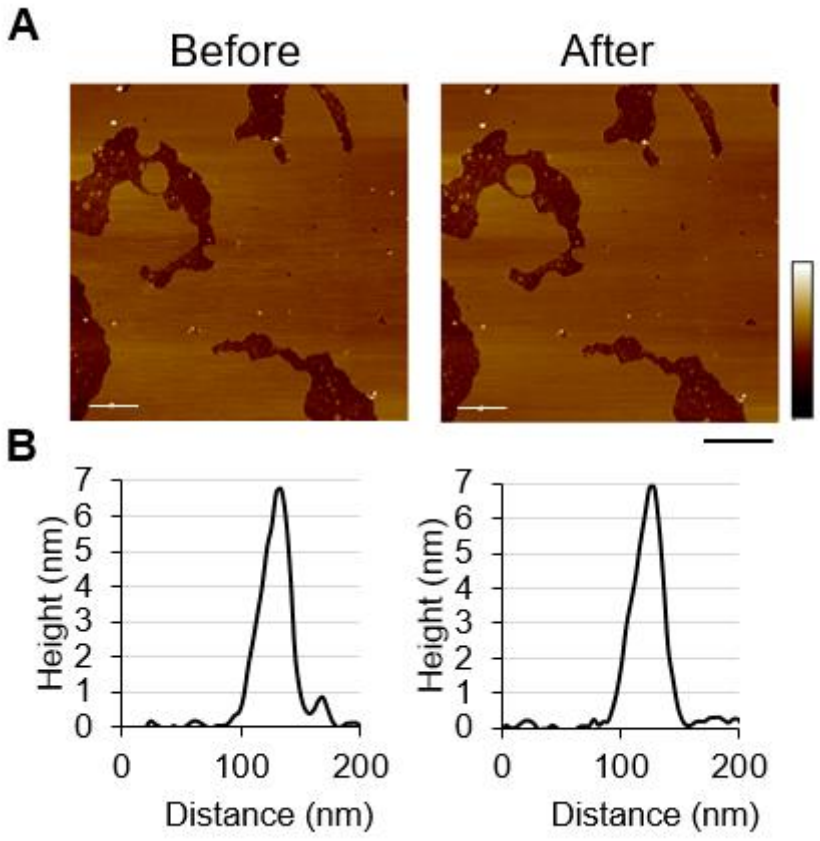

Figure 3.11. CNQX inhibits the effect of L-glutamate on GluK2 receptor height. (A) Representative AFM images of a bilayer containing GluK2 receptors before (left) and after (right) application of L-glutamate (100 μM) in the presence of CNQX (500 μM). Scale bar, 400 nm; colour-height scale, -5 to 5 nm. (B) Sections through the receptor at the position indicated by the line in (A). Peak heights are 6.80 nm before and 6.90 nm after addition of L-glutamate plus CNQX.

In a number of replicates of the above experiments, the mean height of the receptors before L-glutamate application was 7.14±0.10 nm (n=20), and the height fell to 6.29±0.10 nm (n=20) after L-glutamate application (P<0.001; Fig. 3.12A, C). When L-glutamate was applied in the presence of CNQX the height of the receptor remained unchanged: 6.93±0.20 nm (n=20) before and 6.93±0.17 nm (n=20) after drug application (Fig. 3.12B, C).

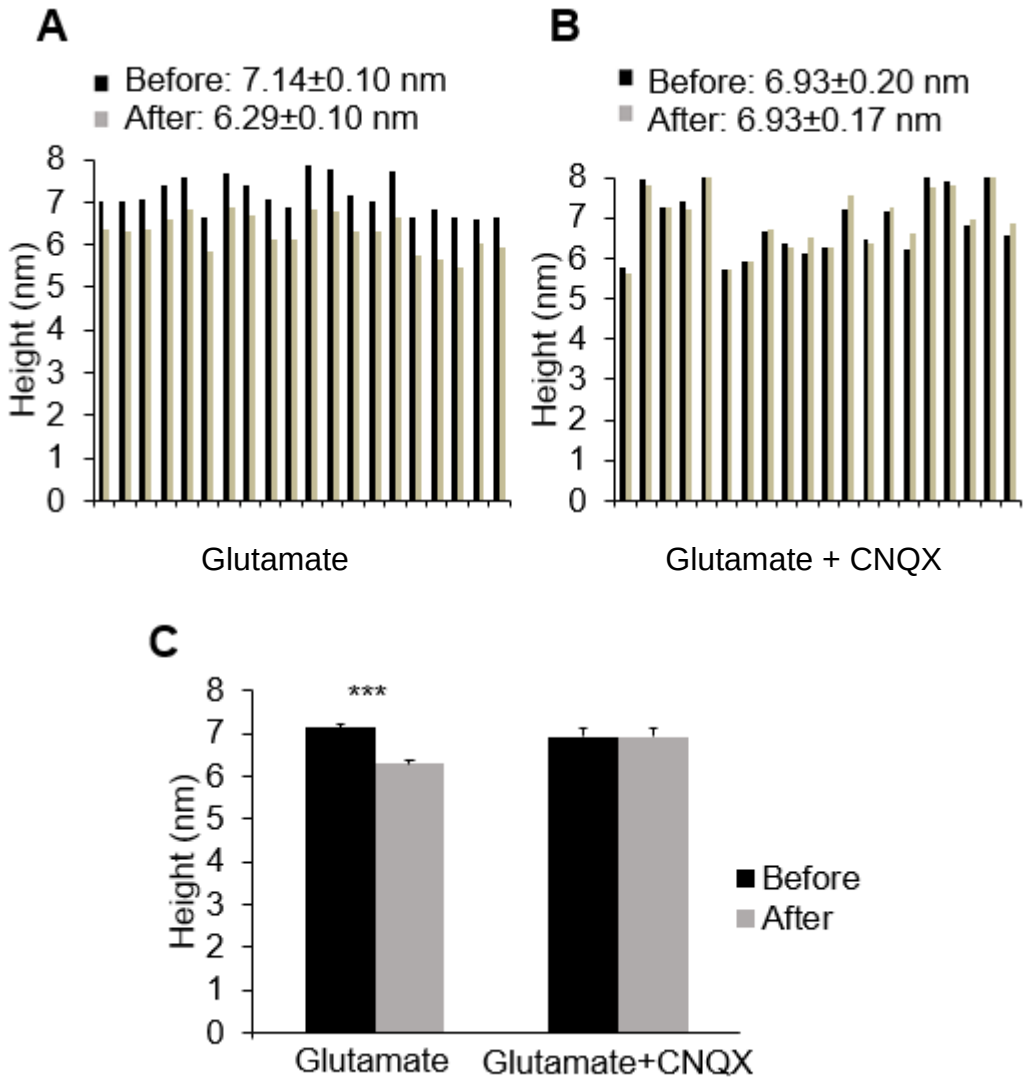

Figure 3.12. Particle heights before and after application of drug(s). (A) Effect of L-glutamate only (100 μM). (B) Effect of L-glutamate in the presence of CNQX (500 μM). (C) Comparison of the results for the two conditions. Triple-asterisks indicate a highly significant change in receptor height following L-glutamate (P<0.001, Student's paired two-tailed *t*-test).

3.2.5 Effect of photolytic uncaging of L-glutamate on GluK2 receptor height

To control the activation of the GluK2 receptor more precisely, I combined fast-scan AFM imaging with photolysis of caged L-glutamate (MNI-glutamate, 100 μM). The mean height of the particles before photolysis was 6.79±0.12 nm (n=12), and after photolysis the height fell to 6.02±0.12 nm (n=12; $P<0.001$; Fig. 3.13A, C). The thickness of the supported lipid bilayer was unaffected by uncaging of the L-glutamate. Importantly, uncaging of L-glutamate in the presence of CNQX (500 μM) did not significantly affect the height of the receptors (7.19±0.22 nm before and 7.16±0.23 nm after drug application; n=13; Fig. 3.13B, C).

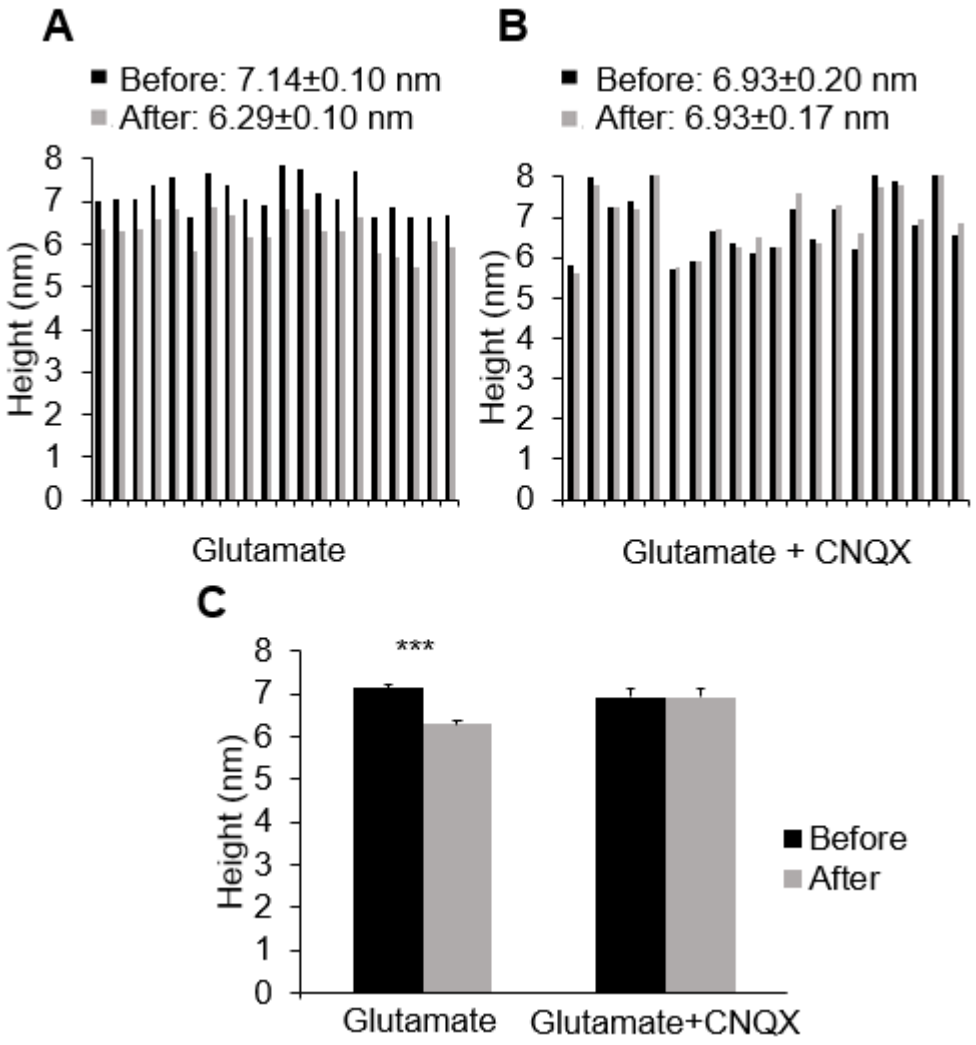

Figure 3.13. Particle heights before and after uncaging of L-glutamate. (A) Effect of L-glutamate only (100 μM). (B) Effect of L-glutamate in the presence of CNQX (500 μM). (C) Comparison of the results for the two conditions Triple-asterisks indicate a highly significant change in receptor height following UV irradiation ($P<0.001$, Student's paired two-tailed *t*-test).

3.2.6 Recording of activation-induced structural changes in the KAR by line scanning

So far, the rate of imaging has been one frame every 25 s, which is far too slow to follow any activation-induced structural changes. I therefore moved to 'line-scanning', where the Y scanning axis is disabled and the receptor is scanned back and forth in the X dimension (Fig. 3.14A). Under these conditions, the Y axis represents time. Each scan line takes about 50 msec to capture, which, combined with UV photolysis of MNI-caged-glutamate, should allow me to obtain a better picture of the structural changes occurring in response to activation. UV illumination was triggered halfway through the scanning period, so the first and second halves of the frame represent the receptor profile before and after UV photolysis, respectively. Fig. 3.14B shows a number of representative traces obtained under different conditions using line scanning. Three features of the data were analysed - the extent of the height change, the rate of the height change, and the fluctuations in height before and after activation.

To determine the extent of the height change, I fitted the data for the first and the last 8 s of each trace to a Gaussian curve. The mean heights for individual particles before and after activation are shown in Fig. 3.14C. Consistent with results reported above, the wild type receptor underwent a vertical compression of 0.75±0.16 nm in response to uncaging of L-glutamate (100 μM). No vertical compression occurred in response to either L-glutamate uncaging in the presence of CNQX (500 μM), or to UV irradiation in the absence of drug. Significantly, the D776K point mutant, which is known not to desensitize (Dawe *et al.,* 2013), did not respond to L-glutamate uncaging. This result indicates that the vertically compressed receptor represents the desensitized state. It also reveals that no detectable height change occurs as the receptor enters the active state. By contrast, the L783C point mutant behaved as the wild type receptor. This interesting mutant does not generate currents in response to activation (Dawe *et al.,* 2013), but rather appears to desensitize very rapidly, likely because it allows water into the cation binding pocket between the LBDs, which displaces the bound Na^+.

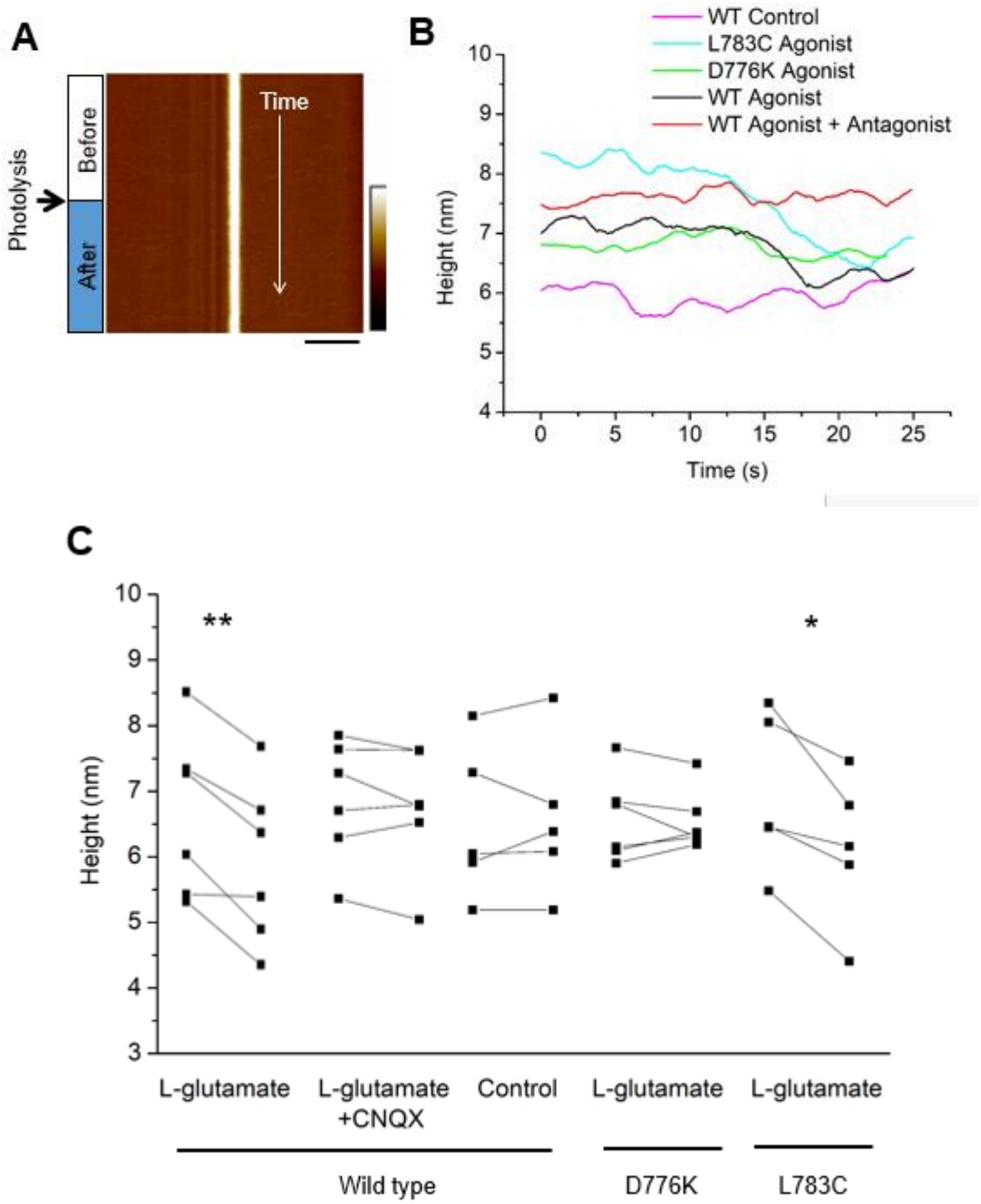

Figure 3.14. Line scanning analysis. (A) The vertical strip represents a series of sections through the receptor, which is scanned back and forth in the X dimension. UV photolysis began halfway through the recording, as indicated. Scale bar, 100 nm; colour-height scale, -5 to 5 nm. (B) Time-courses of height changes under various conditions. UV photolysis began at 12.5 s. (C) Height data for individual receptors before and after UV photolysis. Asterisks indicate a significant change in receptor height following UV irradiation ($P<0.01$, Student's paired two-tailed *t*-test).

According to Fig. 3.14B, the vertical compression in response to uncaging of L-glutamate occurs over a period of several seconds. The time-courses of compression for a number of receptors were fitted exponentially using the equation:

$$H_t = H_{final} + \Delta H.e^{-t/\tau},$$

where H_t is the particle height at time t, the time after the start of UV irradiation, H_{final} is the mean height over the last 8 s of recording, ΔH is the total vertical compression, and τ is the time constant of the decay. A typical fit for L-glutamate action on a wild type receptor is shown in Fig. 3.15 The mean values obtained for τ for the two cases where a reproducible vertical compression was seen were 4.1 s (n=6) for the wild type receptor and 5.6 s (n=4) for the L783C mutant. Clearly, these rate constants are orders of magnitude larger than the τ for desensitization (a few ms; Dawe *et al.*, 2013). I suggest that the vertical compression reflects a weakening of the interaction at the D1-D1 interface at the LBD dimers, which is seen as a height reduction caused by pressure applied by the scanning tip. As the tip scans back and forth across the receptor, it applies a force to it, which eventually ruptures the interface between the two LBDs, causing the receptor to collapse to a shorter state.

It was also possible to obtain information from the fluctuations in receptor height before and after stimulation. I first compared the height distribution of the control experiments in which UV irradiation was used but no drugs were added. Data before and after mock stimulation were examined to check that the data behaved normally. Assuming that any change induced after mock stimulation should not change the control state of the receptor, it was possible to calculate the confidence level for any experiment. For example, in the control experiment shown in Fig. 3.15A, the average change after mock stimulation was 3.7%; hence, the interval level for $P<0.05$ is 7.4%, which means that any height change larger than 7.4% should be statistically different (intervals are represented as vertical red dashed lines). For all experiments, height data points were separated into two states: 'control state' (within 7.4% of the mean) and 'non-control state' (>7.4% from the mean).

Fig. 3.15B shows data from an experiment in which L-glutamate was uncaged. The black dashed line represents the interval level ($P<0.05$); hence, any point below that threshold is statistically different from the control state, and is deemed to represent a non-control state. It is obvious from the figure that the receptor spends the majority of the time in the non-control state after activation. From these graphs, it is possible to calculate the number of events and dwell times for both control and non-control states. Note that in the figure, the trace corresponding to the period before treatment is shown to illustrate of how the receptor behaves, but all of the following analysis is done with the traces for the period after treatment. Fig. 3.15C shows data from an experiment where L-glutamate was uncaged in the presence of CNQX. It is clear that there are now only a small number of events in the non-control state compared to result with L-glutamate alone.

By analysing the data for all particles under the different conditions, histograms of dwell-time events can be generated. Fig. 3.15D represents the data for L-glutamate application to wild type receptors; data for control and non-control states behave exponentially. By fitting the data with an expression for simple exponential decay, a time constant (and rate constant), as well as the total time the receptor spent in each state, can be obtained for each condition (Table 1).

The wild type receptor spends more time in the non-control state than in the control state after activation, and this situation is reversed when antagonist is present. For the D776K mutant, the time spent in each state is similar to that observed in the presence

of antagonist. By contrast, the L783C mutant behaves in a similar way to the wild type receptor in response to L-glutamate. Considering two states for the receptor, it is possible to use a thermodynamic approach to the switching between the two states (Ruan *et al.*, 2017). The free-energy changes upon transitions between distinct conformational states $\Delta G_{transition}$ is calculated from measured dwell times (τ) of the control and non-control states according to the equation:

$$\Delta G_{transition} = -ln(\tau_{non\text{-}control}/\tau_{control})\cdot k_B T,$$

where k_B is the Boltzmann constant and T is the absolute temperature.

With agonist, there is a negative ΔG for the transition from the closed to the desensitized state, which means that this transition is spontaneous. In contrast, the antagonist effect triggered a non-spontaneous transition (positive ΔG), which is more evident with the D776K mutant. For the L783C mutant, the distribution of times spent in each of the two states is similar to that for wild type receptor plus L-glutamate, but the energy barrier is still positive (although closer to zero compared to the data for the D776K mutant and the wild type receptor plus CNQX).

In a theoretical paper, Yonkunas and Kurnikova (2011) compared the energetics of the closed, active and desensitized states for an isolated LBD dimer. Their results showed that the desensitized conformation is favoured over the closed state, and that the energy difference corresponds to -0.5 kcal/mol (-9.5 kcal/mol for the desensitized state and -9.0 kcal/mol for the resting state). In our results, the experimentally determined closed-to-desensitized transition difference is -0.43 kcal/mol, very similar to the calculated value. This similarity suggests that the energetics I observed reflects the behaviour of the LBD dimer.

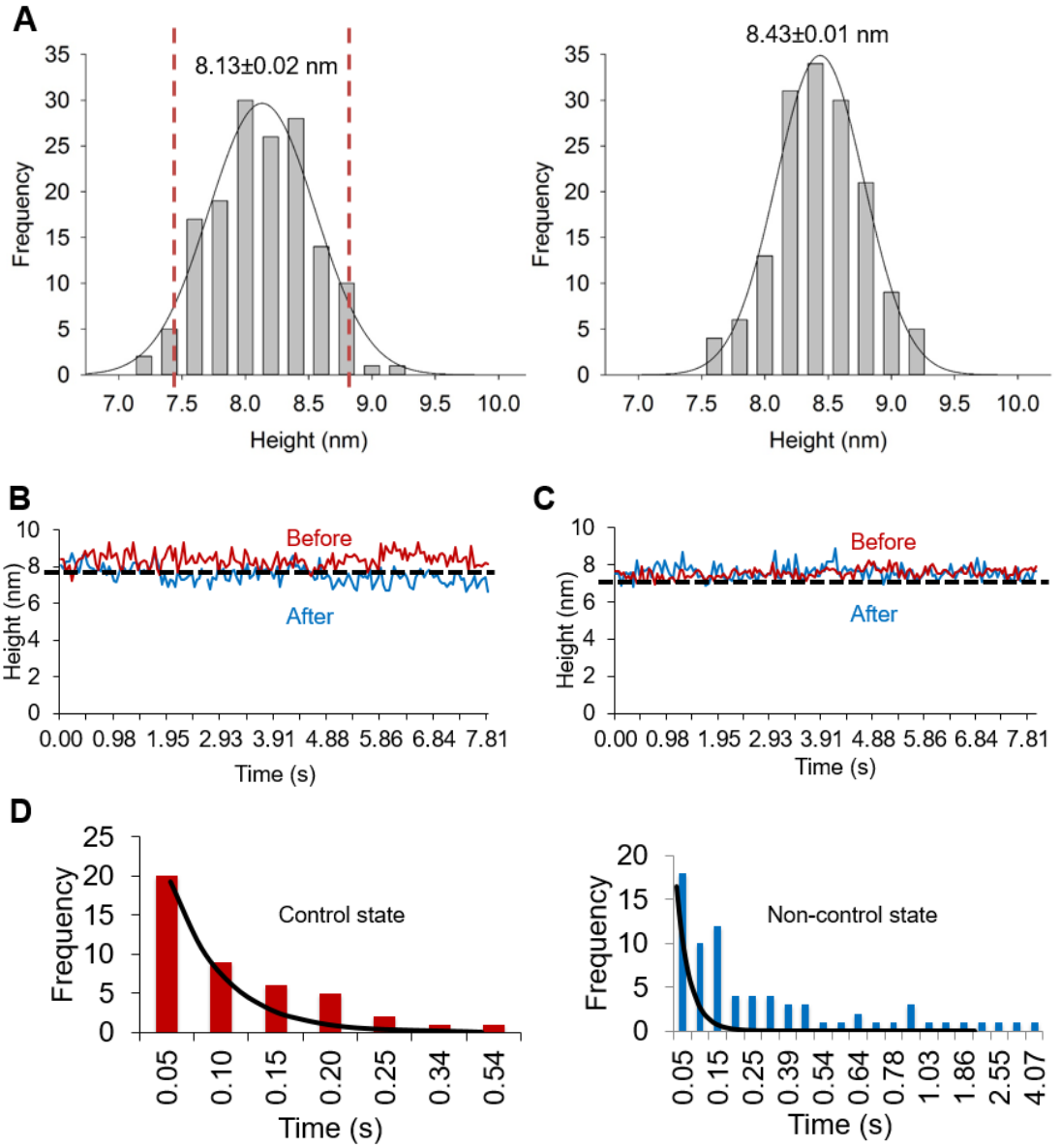

Figure 3.15. Line scanning analysis. (A) Control experiment showing the interval level as 7.4% at P<0.05. Left panel, before, and right panel, after, the start of UV photolysis. The red dashed line represents the 95% confidence level (P<0.05). (B, C) Height fluctuations showing the control and non-control states before and after uncaging of L-glutamate in the absence (B) and presence (C) of CNQX. The black dashed line represents the interval level (P<0.05). Red and blue traces show the height fluctuations before (first 8 s) and after (last 8 s) uncaging of L-glutamate, respectively. (D) Exponential curves for control and non-control states for L-glutamate application to wild type receptors.

Table 1. Line scanning analysis.

Condition	L-glutamate (WT)	L-glutamate + CNQX (WT)	L-glutamate (D776K)	L-glutamate (L783C)
Total time spent in control state (s)	5.096	36.015	32.389	7.742
Total time spent in non-control state (s)	31.85	4.459	5.39	18.228
Time constant (s) control state	0.084	0.086	0.380	0.088
Rate constant (s^{-1}) control state	11.89±1.37	11.56±1.81	2.62±0.46	11.26±1.87
Time constant (s) non-control state	0.173	0.075	0.040	0.081
Rate constant (s^{-1}) non-control state	5.75±0.81	13.25±2.56	24.57±5.18	12.20±1.90
ΔG transition from control to non-control state (Kcal/mol)	-0.43	0.08	1.32	0.04

3.2.7 Visualizing relative movement between the two ATD blobs

To follow the dynamics of the ATDs, sequential high-magnification (120 nm x 120 nm) images of receptor-containing bilayers were captured at a frequency of 1 frame/s. The target amplitude was kept at 1nm in order to exert minimum force on the receptor. Individual particles in the images were identified, and particles with heights between 6 and 8 nm were taken to represent assembled KARs. (N.B. The particles were slightly taller when using a target amplitude of 1nm instead of a conventional target amplitude of 5nm). Movement of the two blobs relative to each other was followed for the wild type receptor and the D776K mutant. Each dataset consists of two sets of images - before and after uncaging of L-glutamate by UV photolysis. The centres of the blobs were identified using Gaussian fitting (ImageJ plug-in, Adrian's FWHM; Fig. 3.16), and relative movements of the ATDs were expressed as the mean squared displacement (MSD).

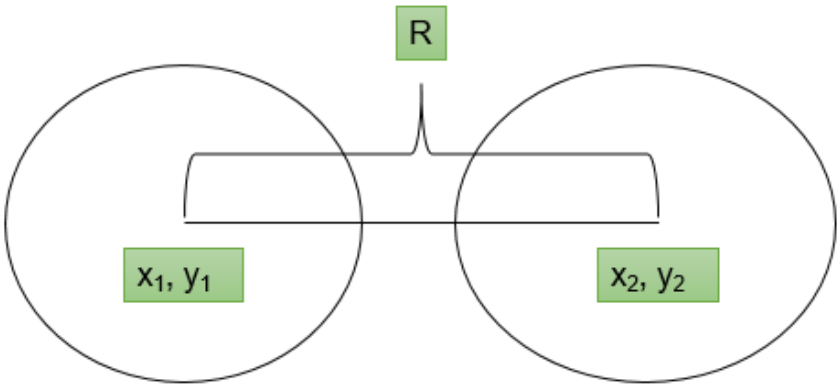

Distance between two blobs, $R_n=\sqrt{(x_2-x_1)^2 + (y_2-y_1)^2}$

Mean squared displacement, $MSD_n=(R_{(n+1)}-R_n)^2 + MSD_{(n-1)}$

(X_1, y_1) and (x_2, y_2) are the centre of mass of the blobs calculated by FWHM

Figure 3. 16. Schematic depiction of the method used to calculate MSD.

Averaged images of GluK2 ATD dimers from both wild type receptor and the D776K mutant, before and after UV photolysis of caged L-glutamate, are shown in Fig. 3.17. The centres of the two ATDs appear further apart after activation for the wild type but not the D776K mutant. Fig. 3.17B shows a montage of a single wild type GluK2 over a 40-s time-period. The variations in orientation of the receptor demonstrate the ability

of the receptor to rotate within the bilayer. As shown in Fig. 3.17C, the ATD mobility of the WT receptor increased after L-glutamate uncaging, whereas the ATD mobility of the D776K mutant was not noticeably affected.

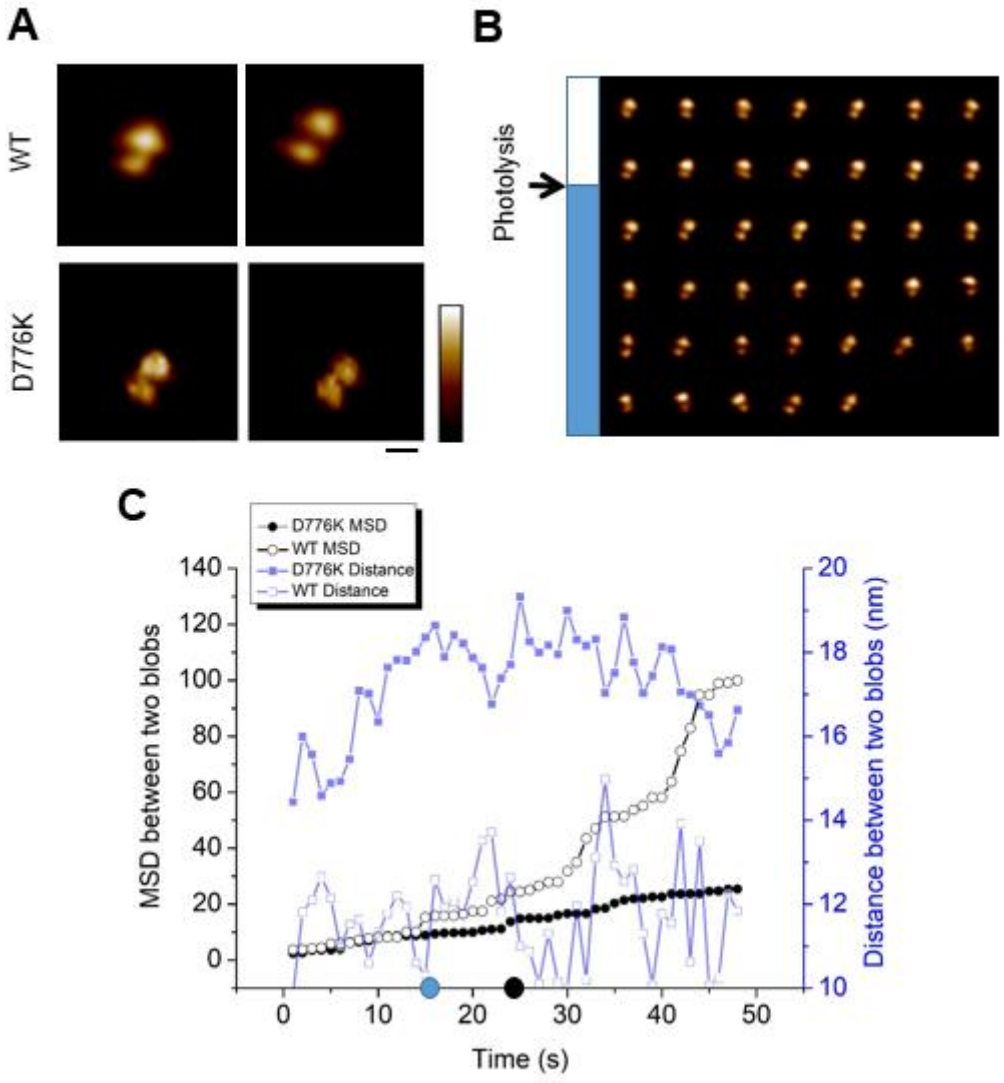

Figure 3. 17. Effect of activation on ATD mobility. (A) Averaged images of GluK2 ATD dimers from wild type and WT D776K mutant receptors, before (left panels) and after (right panels) activation. Scale bar, 20 nm; colour-height scale, -5 to 5 nm. (B) Sequential montage of wild type GluK2 in a bilayer. Images were captured at 1 frame/s; white and blue bars represent the periods before and after photolysis, respectively. (C) MSD (black) and distance between the two blobs (blue) for wild type (open symbols) and D776K mutant receptors (solid symbols). Black and blue circles on the X axis denote the time at which UV irradiation was begun for wild type and mutant receptors, respectively.

3.3 Discussion

Fast-scan AFM imaging permits the visualization of protein dynamics at the molecular level and under near-physiological conditions. For this reason, AFM stands out as perhaps the only technique currently available to provide nanometre-scale details of the structure of 'living' proteins (Ando *et al.*, 2013). The behaviour of several proteins and DNA molecules has already been analysed using AFM. Examples include studies of the structural dynamics of NMDARs (Balasuriya *et al.*, 2014; Suzuki *et al.*, 2013), GroEL (Yokokawa *et al.*, 2006), the P2X4 receptor for ATP (Shinozaki *et al.*, 2009), ASIC1a (acid-sensing ion channel 1a (Yokokawa *et al.*, 2010), the Ca^{2+}ATPase (Yokokawa *et al.*, 2011), the restriction enzyme EcoP15I (Crampton *et al.*, 2007), and nucleosomes of chromatin (Suzuki *et al.*, 2010). The current study adds the KAR to this growing list of proteins whose behaviour has been examined by fast-scan AFM.

I was able to purify the GluK2 kainate receptor to near-homogeneity (as shown by the presence of a single band on silver stains). The measured height of the extracellular region of the kainate receptor in lipid bilayers (6.6 nm) was considerably smaller than expected from the heights of the corresponding region of the NMDAR (7.2-8.3 nm) reported previously by Suzuki *et al*. (2013) and Balasuriya *et al*. (2014). Significantly, these previous experiments involved the use of different microscopes: Suzuki *et al.* (2013) used an Olympus fast-scan atomic force microscope, while Balasuriya *et al*. (2014) used a Bruker Multimode instrument. Perhaps more importantly, I also used different AFM cantilevers. Notably, the measured height of the bilayer in my experiments was 3.7 nm, which is considerably smaller than the heights recorded in the previous experiments (~4.5 nm). The measured height of the bilayer as well as that of the embedded proteins depends to some extent on the cantilever used and the optimum amplitude setpoint. This is likely to be the reason for the differences in height determined for these two closely related receptors, rather than a real difference between the receptors themselves.

According to its crystal structure, the height of the extracellular segment of intact antagonist bound AMPA receptor is 14 nm (Sobolevsky *et al.*, 2009). As in my experiments, the cryo-EM structure of GluA2 described by Nakagawa group was shorter than the crystal structure (Nakagawa *et al.*, 2005, 2006; Nakagawa, 2011). Interestingly, the Nakagawa group also reported that the ATD dimers in the EM structure were tilted in one direction, leading to asymmetry in the ATD region, with the

two dimers appearing to have two different heights, a phenomenon that I also observed by AFM imaging. By contrast, in the X-ray structure the two dimers are standing 'upright', generating a symmetric ATD structure (Nakagawa *et al.*, 2005; Sobolevsky *et al*., 2009). One possible explanation for the taller crystal structure lies in the extensive molecular engineering required to generate crystals in the first place. Mutations to the receptors for crystallization include addition of cross-linking cysteine residues, truncation of the linkers connecting the LBD and the ATD and removal of two predicted glycosylation sites (Hollmann *et al.*, 1994; Patersnack *et al.*, 2003). The necessity to introduce these mutations in order to facilitate crystallization indicates that the structure of the native receptor is very flexible, as indeed I found during my experiments. Another factor potentially contributing to the reduced height observed for the GluK2 receptor is the inevitable 'squashing' effect that the scanning tip has on the bilayer and embedded protein particles.

Unfortunately, it was not possible to detect any changes in the widths of the kainate receptor particles because of the convolution error introduced by the geometry of the scanning tip (Schneider *et al.*, 1998), which causes imaged particles to appear wider than they really are. Moreover, as a result of the presence of the bulky ATDs above the LBDs, it would in any case be difficult to obtain a precise measurement of the width of the receptor. Hence, it was not possible to draw any conclusions about whether activation results in an increase in the width of the receptor along with the observed decrease in height.

By using fast-scan AFM, I have shown that the extracellular region of the kainate receptor undergoes a rapid reduction in height in response to activation. This result is in agreement with the similar finding reported previously for the NMDAR (Suzuki *et al*., 2013; Balasuriya *et al*., 2014). This structural change can likely be attributed to the weakening of the dimer interface as the receptor enters the desensitized state (Sun *et al.*, 2002; Armstrong *et al.*, 2006), followed by a vertical compression induced by the force applied by the scanning tip.

It was possible to track the ATD mobility of the receptor by sequential AFM imaging. Two key observations emerged from my experiments. First, activation induced greater mobility of the ATDs in the wild type KAR, compared to its effect on the D776K non-desensitization mutant. This difference can be attributed to the fact that rupture of the D1 lobes in LBD of the wild type receptor (but not the D776K mutant) during

desensitization confers additional mobility on the ATDs via the ATD-LBD linker. Second, the distance between the ATDs increased after activation. This result is in agreement with the cryo-EM images of GluA2 reported by Meyerson *et al.* (2014), which also suggests the existence of more than one conformation when the receptor has been activated. I will return to the effect of receptor activation on ATD mobility in the context of the GluA2 AMPAR in Chapter 4.

The reduction in the height of the extracellular region of KARs upon activation might have significant functional implications for excitatory postsynaptic neurotransmission. The extracellular regions of iGluRs span almost half the width of the synaptic cleft (Sobolevsky *et al.*, 2009). Moreover, they are primarily localized to postsynaptic densities (PSDs), which contain other signalling proteins, cytoskeletal elements, and members of the synapse-associated protein-90 (SAP90)/PSD-95 family (Ehlers *et al.*, 1996; Kennedy, 1997; Pawson and Scott, 1997). Strikingly, native GluK2/GluK5 receptors associated with SAP90 proteins exhibit slower desensitization (Garcia et al., 1998). In addition, another integral membrane protein named NETO (neuropilin and tolloid-like), known to be an interacting partner of the KAR, modulates the function of the KAR, in the same way as the transmembrane AMPAR regulatory proteins (TARPs) do for the AMPAR, through interactions with the LBD that alter the stability of the LBD dimer interface (Copits and Swanson, 2012; Stern-Bach *et al.*, 1998; Sun *et al.*, 2002; Zhang *et al.*, 2009). Both NETO1 and NETO2 generally increase the rate of recovery of the KAR from desensitization. Moreover, NETO2 increases the probability of channel opening without affecting single-channel conductance (Zhang *et al.*, 2009). Agonist efficacy and potency are also increased when KARs incorporate NETO proteins (Straub *et al.*, 2011). Hence, it seems reasonable to speculate that a sudden reduction in the height of the extracellular region of the KAR following its activation will significantly affect the nature and strength of its relation with its synaptic partners (Fleck *et al.*, 2003; Greger *et al.*, 2006; Grunwald *et al.*, 2003; Mah *et al.*, 2005; Penn *et al.*, 2008; Priel *et al.*, 2006; Valluru *et al.*, 2005).

4. Visualization of ATD mobility in flip-flop variants

4.1 Introduction

4.1.1 Alternative splicing

Splicing is a process of editing of a pre-mRNA transcript in which the introns are cut out and the exons (the sequences that encode protein) are pasted together. For many genes, splicing produces a single protein by assembling exons in only one way; in contrast, during alternative splicing, exons are ligated in different ways, allowing a single gene to encode multiple proteins with potentially different functions, known as isoforms (Fig. 4.1; Chow *et al.,* 1977; Berget *et al.,* 1977; Black, 2003).

The splicing process is executed by a complex ribonucleoprotein mega-particle, known as the spliceosome, which is composed of small nuclear ribonucleoproteins (snRNPs) U1, U2, U4, U5 and U6, and auxiliary factors, including U2AF65 and U2AF35. It is the spliceosome that performs the two transesterification reactions that causes excision of introns and the joining together of the selected exons, which eventually results in alternative splicing (Kornblihtt *et al.,* 2013).

It is thought that greater than 95% of human multi-exon genes express multiple splice isoforms (Black, 2003; Wahl *et al.,* 2009). Alternative splicing is critical in generating genomic diversity and tissue specificity. It creates protein isoforms that have different properties and consequently differ in protein-protein interactions, subcellular localization, or catalytic ability (Stamm *et al.,* 2005). Moreover, protein products of alternative splicing contribute to the regulation of normal physiological functions, as well as a number of human pathologies. In summary, alternative splicing is involved in all cellular processes, including cell growth, differentiation and death (Chen and Manley 2009).

4.1.2 Alternative splicing and disease

Dysregulation in alternative splicing plays a vital role in numerous human diseases, including spinal muscular atrophy (SMA) and tauopathies. SMA is a recessive disease characterized by degeneration of alpha-motoneurons in the brainstem and spinal cord, which results in progressive paralysis at the spinal level; it is one of the most frequent genetic causes of infantile death. SMA is caused by the loss during alternative splicing of the SMN1 (survival of motor neurons) gene, which encodes the SMN protein

necessary for the assembly of snRNPs (Zhang *et al.*, 2008). The tau protein is encoded by a single gene called MAPT (microtubule associated protein tau). In humans, eight of the sixteen exons of this gene are alternatively spliced, and changes in the ratio of expressed isoforms can generate tauopathies (Andreadis, 2005). There are also many reports of alternative splicing linked to cancer biology, involving effects on such diverse phenomena as cell proliferation, motility, and drug responsiveness (Skotheim and Nees, 2007).

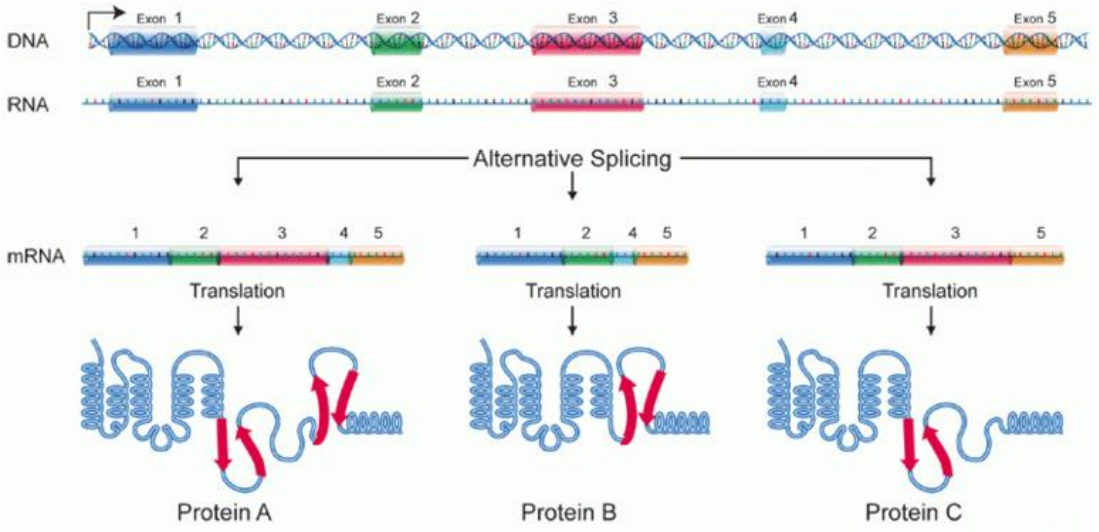

Figure 4.1. Alternative splicing. This is a process where a single gene is encoded to multiple proteins with potentially different functions (Clancy, 2008).

4.1.3 Flip and flop - alternative splicing variants of AMPA receptor

Alternative splicing in the LBD of all four AMPAR subunits generates two variants of each, known as flip and flop. Although the alternative splicing involves a 38-amino acid sequence, only nine amino acid residues, accounting for ~1% of the overall amino acid content of the protein, are actually different between flip and flop (Sommer *et al.*, 1990; Rogers *et al.*, 1991). According to the AMPAR crystal structure, the major part of the flip/flop sequence is located in the ligand binding core (Sun *et al.*, 2002; Horning and Mayer, 2004). The LBD contains the first five variable residues, but the last six residues from the flip-flop cassette are not included in the S1-S2 domain. Among these six residues, four vary between flip and flop (Figs. 4.2 and 4.3).

Alternative splicing in the AMPAR is believed to be responsible for functional heterogeneity of AMPAR-mediated synaptic transmission (Hollmann and Heinemann

1994, Jonas and Sakmann, 1992; Erreger *et al.*, 2004). At the molecular level, the flop variants of the GluA2-GluA4 AMPARs desensitize at least three times more quickly but recover more slowly from desensitization than their flip counterparts. In contrast, the GluA1 flip and flop variants exhibit identical rates of desensitization (Koike *et al.*, 2000; Quirk *et al.*, 2004; Mosbacher *et al.*, 1994). Importantly, the relative abundance of flip and flop splice variants plays a critical role in the pathogenesis of some neurodegenerative diseases; for instance, the flip:flop ratio is very high in patients with amyotrophic lateral sclerosis (ALS) (Tomiyama *et al.*, 2002). Hence, a greater understanding of the structural and functional differences between flip and flop isoforms of the AMPAR might shed new light on the aetiology of these catastrophic conditions.

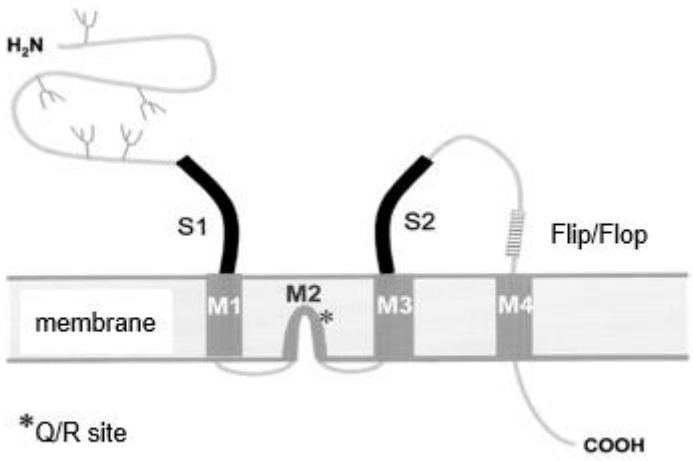

Figure 4.2. The AMPAR flip/flop site. The position of the flip/flop alternatively spliced exon is shown (Dingledine *et al.*, 1999).

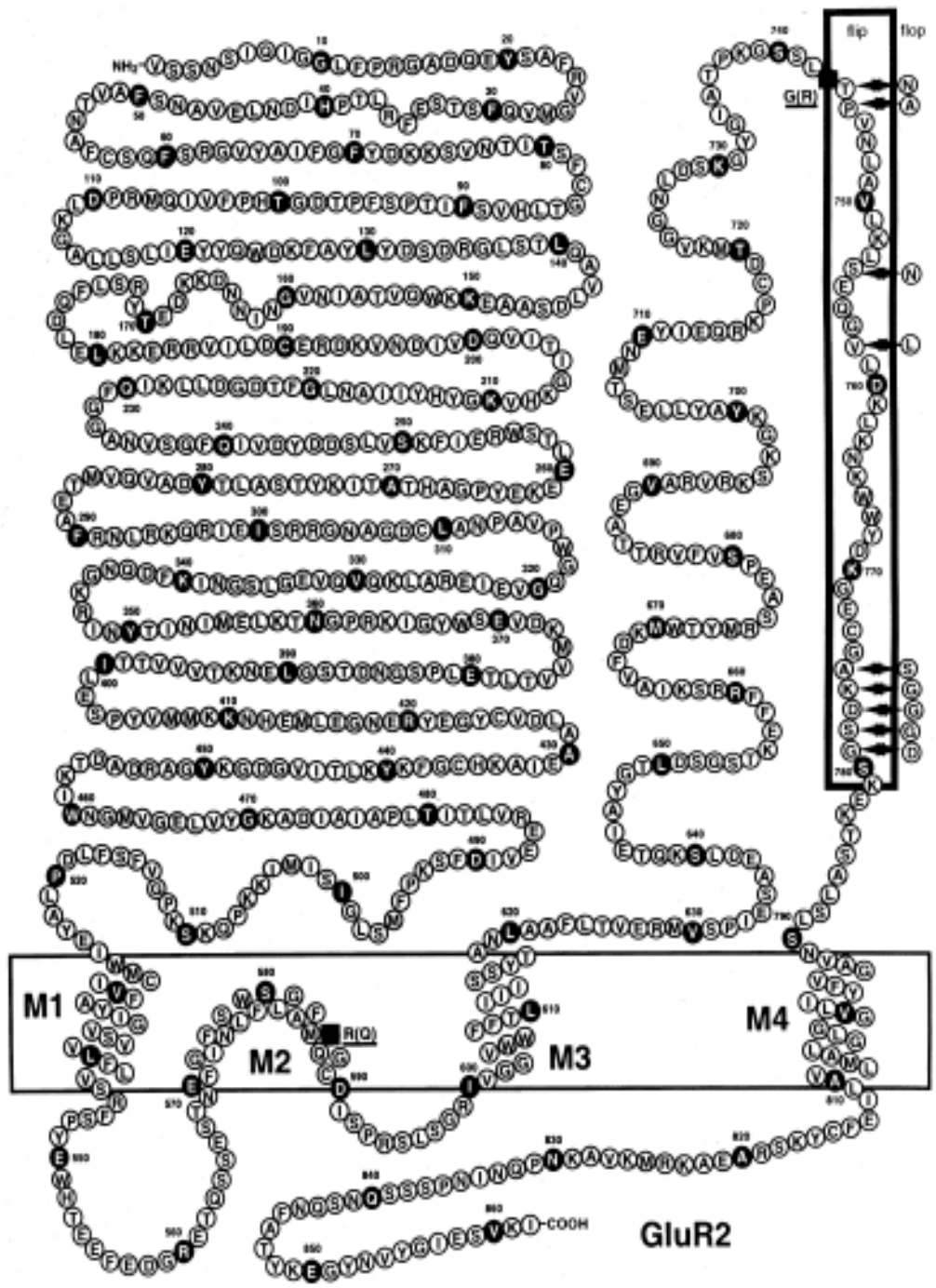

Figure 4.3. Structure of the AMPAR subunit GluA2. The 862 amino acids are shown in single-letter code. The two RNA editing sites, glutamine (Q)-to-arginine (R) at position 586 and arginine (R)-to-glycine (G) at position 743, are indicated by filled squares. The box around amino acids 744-781 indicates the region where alternative splicing variants, flip and flop, occur. The nine amino acids in flip indicated by double arrows inside the box are changed to those outside of the box in flop version; amino acid numbering does not include the signal peptide (Hollmann *et al.*, 1994).

4.1.4 Aims

In this chapter, I describe the use of fast-scan AFM imaging to study the effects of activation by L-glutamate on the mobility of the extracellular domain of the GluA2 AMPA receptor. I investigate the effects of the receptor antagonist CNQX which inhibits receptor activation, on the response to L-glutamate. Finally, I compare the mobilities of the flip and flop isoforms of the receptor, both in the unstimulated state and in response to activation.

4.2 Results

4.2.1 Immunoaffinity purification of the GluA2 AMPA receptor

tsA 201 cells were transfected separately with DNA encoding HA-tagged flip and flop isoforms of the unedited AMPAR subunit, GluA2. Transfected cells were solubilized in Triton X-100, and GluA2 was isolated by anti-HA immunoaffinity chromatography. Both the flip and flop isoforms of the isolated proteins appeared as single bands at a molecular mass of 110 kDa on silver stained gels (Fig. 4.4). Proteins were also analysed by immunoblotting using an anti-HA antibody. Single immunopositive bands, again at 110 kDa, were seen in samples of both total detergent extracts of the cells and of the eluted proteins, confirming the successful purification of both flip and flop isoforms of the GluA2 AMPA receptor.

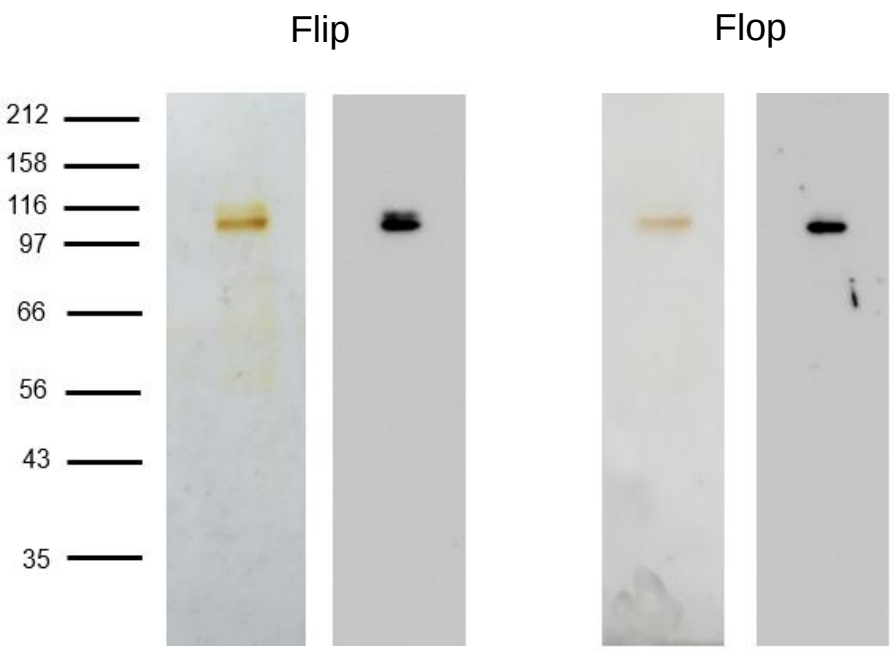

Figure 4.4. Isolation of HA-tagged flip and flop isoforms of GluA2 by anti-HA immunoaffinity chromatography. Samples were analysed by SDS-PAGE followed by either silver staining (left panels) or immunoblotting using anti-HA antibody (right panels).

4.2.2 Visualization of the GluA2 receptor integrated in lipid bilayer by AFM

Purified GluA2 (flip isoform) was integrated into supported lipid bilayers and subjected to AFM imaging. Low-magnification (2 µm x 2 µm) AFM images revealed a relatively homogenous distribution of particles (Fig. 4.5A). Since there was only one clear band on silver stains, the particles in the bilayers must all be GluA2 receptors. A frequency distribution of heights of the particles in the bilayer revealed two height populations, at 4.71±0.04 nm and 7.14±0.3 nm (Fig. 4.5B). In previous experiments on kainate receptors (Chapter 3), antibody decoration was used to identify fully assembled receptors inserted into the bilayer with their extracellular regions uppermost. Among the two height populations, only the taller one was decorated by antibodies directed against the extracellular region. It is therefore reasonable to assume that the taller peak seen with GluA2 also represents assembled receptors with their extracellular regions protruding from the bilayers.

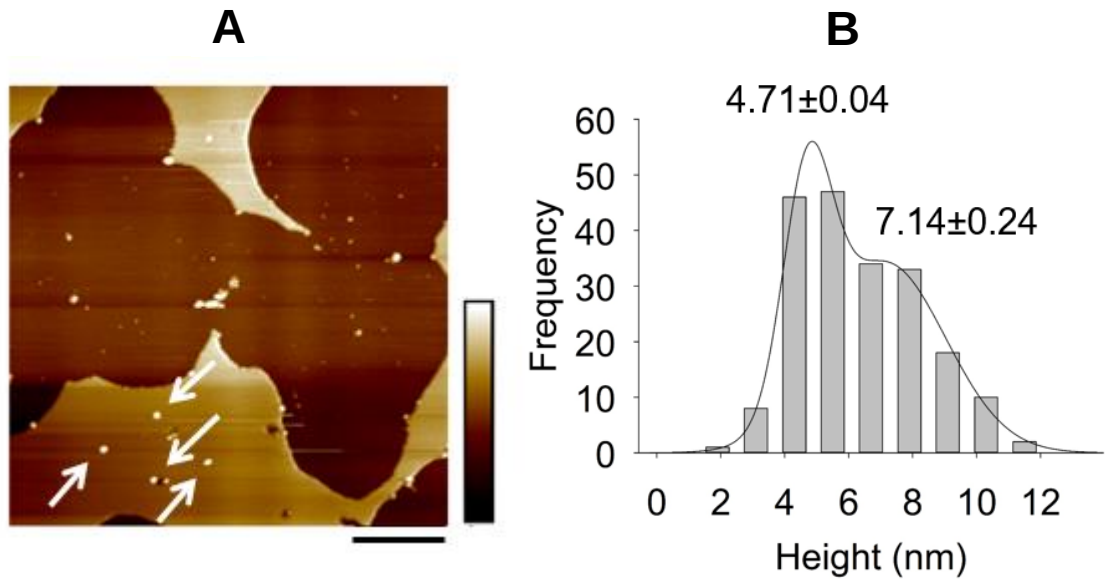

Figure 4.5. AFM imaging of bilayer-integrated GluA2. (A) Low-magnification (2 µm x 2 µm) AFM images of immunoisolated GluA2 particles. Arrows indicate assembled GluA2 receptors. Scale bar, 400 nm; colour-height scale, -5 to 5 nm. (B) Frequency distribution of heights of the GluA2 particles in bilayer. The curve indicates the fitted Gaussian functions. The peaks of the distribution (±SEM) are indicated.

In high-magnification (120 nm x 120 nm) images, the receptors appeared as double-blob structures, as was seen with KARs (Chapter 3). Based on X-ray and cryo-EM structures, each blob is likely to contain ATDs from two subunits. Galleries of zoomed AFM images of these double-blob structures, for both flip and flop isoforms, are shown in Fig. 4.6.

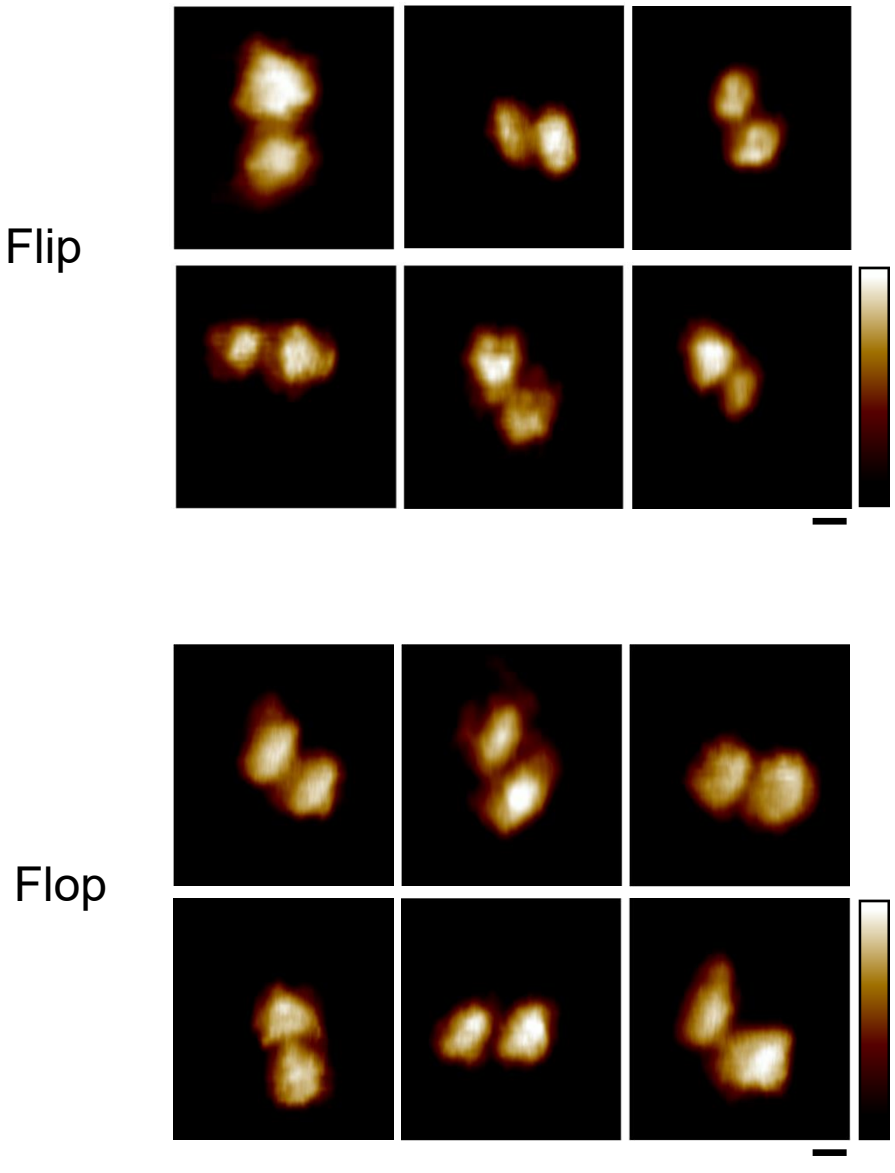

Figure 4.6. Galleries of zoomed (120 nm x 120 nm) AFM images of immunoisolated flip and flop GluA2 particles. Scale bar, 20 nm; colour-height scale, 0-8 nm.

4.2.3 Visualizing relative movement between the two ATD blobs

Sequential high-magnification (120 nm x 120 nm) images of receptor-containing bilayers were captured at a frequency of 1 frame/s. The target amplitude was kept at 1nm in order to exert minimum force on the receptor. Individual particles in the images were identified, and particles with heights between 7 and 10 nm were taken to represent assembled AMPARs. (N.B. The particles were slightly taller when using target amplitude 1nm instead of conventional target amplitude of 5nm). Movement of the two blobs relative to each other was followed under various conditions: in buffer only (control), after administration of L-glutamate at different concentrations and after L-glutamate plus antagonist (CNQX). The centres of the blobs were identified by using Gaussian fitting (ImageJ plug-in, Adrian's FWHM; Fig. 3.16), and relative movements of the ATDs were expressed as the mean squared displacement (MSD).

4.2.4 Effect of different concentrations of L-glutamate on ATD mobility

In initial experiments, three different concentrations of L-glutamate (0.1 mM, 1 mM and 10 mM) were applied to flip and flop isoforms of GluA2. The raw data are shown in Fig. 4.7A, B. By eye, it appears that for both flip and flop isoforms, the ATD mobility is greater at 10 mM L-glutamate than at the lower concentrations, and that the data are more tightly bunched for flop than for flip. When the raw data for 10 mM L-glutamate are compared to control data (i.e. buffer only), then ATD mobility seems to have been increased by activation, for both flip and flop isoforms (Fig. 4.7C, D).

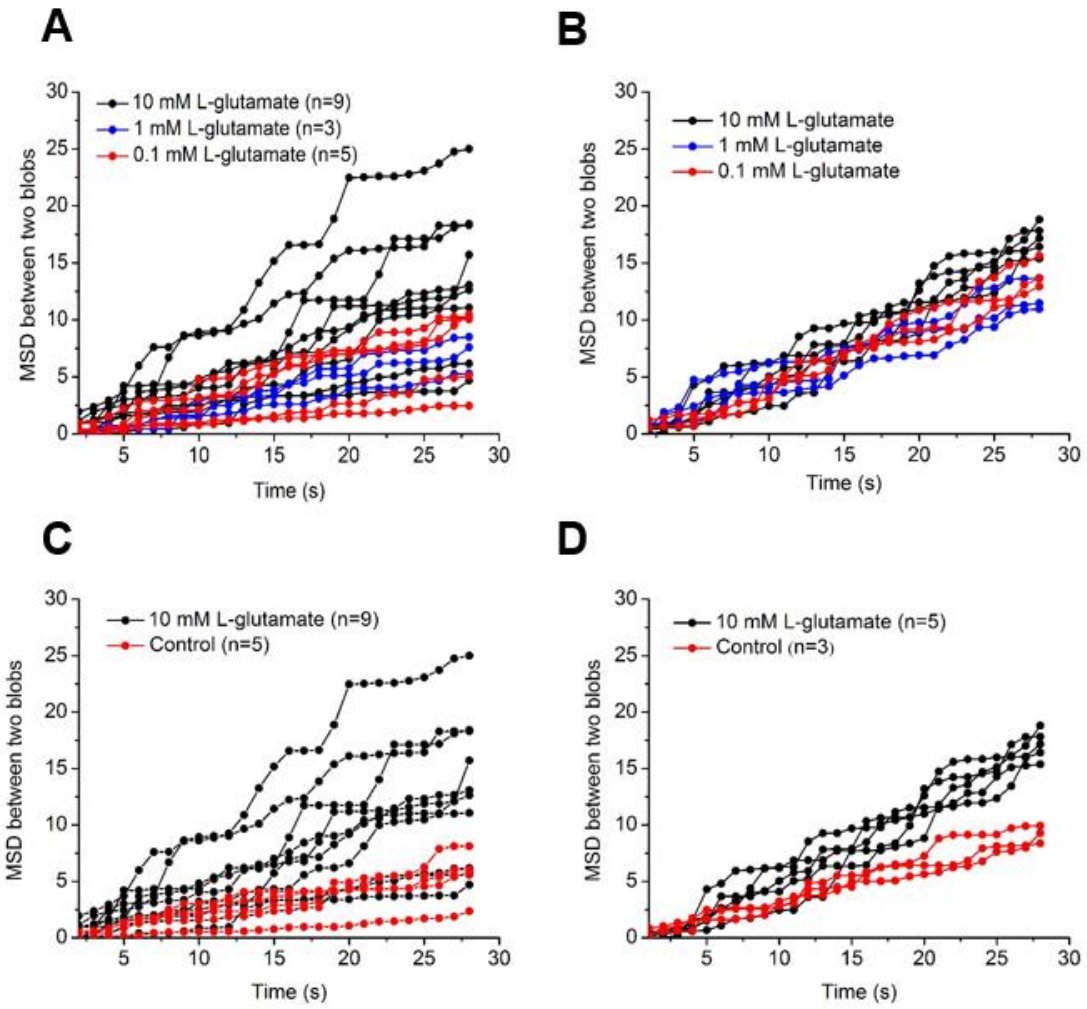

Figure 4.7. Mean squared displacement (MSD) between the two blobs. (A, B) Raw data after addition of different concentrations of L-glutamate to flip (A) and flop receptors (B). Comparison of MSD values between 10 mM L-glutamate and control for flip (C) and flop receptors (D).

Second-by-second analysis of data for groups of receptors up to 28 s confirmed that 10 mM L-glutamate caused a significant increase in ATD mobility for both flip and flop isoforms (Mann-Witney U-test; Fig. 4.8A, B). Interestingly, the flop isoform was more mobile than flip even in the absence of L-glutamate, suggesting that the former isoform has a greater inherent flexibility (Fig. 4.8C).

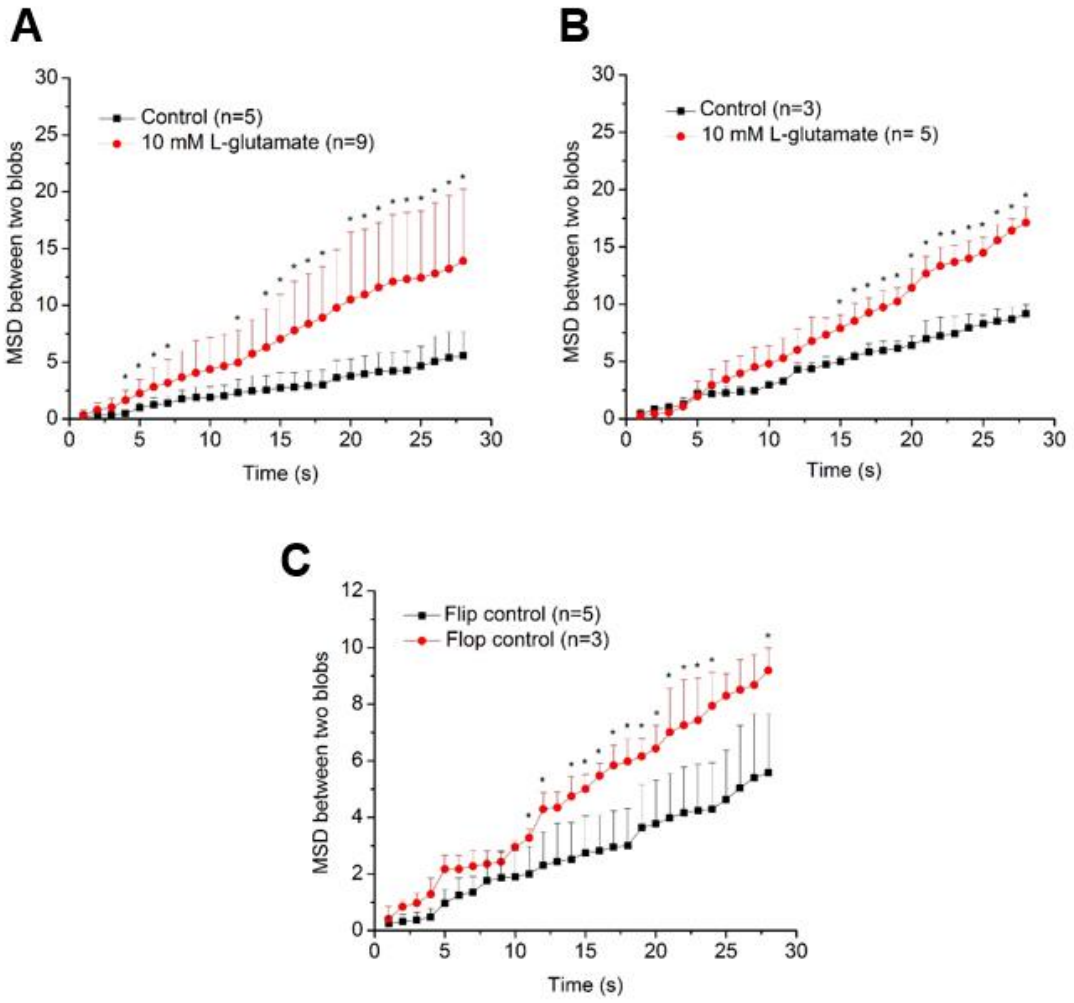

Figure 4.8. Comparison of ATD mobilities of flip and flop isoforms (1). (A, B) Combined second-by-second MSD data between 10 mM L-glutamate and control for flip (A) and flop isoforms (B). (C) MSD data for flip and flop isoforms under control conditions. Asterisks indicate a significant difference ($P<0.05$) between the pairs of values at a particular time (Mann-Witney U-test).

Comparison of the combined second-by-second data for flip and flop isoforms at two concentrations of L-glutamate, 0.1 mM and 10 mM, revealed that ATD mobility was greater for flop than flip at 0.1 mM L-glutamate (Fig. 4.10A) but not at 10 mM L-glutamate (Fig. 4.9B). Fig. 4.9C shows the combined MSD data at the 28th second for all conditions used. As can be seen, the ATD mobility of both flip and flop at 10 mM L-glutamate is greater than that of at either 0.1 mM or 1 mM L-glutamate.

4.2.5 Effect of the antagonist CNQX

CNQX is known to block the functional effects of L-glutamate on both flip and flop isoforms (Long *et al*., 1990; King *et al*., 1992). Fig. 4.10A, B show the combined second-by-second data for flip and flop isoforms, respectively, during treatment with 10 mM L-glutamate in the absence and presence of 0.5 mM CNQX. The antagonist significantly reduced the ATD mobilities of both isoforms, although there was no significant difference between the ATD mobilities of flip and flop in the presence of L-glutamate plus CNQX (Fig. 4.10C). Fig. 4.11D shows the combined MSD data at the 28^{th} second. CNQX significantly reduced the ATD mobilities of both isoforms of the receptor in the presence of L-glutamate.

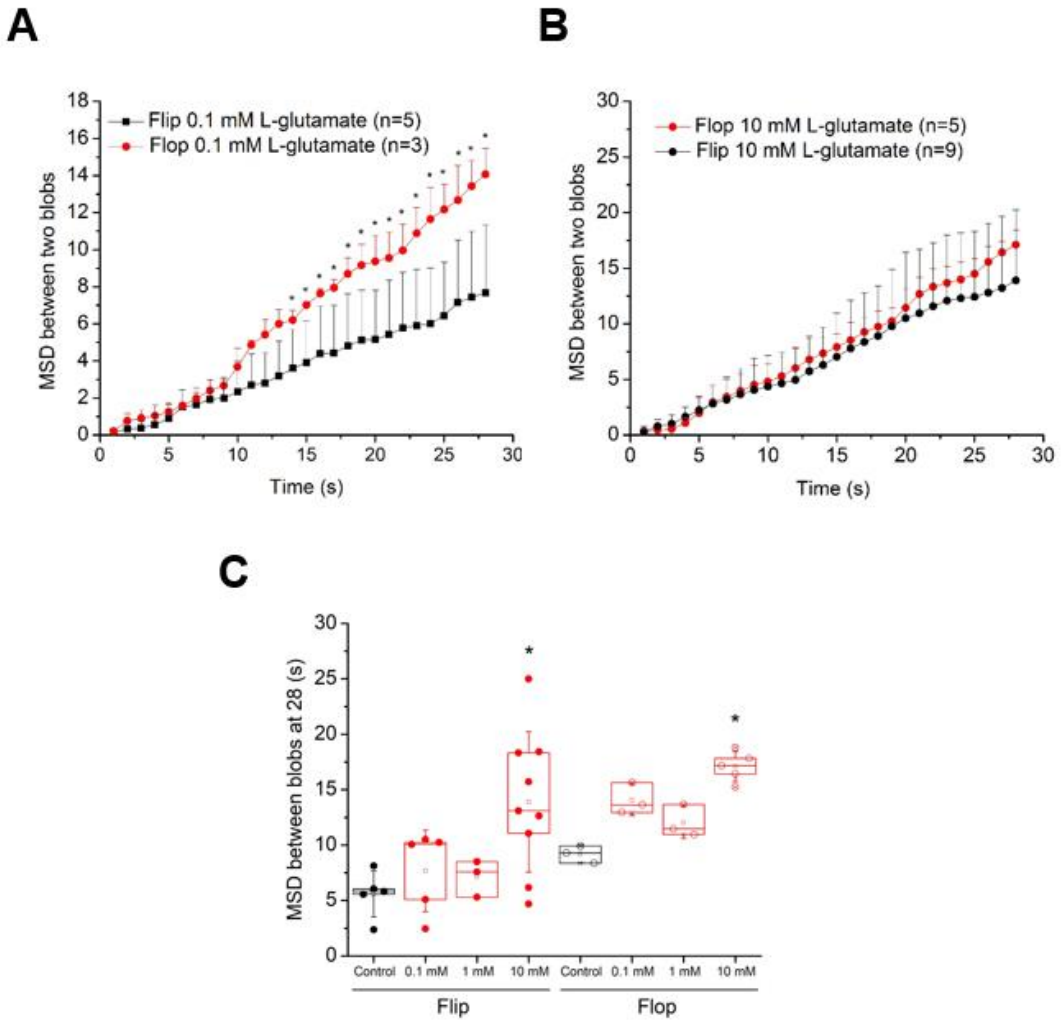

Figure 4.9. Comparison of ATD mobilities of flip and flop isoforms (2). (A, B) Second-by-second analysis (up to 28 s) of combined MSD data for flip and flop isoforms at two concentrations of L-glutamate, 0.1 mM (A), and 10 mM (B). Asterisks indicate a significant difference ($P<0.05$) between the pairs of values at a particular time (Mann-Witney U-test). (C) Box plot of MSD between the two blobs at 28 s for both flip and flop isoforms. Asterisks indicate a significant difference ($P<0.05$) between 10 mM L-glutamate and both 0.1 mM and 1 mM L-glutamate (one-way ANOVA, Fisher test).

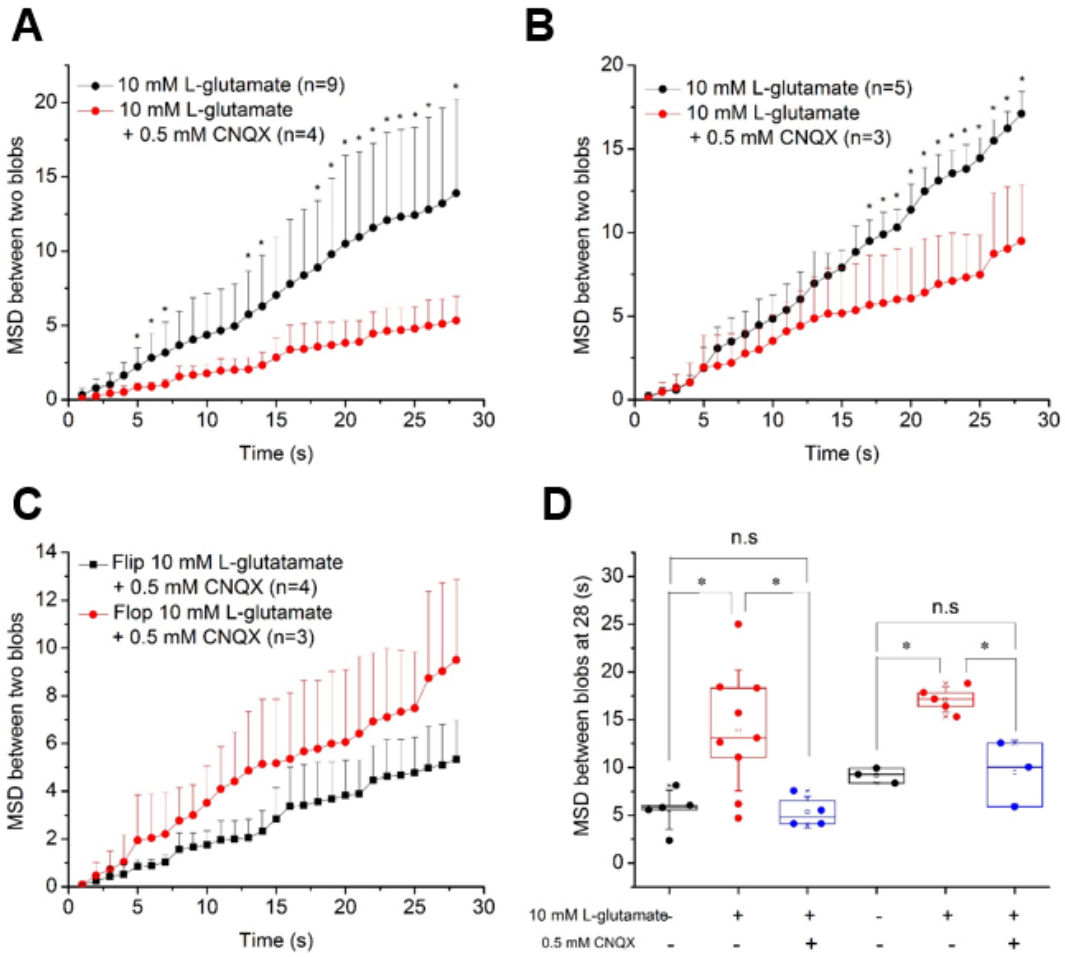

Figure 4.10. Effect of CNQX on ATD mobility. (A, B) Second-by-second analysis (up to 28 s) of combined MSD data for flip (A) and flop (B) isoforms treated with 10 mM L-glutamate in the absence and presence of 0.5 mM CNQX. Asterisks indicate a significant difference ($P<0.05$) between the pairs of values at a particular time (Mann-Witney U-test). (C) Comparison between flip and flop isoforms in 10 mM L-glutamate plus 0.5 mM CNQX. (D) Box plot of MSD between the two blobs at 28 s for both flip and flop isoforms. Asterisks indicate a significant difference ($P<0.05$) between the groups (one-way ANOVA, Fisher test).

4.3 Discussion

The series of experiments described in this chapter represent, to the best of my knowledge, the first attempt visualize the global mobility of an intact AMPA receptor. The results reveal that the receptor is highly mobile, and furthermore, that the mobility of the flop isoform of the receptor is greater than that of the flip isoform both in the unstimulated state and in response to low concentrations of L-glutamate. At high L-glutamate concentrations, the two isoforms have similar mobilities, perhaps indicating that the receptor reaches a maximum mobility under conditions of maximum activation. The ability of the receptor antagonist CNQX to restore ATD mobility of both flip and flop isoforms to control levels in the presence of L-glutamate demonstrates that receptor activation is required for the observed increase in mobility in the presence of L-glutamate alone.

AMPARs are alternatively spliced at the TM3-TM4 loop of the LBD. Quirk *et al.* (2004) identified three different regions of amino acid sequences in the GluA2 AMPAR structure that are responsible for the differences in function between flip and flop isoforms. Region 1 consists of Thr765-Pro766 in flip and Asn765-Ala766 in flop. This region is located near the N-terminal end of the flip-flop domain. Region 2 consists solely of Ser775 in flip and Asn775 in flop. This region is 10 amino acids away from the region 1. Finally, region 3 contains five residues, Ala796-Lys797-Asp798-Ser799-Gly800 in flip and Ser796-Gly797-Gly798-Gly799-Asp800 in flop. This region is located at the C-terminal end of the alternatively spliced domain. Additionally, residue 779 is Val in flip and Leu in flop (Fig. 4.11).

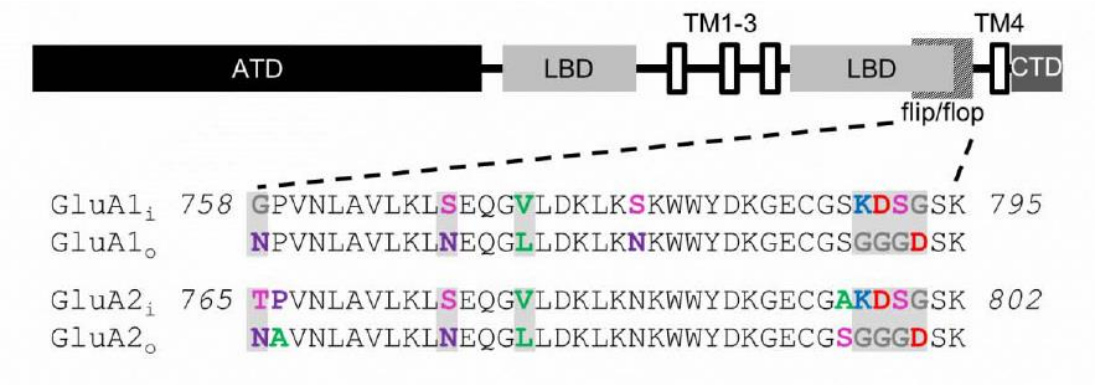

Figure 4.11. Schematic diagram showing the alternatively spliced region along with the amino acid sequence (GluA1 and GluA2). Different amino acids in this region are denoted by colour. Amino acid numbering includes the signal peptide.

Region 3 of the flop sequence is relatively rich in glycine, which is known to be a helix-breaker; this is because the lack of a side chain in glycine favours unconstrained rotation around both dihedral angles (Ramachandran *et al.,* 1963) and confers flexibility on flop. For this reason, this portion of the receptor may not have helix-forming propensities (Sutcliffe *et al.,* 1996). The free space created by the presence of the side chain-less amino acids might contribute to the greater flexibility of the flop isoform of the receptor.

It has been reported that the lower lobe of the LBD (D2) is somewhat dynamic in nature and adopts different conformations even in absence of agonist (Plested and Mayer, 2009). This mobile nature of the LBD could generate spontaneous intramolecular motions within single receptor subunits, as well as intermolecular mobility between subunits, leading to the natural mobility of the ATDs seen in the present study.

It is well known that the flop isoform of the receptor has a greater desensitization rate than flip, and that desensitization involves destabilization of the intra-dimer interface (Quirk *et al.,* 2004). The open-cleft conformation of the LBD is stabilized by the intra-domain interaction in the resting state, whereas the inter-domain interaction plays a major part in the stabilization of the conformation in the ligand-bound state (Armstrong and Gouaux, 2000; Sun *et al.,* 2002). A decline in dimer stability might therefore favour the desensitization of the receptor.

There are numerous intermolecular contacts in the crystal structure, including a salt bridge, a hydrogen bond network, and intermolecular van der Waals contacts between helices D and J in adjacent LBDs. These multiple bonding mechanisms occur in a single locus. Hence, breaking of some contacts by whatever means might not only disturb that particular interaction but could also upset the whole packing of the dimer. In agreement with this idea, it has been reported that mutations in this region could affect the stability of the dimer and in turn the rate of desensitization (Stern-Bach *et al.,* 1998; Sun *et al.,* 2002; Horning and Mayer, 2004).

The flip-flop region is located on helix J at the dimer interface (Armstrong and Gouaux, 2000; Sun *et al.,* 2002), and it has been reported that three amino acid residues in this helix, Thr/Asn765, Pro/Ala766 and Ser/Asn775 (flip/flop) (Quirk et al., 2004), are responsible for the rapid desensitization of flop. Of these residues, Asn775 is located in a site that governs the allosteric modulation of desensitization of the flip isoform by

CTZ (Partin *et al.*, 1995). It was shown by Partin *et al.* (1996) that the point mutation N775S in the flop isoform results in blockage of desensitization by CTZ. Another study confirmed the critical role of this residue, through the demonstration that the S775D mutation causes a profound increase in the desensitization rate of the flip isoform (Sun *et al.*, 2002). These results highlight the contribution of Asn775 in flop compared with Ser775 in flip as one of the reasons for the faster desensitization of flop. In fact, the role of Asn775 is to form a hydrogen bond with the backbone carbonyl of Ser750, which is located near the inter-domain hinge of the adjacent dimer (Armstrong and Gouaux, 2000; Sun *et al.*, 2002). This might affect the stability of the dimer interface via coulombic repulsion between the mutant aspartate carboxyl side chain and a main-chain carbonyl oxygen in the adjacent subunit (Horning and Mayer, 2004). Although Asn765 and Ala766 in flop do not contribute to this intermolecular interaction, they might nevertheless affect the hydrophobic bonding cluster, which in turn could impact on the stability of the inter-dimer interactions (Quirk *et al.*, 2004). It has been suggested that the faster desensitization of the flop isoform is caused by differences in amino acid sequence, which confer an increased flexibility of the receptor compared with flip. On the basis of the above discussion one could speculate that the greater mobility of the flop isoform might arise from the flexible packing of LBD dimer interface. Any changes in the arrangement in the dimer interface of the LBD upon addition of L-glutamate could directly affect the upper part of the receptor via the connected linker, which in turn might cause the rapid movement of the receptor.

The LBD layer is the 'engine' of the receptor since the source of energy for conformational changes in the receptor is generated by this domain. The flip-flop region of the AMPAR acts as a linker to TM4. A change in the conformation of the LBD upon addition of the L-glutamate is transferred to the channel pore via this linker. Since the flop domain is much more flexible than its flip counterpart, any changes in the LBD clamshell will facilitate channel activation and desensitization more in flop than in flip (Sutcliffe *et al.*, 1996). In the same way, any changes in the LBD layer will affect the mobility of the ATD layer of the receptor. Moreover, it has been reported that a truncated GluA2 receptor lacking ATDs has functional properties, such as ligand-binding affinities, agonist potencies, and kinetic properties, that are very similar to those of the wild-type receptor (Horning and Mayer, 2004; Pasternack *et al.*, 2002). It is

plausible, therefore, that LBD layer is responsible for controlling the mobility of the ATDs.

Interestingly, although the ATDs are the most membrane-distal domains, they have been reported to play important roles in signalling through the iGluRs (Cais *et al.*, 2014). In fact, channel gating is TARP-dependent and TARP contact points include the ligand binding cleft, the flip/flop region, and the LBD-ion channel linker. Hence, any torsion in ATD-LBD linker could mediate TARP-dependent changes in AMPAR gating. It is not yet known if there is any difference in binding affinity between the alternate spliced regions and TARP. It would also be very interesting to determine whether TARP can influence the mobility of the ATDs, a question that could be answered using the AFM imaging approach described here.

In fact, the single-channel conductance of the AMPAR depends to a large extent on L-glutamate concentration (Smith and Howe, 2000). In addition, it was reported that the extent of the receptor activation depends on the degree of domain closure, and that partial agonists have less effect on the conformation of the domain cleft than full agonists (Armstrong and Gouaux, 2000). These properties might be attributed to the fact that higher concentrations of agonist disguise the difference in mobility of the ATDs between the two splice variants.

5. Allosteric modulation of AMPARs by anions

5.1 Introduction

5.1.1 Allosteric modification

The binding site on a receptor to which the neurotransmitter binds is called the orthosteric binding site, while other sites to which ligands bind are known as allosteric binding sites. Often, a receptor will have several allosteric binding sites that are specific for different ligands. Ligands causing allosteric modulation are of two types: positive allosteric modulators, which enhance the agonist-induced response, and negative allosteric modulators, which reduce receptor function. Interestingly, although they bind remotely, allosteric ligands can contribute to the conformational rearrangements of the receptor associated with channel gating (Partin *et al.,* 1996; Bertolino *et al*., 1993; Yamada and Tang 1993).

Negative allosteric modulators acting on ionotropic receptors include ifenprodil, a modulator of NMDARs, which can be useful in treating cerebrovascular injuries (Başkaya *et al.,* 1997). Another example is perampanel, which acts as a negative modulator of AMPARs and is used to treat some forms of epilepsy and amyotrophic lateral sclerosis (ALS; Zaccara *et al.,* 2013; Chong and Lerman, 2016; Akamatsu *et al.,* 2016). Positive allosteric modulators, include galantamine, an effector of the nicotinic acetylcholine receptor, which is reported to be effective in the treatment of neurodegenerative cholinergic disorders such as Alzheimer's disease (Loy and Schneider, 2006). In addition, LY404187, as allosteric effector of the AMPAR, has been proposed for the treatment of Parkinson's disease (O'Neil *et al.,* 2004).

Allosteric sites offer the possibility of numerous ligand-receptor interactions and signaling phenomena in addition to those involving the orthosteric site, and are believed to have a bright future in drug discovery (Hogg *et al.,* 2005). Allosteric effectors offer significant advantages over the corresponding orthosteric ligands or open channel inhibitors in terms of selectivity, including subtype selectivity within receptor families. By contrast, orthosteric ligands are often characterized by poor selectivity and reduced efficacy, which in turn results in cytotoxicity and down-regulation of the receptor, respectively (Christopoulos, 2002; Conn *et al*., 2009; Kenakin and Miller, 2010). Moreover, allosteric modulators often show ceiling effects after the sites are occupied, which gives a larger safety window for drug administration. Another failing of

orthosteric sites is that they allow prolonged activation of the receptor with an agonist, or complete inhibition of gating when competitive antagonists are used at saturating concentrations (Hogg *et al.*, 2005; Jin *et al.*, 2005).

5.1.2 Allosteric modulators of ionotropic glutamate receptors

Two distinct allosteric binding sites have so far been reported in the AMPAR, namely the cyclothiazide (CTZ) and the 2, 3-benzodiazepine sites (Hogg *et al.*, 2005). CTZ binding sites are located at the dimer interface and at the inter-domain hinge (Fig. 5.1A; Partin *et al.*, 1996; Lawrence *et al.*, 2003). Along with CTZ, aniracetam and CX614 are well characterized examples of allosteric modulators of the AMPAR acting at this site. Two CTZ molecules bind in the dimer interface, whereas aniracetam and CX614 share a single binding site. In addition, whereas the long axis of the CTZ molecule spans the dimer interface, in the case of aniracetam and CX614 the binding site is centred on the molecular two-fold axis (Fig. 5.2A, B; Jin *et al.*, 2005). By binding at the dimer interface, these molecules promote stabilization of the closed-cleft, agonist-bound conformation of the ligand-binding core and therefore slow ion channel desensitization and deactivation (Partin *et al.*, 1996; Sun *et al.*, 2002). CTZ acts as a desensitization blocker which is effective on the flip but not the flop isoform (Sun *et al.*, 2002). In contrast, aniracetam and CX614 slow channel deactivation and are more efficacious on flop than on flip (Jin *et al.*, 2005; Quirk and Nisenbaum, 2003). Another group of AMPAR modulators belong to 2, 3-benzodiazepine family (e.g. GYKI-52466). They have a unique binding site at the interface between the S1 and S2 L-glutamate binding core and the channel transmembrane domains. By binding with the S1-M1 and S2-M4 linkers, they prevent the agonist-occupied LBDs from inducing sufficient conformational change to open the channel pore (Balannik *et al.*, 2005). Hence, binding of a modulator at any position could potentially influence the stability of the protein complex and eventually result in conformational changes.

An interesting feature of NMDARs is their susceptibility to allosteric regulation through the binding of small molecules at the interface between the ATDs (Yuan *et al.*, 2009; Gielen *et al.*, 2009). For instance, ifenprodil, a negative allosteric modulator of the NMDAR, binds at the interface between the ATDs of GluN1/GluN2B heterodimers (Karakas *et al.*, 2011). By contrast, polyamine compounds such as spermidine and spermine have three distinct binding sites on NMDARs. Glycine-independent stimulation occurs through interaction with the ATDs of GluN1/GluN2B

receptors, whereas glycine-dependent stimulation and voltage-dependent inhibition are seen at both GluN1/GluN2A and GluN1/GluN2B receptors (Monaghan and Jane, 2009; Williams, 2009). Another important modulator at the level of the ATD is Zn^{2+}, which has a distinct binding site in the GluN2A-ATD cleft. Although Zn^{2+} targets both GluN1/GluN2A and GluN1/GluN2B receptors, it shows a higher affinity for GluN2A-containing than for GluN2B-containing receptors (Fig. 5.1B; Karakas *et al.*, 2011; Rachline *et al.*, 2005).

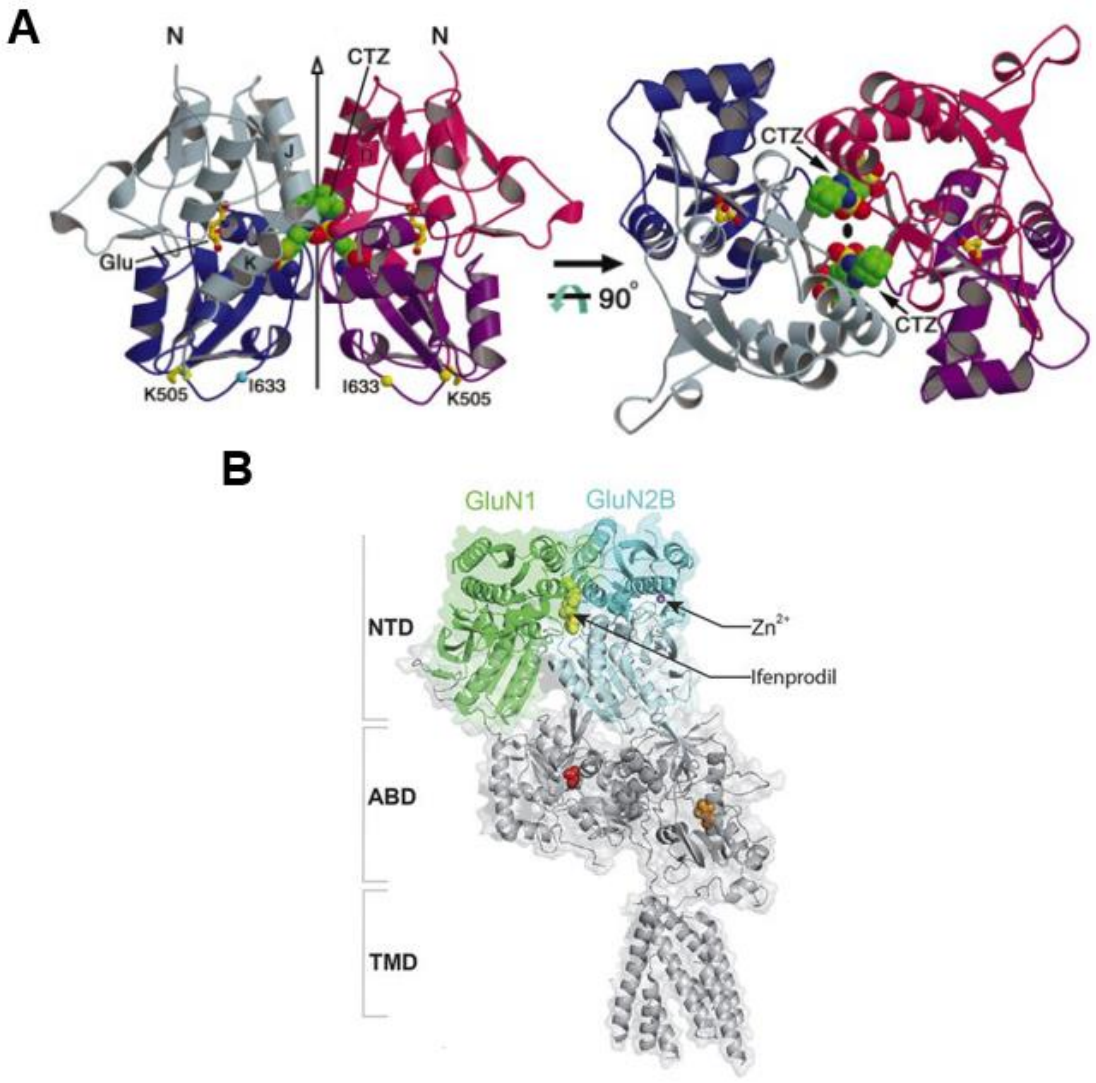

Figure 5.1. CTZ acts as a positive allosteric modulator of the AMPAR. (A) Left panel: Side view of the crystal structure of the LBD of the GluA2 N775S dimer in a complex with glutamate and CTZ. Right panel: Top view of the dimer, looking down the 2-fold axis. The two CTZ molecules are represented in green (Sun *et al.*, 2002). (B) Side view of the crystal structure of a GluN1/GluN2B heterodimer. Binding pockets of two allosteric inhibitors, ifenprodil and Zn^2, are indicated. Ifenprodil (yellow sphere) sits at the interface of two subunits, whereas Zn^{2+} (grey sphere) binds at the GluN2B ATD cleft. Co-agonists glycine (red) and glutamate (orange) are represented as spheres (Tian and Ye, 2016).

5.1.3 Allosteric modulation of ionotropic receptor desensitization and deactivation

Receptor desensitization and deactivation are distinct processes. Deactivation is characterized by the closing of the ion conducting pore of the receptor caused by the dissociation of the agonist from the ligand-binding core. By contrast, desensitization is a comparatively long-lasting, agonist-bound, non-conducting state. Desensitization largely depends on the destabilization of the dimer interface, while deactivation is related to the stability of the closed clamshell state of the ligand-binding core. Interestingly, AMPAR allosteric modulators can influence both deactivation (e.g. aniracetam and CX614) and desensitization (e.g. CTZ). This dual action could be attributable to the fact that the allosteric binding sites governing these two phenomena partially overlap in the AMPAR (Jin *et al.*, 2005).

5.1.4 Ions as modulators

It has been known for some time that ion channel gating is influenced by the external ionic conditions around the cell. For instance, Ascher *et al*. (1978) observed that the stability of the open state of the nicotinic acetylcholine receptor largely depends on the concentration of the permeant ions. In the case of voltage-gated K^+ channels, crystallographic analysis confirmed the effect of permeant ions on the gating of the ion channel (Zhou *et al.,* 2001). Bowie (2002) found that modulation of KARs is also strongly sensitive to anions. Although there are many examples of regulation of the gating machinery by ions, the molecular mechanisms underlying conformational changes in the receptor as a result of ionic modulation are usually poorly understood.

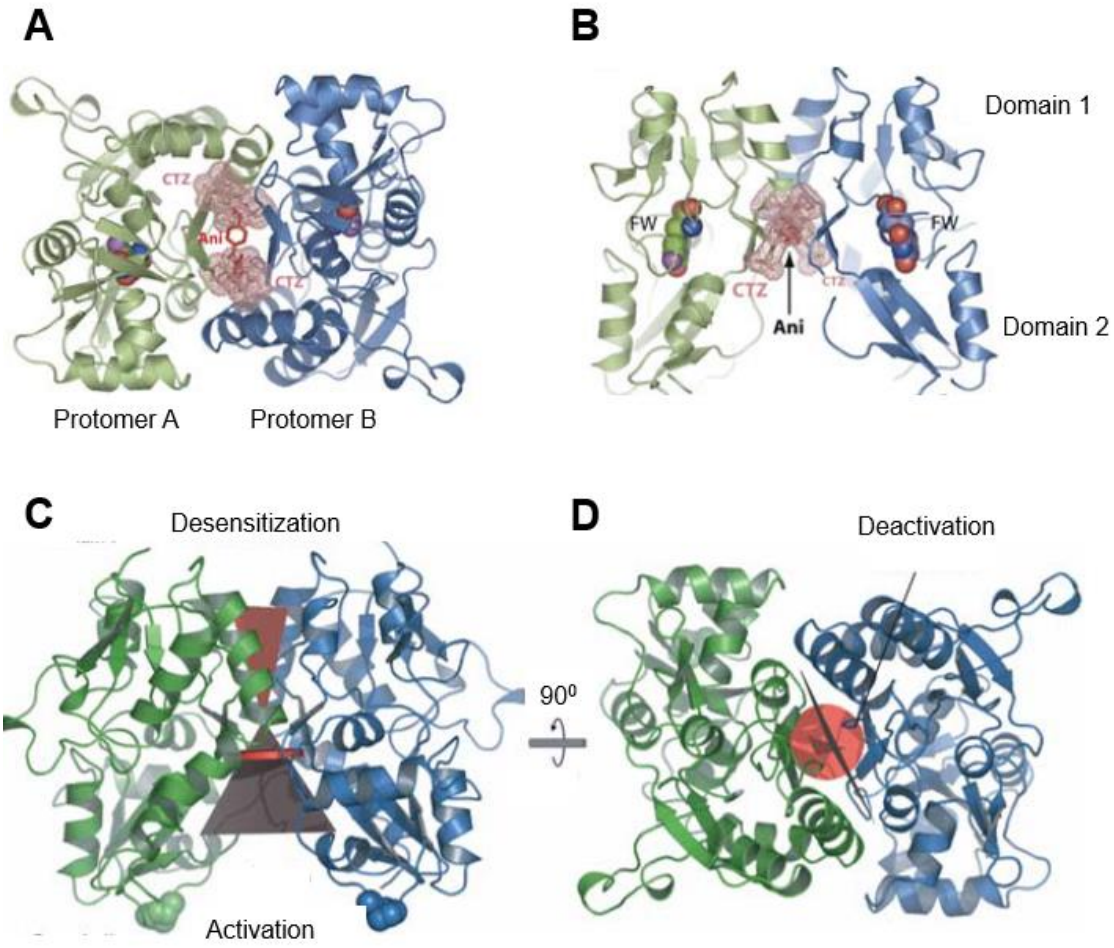

Figure 5.2. Comparison of the binding sites for aniracetam and CTZ. (A) View down the twofold axis of the aniracetam/fluorowillardiine (Ani/FW) complex along with two CTZ molecules superimposed on the structure; aniracetam is in red and CTZ molecules are pink. (B) View perpendicular to the molecular two-fold axis. (C) Modulator binding sites in relation to their modes of action. Receptor activation results in an increase in the distance between domains 2 of each subunit (dark grey triangle). Following activation, rearrangements of domain 1 interactions (red triangle) cause channel desensitization; this rearrangement is prevented by the binding of CTZ in the dimer interface. CX614 binds at the hinges between domains 1 and 2 (red circle). (D) Rotating the view by 90° of (C) allows a view of the CX614 interaction with the hinges, which results in slowing of deactivation by stabilizing the closed-clamshell conformation (Jin *et al.*, 2005).

5.1.5 Aims

In this chapter, I describe attempts to use AFM imaging to look for evidence of global conformational changes in the AMPAR in response to anion substitutions. Specifically, I assess whether anions are able to produce vertical compression in the extracellular domain of the receptor through an allosteric effect in the absence of the orthosteric ligand, L-glutamate. I also attempt to identify the site of action of the anions on the receptor. Finally, since the LBD is the site of flip-flop alternative splicing of the AMPAR, I asked whether any anion effects on receptor conformation are isoform-dependent.

5.2 Results

5.2.1 Functional evidence for an effect of anions on the AMPA receptor

The stimulus to look for structural effects of different anions on the AMPAR was a series of electrophysiological experiments carried out by our collaborators in the group of Dr. Derek Bowie, Department of Pharmacology and Therapeutics, McGill University. According to their recordings on outside-out membrane patches containing GluA2 AMPARs, there is a relationship between the radius of the halide ion in the bathing solution and the rate of desensitization of the receptor. Specifically, larger halide ions resulted in faster desensitization of the flip isoform of GluA2. By contrast, the deactivation time constant (~0.5 ms) did not show significant changes among the halide species. Further, the flop isoform of the receptor exhibited less sensitivity to anion substitution than flip (Fig. 5.3A-C).

Crystal structures of the GluA2 (flop)-LBD and the flip-like mutant GluA2 (flop)-LBD N775S in the presence of bromide, at 1.8 Å resolution, were obtained by collaborators in the group of Dr. Jette Kastrup, Department of Drug Design and Pharmacology, University of Copenhagen. These structures positioned a pair of bromide ions near the lower base of the D1-D1 dimer interface (Fig. 5.3D), and close to residue 775, which is particularly important in conferring the faster desensitization rate on the flop isoform. The observation that the GluA2 (flip)-S775N point mutant behaved like the flop isoform in terms of anion sensitivity indicates that residue 775 is intimately involved in modulation of the receptor by anions. By contrast, mutation of the two other residues responsible for faster desensitization in flop (T765N and P766A) did not remove anion sensitivity (Fig. 5.3C).

Based upon this information about anion modulation of desensitization of GluA2 (flip), I used AFM imaging to test whether anion substitution caused any global conformational changes that might be related to the observed differences in channel gating.

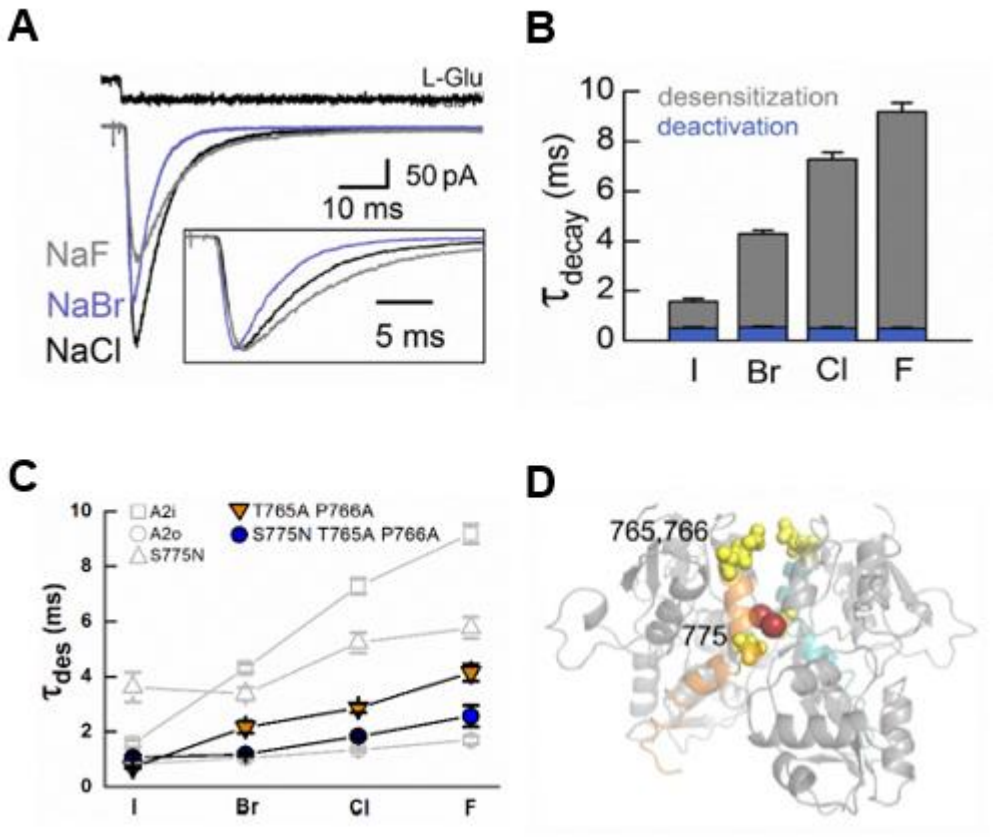

Figure 5.3. Functional effects of anions on GluA2. (A) Typical current responses of wild-type GluA2 (flip) receptors to a 250-ms application of 10 mM L-glutamate in the presence of external NaCl (black), NaBr (light blue), and NaF (grey). In the inset, the responses are scaled to the same peak amplitude. The uppermost trace (black) shows the junction current, recorded with an open patch pipette after the experiment to monitor the profile of solution exchange. (B) Mean time constants (τ_{deac} and τ_{des}) of current decay after a 250-ms application of 10 mM L-glutamate onto GluA2 (flip) in the presence of different external anions. Data are mean±SEM. (C) Mean desensitization time constants (τ_{des}) after a 250-ms application of 10 mM L-glutamate onto flip/flop isoforms (A2i/A2o) and various mutants in the presence of different external anions. Data are mean±SEM. (D) Side view of the GluA2 (flop)-LBD N775S dimer (RbBr form), indicating three important positions responsible for the rapid desensitization of the flop isoform. Bromide ions are shown as red spheres. Data (unpublished) are from the labs of Dr. Derek Bowie (A-C) and Dr. Jette Kastrup (D).

5.2.2 AFM imaging of GluA2 (flip) integrated into a lipid bilayer

The flip splice variant of HA-GluA2 was isolated from a detergent extract of transfected tsA 201 cells by anti-HA immunoaffinity chromatography, and the purity of the sample was checked by SDS-PAGE followed by silver staining and immunoblotting, as described in Chapter 4. Isolated GluA2 was integrated into liposomes (PC/PS, 3:1), and the proteoliposomes were deposited onto a mica surface to produce a supported proteolipid bilayer. An AFM image of a plain (protein-free) lipid bilayer was smooth and featureless; in contrast, a bilayer containing integrated GluA2 receptors had many protruding particles (Fig. 5.4).

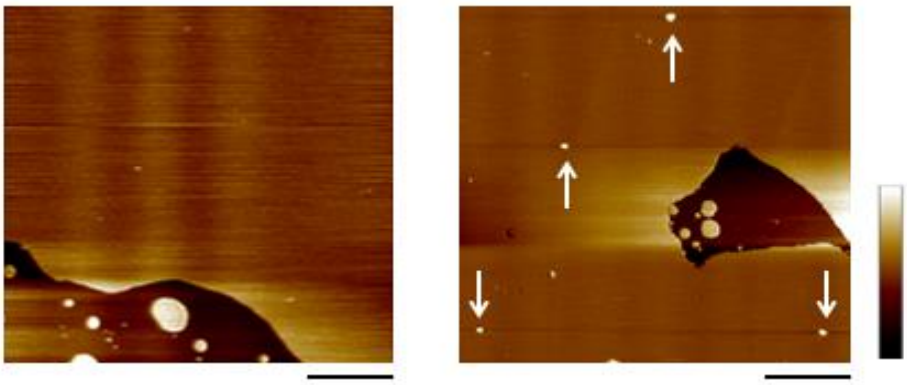

Figure 5.4. AFM imaging of bilayer-integrated GluA2. AFM images of a protein-free bilayer (left) and a bilayer containing integrated GluA2 (right). Arrows indicate GluA2 receptors. Scale bar, 400 nm; colour-height scale, -5 to 5 nm.

5.2.3 Effect of anion substitution and addition of L-glutamate on GluA2 (flip) height

When the solution in the imaging chamber was changed from NaCl to either NaBr or NaI, GluA2 receptors exhibited a height reduction of 0.74±0.06 nm (n=12) and 0.87±0.11 nm (n=13), respectively (Fig. 5.5). When L-glutamate (10 mM) was added to the receptors in either NaBr or NaI, there were further smaller height reductions, of 0.25±0.05 nm (n=14) and 0.18±0.06 nm (n=12), respectively. In contrast, the addition of L-glutamate in NaCl caused a much greater reduction in receptor height (0.69±0.11 nm; n=11). This result might be attributable to the fact that extracellular domain of the receptor had already become compressed upon addition of NaBr or NaI, which reduced the scope for further compression in response to L-glutamate (Fig. 5.6).

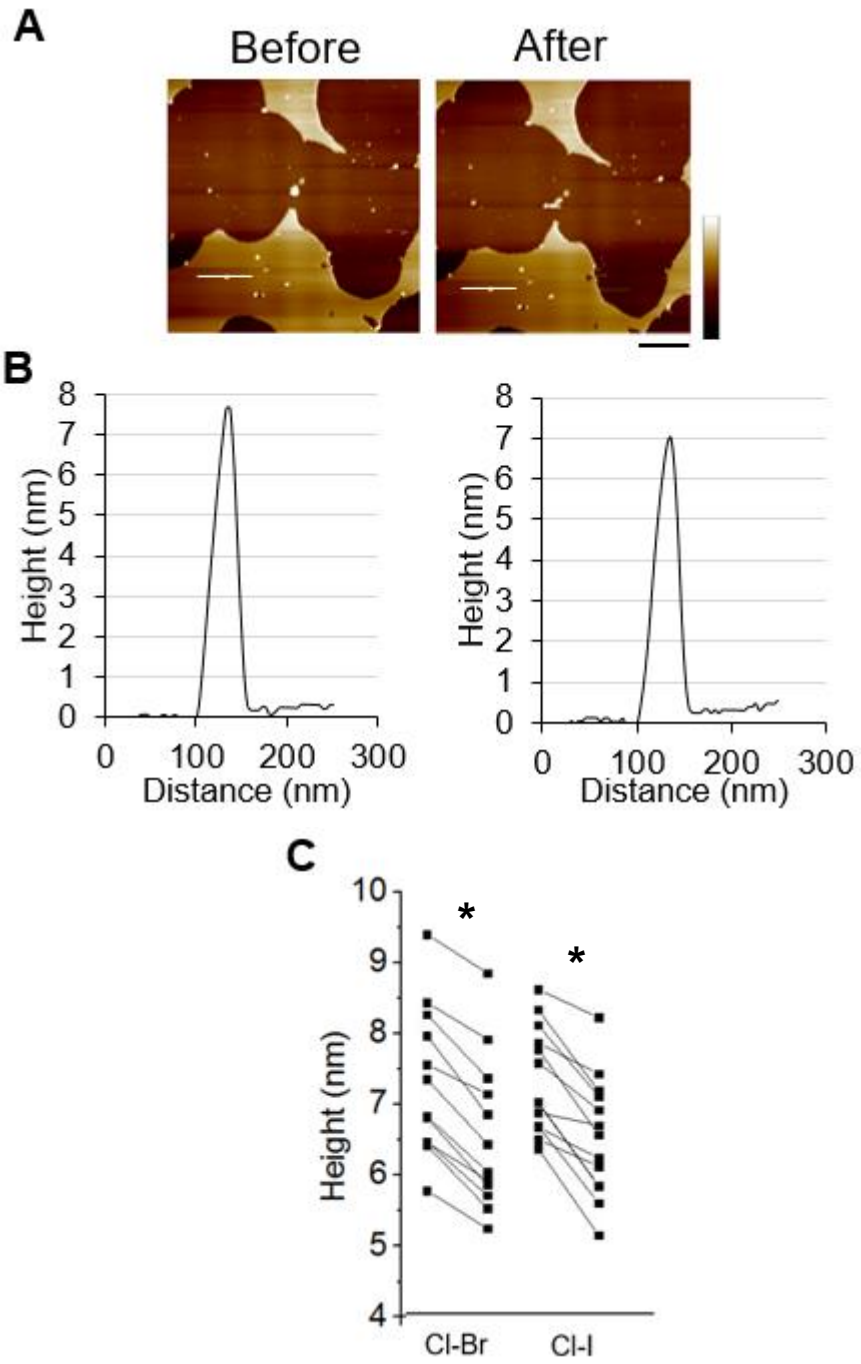

Figure 5.5. Effect of anion substitution on GluA2 (flip) height. (A) Representative AFM images of a bilayer containing GluA2 receptors in NaCl (150 mM; left) and after switching to NaI (150 mM; right). Scale bar, 400 nm; colour-height scale, -5 to 5 nm. (B) Sections through the receptor at the position indicated by the line in (A). Peak heights are 7.67 nm before and 7.01 nm after anion substitution. (C) Height data for individual receptors before and after Cl-Br and Cl-I substitutions. Asterisks indicate a significant difference ($P<0.01$, Student's paired two-tailed *t*-test).

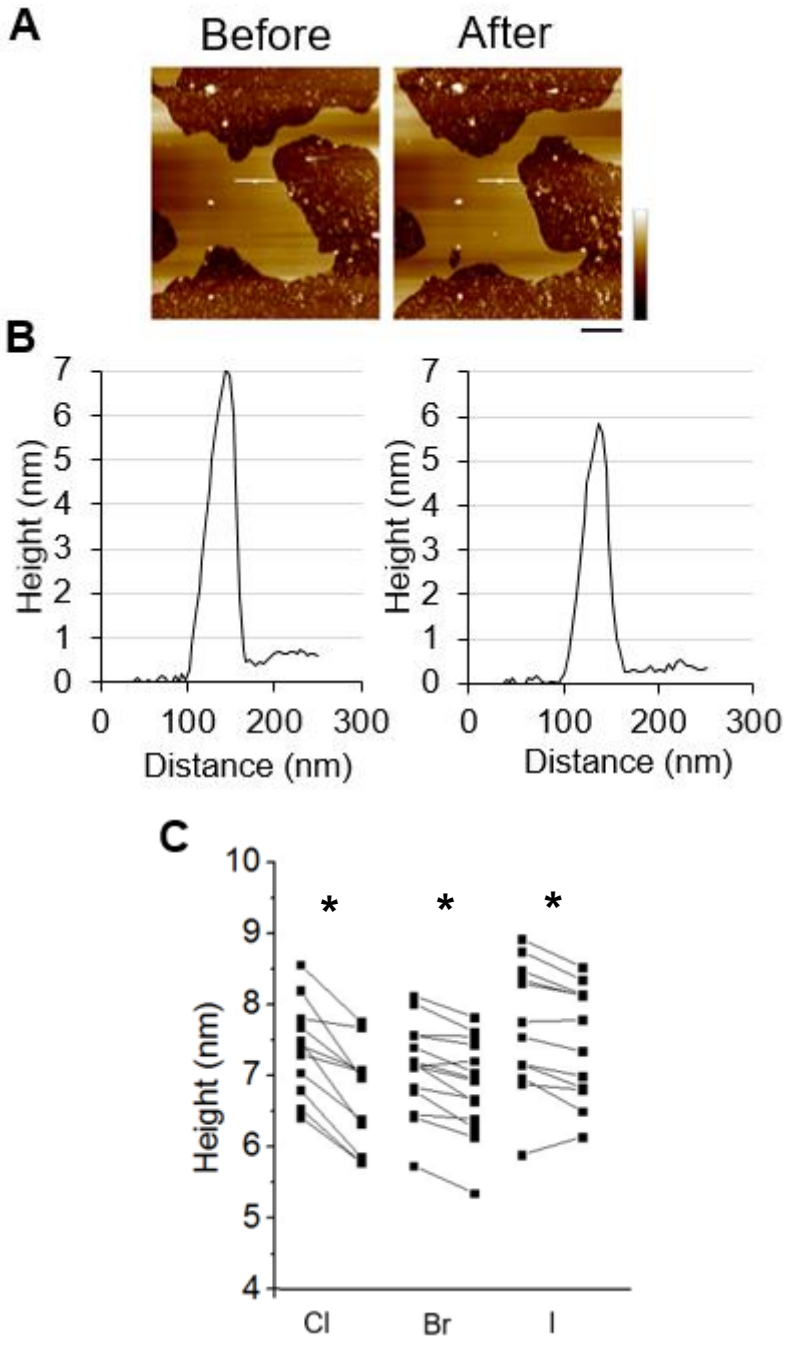

Figure 5.6. Effect of L-glutamate on GluA2 (flip) height in the presence of various anions. (A) Representative AFM images of a bilayer containing GluA2 receptors in NaCl (150 mM) before (left) and after (right) and after application of L-glutamate (10 mM). Scale bar, 400 nm; colour-height scale, -5 to 5 nm. (B) Sections through the receptor at the position indicated by the line in (A). Peak heights are 7.14 nm before and 5.83 nm after addition of glutamate. (C) Height data for individual receptors before and after addition of L-glutamate in the presence of the various anions. Asterisks indicate a significant difference ($P<0.01$, Student's paired two-tailed t-test).

5.2.3 Effects of cyclothiazide and CNQX on height responses of GluA2 (flip)

It has been reported that CTZ almost completely blocks AMPAR desensitization (Patneau *et al.*, 1993; Yamada and Tang, 1993) by stabilizing the LBD dimer interface in the active conformation (Sun *et al.*, 2002). I found that the L-glutamate-induced compression of GluA2 (flip) reported above was prevented by CTZ (100 µM). Specifically, in the presence of CTZ, the mean height reduction in response to L-glutamate was -0.03±0.07 nm (n=14). A similar lack of response to L-glutamate was observed in presence of 500 µM of the competitive antagonist CNQX (height reduction -0.10±0.07 nm; n=12). Together, these results indicate that the height reductions reflect entry of the receptors into the desensitized state.

Interestingly, the vertical compression caused by the large anions still occurred in the presence of CTZ: 0.45±0.19 nm (n=6) in NaBr and 0.66±0.05 nm (n=12) in NaI (Fig. 5.7). Although CTZ preserves the receptor in its active conformation, this result might indicate that some weakening of LBD dimer interface still occurs even in the presence of CTZ, and is revealed by pressure applied via the scanning tip.

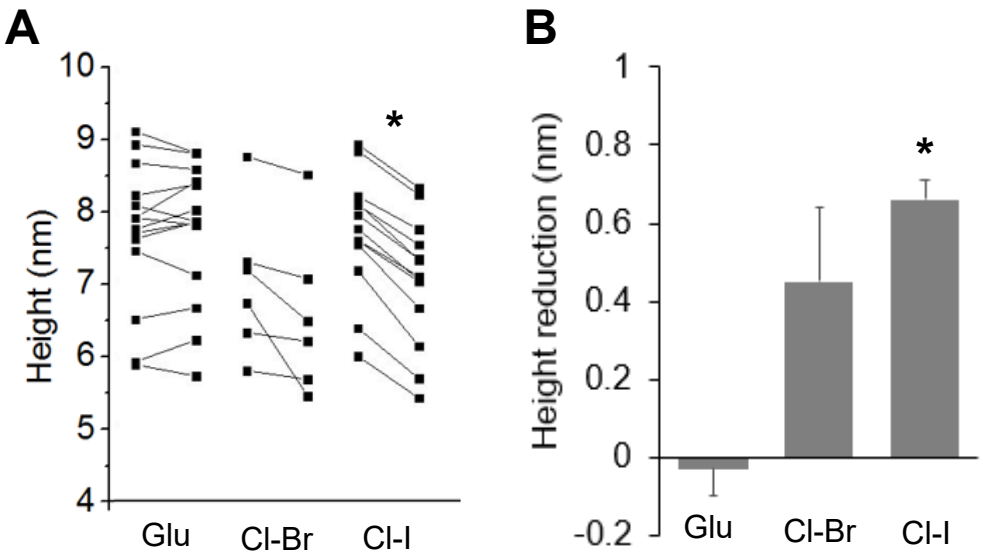

Figure 5.7. Effect of CTZ on GluA2 (flip) height changes. (A) Height data for individual receptors before and after addition of L-glutamate and before and after anion switches in presence of CTZ (100 µM). (B) Mean reductions in height of receptors in response to L-glutamate and anion substitutions in the presence of CTZ. NaCl, NaBr and NaI were all at 150 mM. The asterisk indicates a significant difference ($P<0.01$, Student's paired two-tailed *t*-test).

5.2.4 Effect of anion substitution and addition of L-glutamate on GluA2 (flop) height

The flop splice variant of HA-GluA2 was isolated and analysed as described above for GluA2 (flip). The receptor was integrated into liposomes (PC/PS, 3:1), and the proteoliposomes were deposited onto a mica surface to produce a supported proteolipid bilayer.

In contrast to the results obtained for the GluA2 flip isoform, there was little effect of anion substitution on the height of the flop isoform. Specifically, when the solution in the imaging chamber was changed from NaCl to either NaBr or NaI, the height reductions recorded were 0.06±0.06 nm (n=12) and 0.12±0.06 nm (n=15), respectively (Fig. 5.8). Despite this dramatically reduced effect of anion substitution, the flop isoform still responded robustly to addition of L-glutamate, with height reductions of 0.61±0.07 nm (n=10) in NaCl, 0.70 ± 0.14 nm (n=10) in NaBr, and 0.59±0.11 nm (n=11) in NaI (Fig 5.9).

Hence, the combined height reductions caused by NaBr or NaI substitution and L-glutamate application range from roughly 0.7 to 1.0 nm in both flip- and flop-type receptors. The key difference between the isoforms in these experiments is that most of the total compression is due to anion substitution in flip receptors, and to L-glutamate in flop receptors.

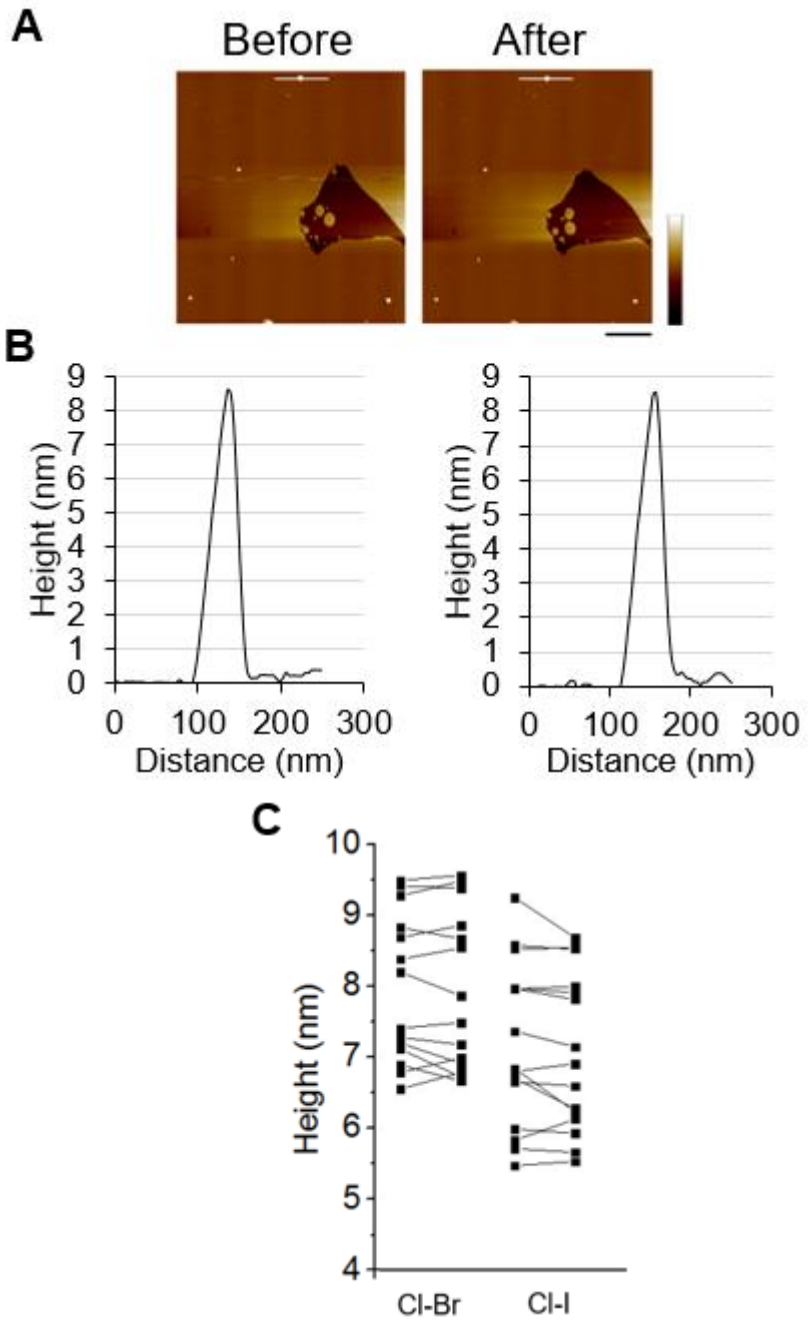

Figure 5.8. Effect of anion substitution on GluA2 (flop) height. (A) Representative AFM images of a bilayer containing GluA2 receptors in NaCl (150 mM; left) and after switching to NaI (150 mM; right). Scale bar, 400 nm; colour-height scale, -5 to 5 nm. (B) Sections through the receptor at the position indicated by the line in (A). Peak heights are 8.62 nm before and 8.57 nm after anion substitution. (C) Height data for individual receptors before and after Cl-Br and Cl-I substitutions. Height differences are non-significant (P>0.01, Student's paired two-tailed *t*-test).

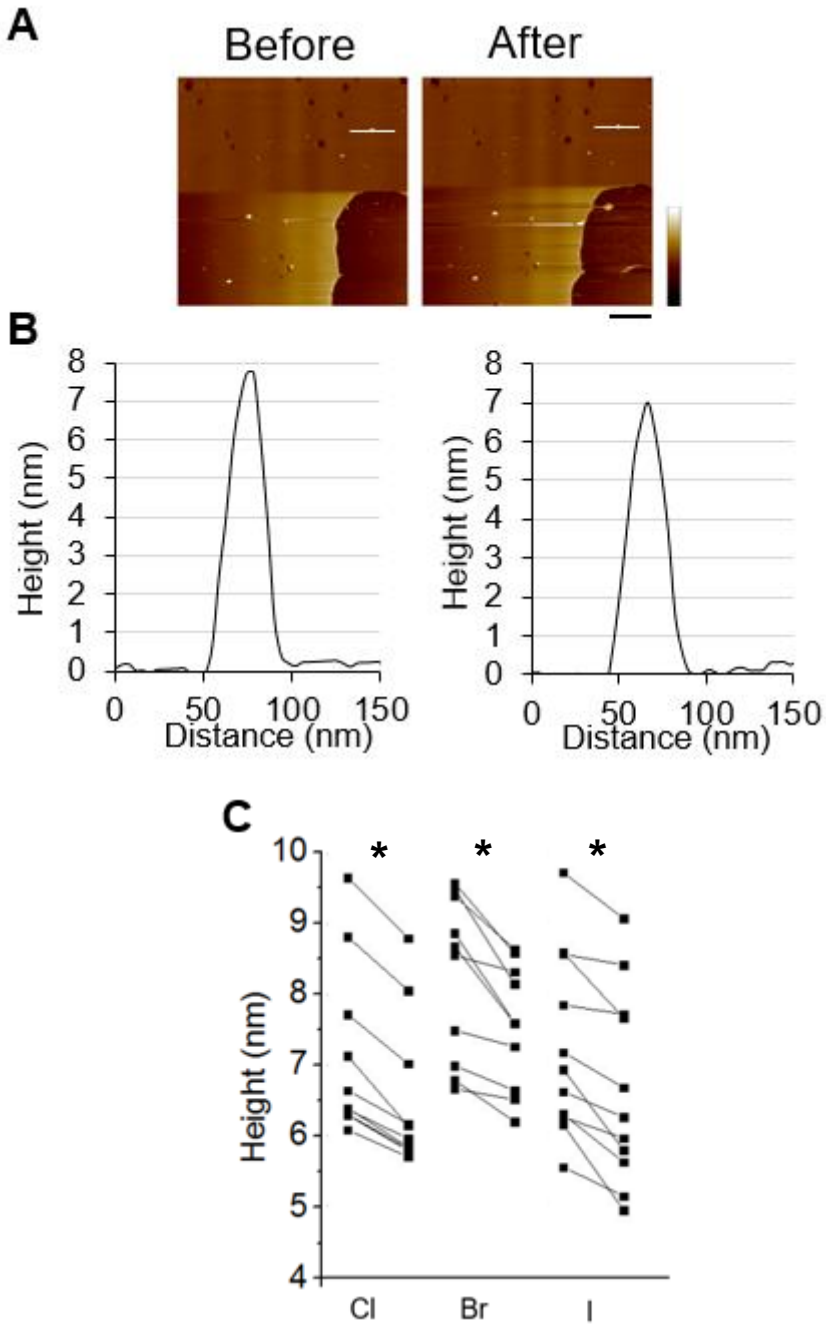

Figure 5.9. Effect of L-glutamate on GluA2 (flop) height in the presence of various anions. (A) Representative AFM images of a bilayer containing GluA2 receptors in NaCl (150 mM) before (left) and after (right) application of L-glutamate (10 mM). Scale bar, 400 nm; colour-height scale, -5 to 5 nm. (B) Sections through the receptor at the position indicated by the line in (A). Peak heights are 7.73 nm before and 7.03 nm after addition of L-glutamate. (C) Height data for individual receptors before and after addition of L-glutamate in the presence of the various anions. Asterisks indicate a significant difference ($P<0.01$, Student's paired two-tailed *t*-test).

5.2.5 Effect of anion substitution and addition of L-glutamate on heights of GluA2 (flip) S775N and L504A point mutants

I next explored the behavior of two point mutants of GluA2 (flip), namely S775N and L504A. The S775N mutant was of interest because it removes the functional response of the flip isoform to anions, as mentioned above (Fig. 5.3C). The L504A mutant also disrupts anion modulation of desensitization (Bowie lab, unpublished data), for reasons that are not entirely clear. One suggestion is that although L504 is not itself at the LBD dimer interface, the L-to-A mutation may indirectly affect the stability of the interface. Both mutants were isolated from detergent extracts of transfected tsA 201 cells by anti-HA immunoaffinity chromatography. After isolation, both proteins appeared as single bands at a molecular mass of 110 kDa on silver stained gels (Fig. 5.10), and both gave single immunopositive bands, again at 110 kDa, on anti-HA immunoblots. Isolated proteins were integrated into liposomes (PC/PS, 3:1), and the proteoliposomes were deposited onto a mica surface to produce supported proteolipid bilayers for AFM imaging.

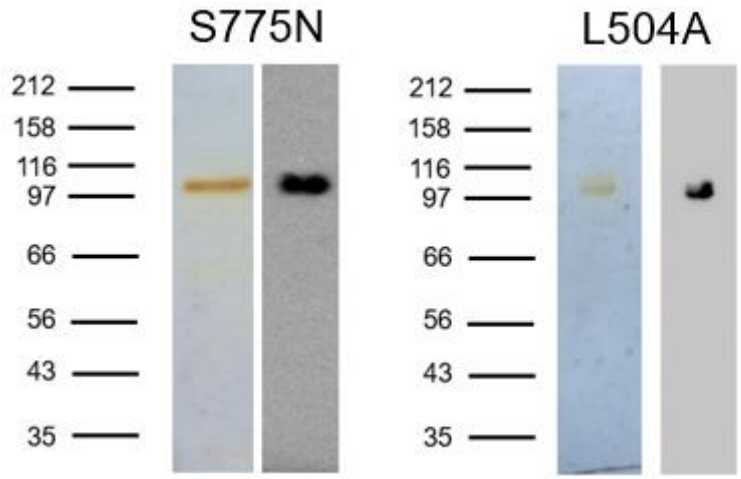

Figure 5.10. Isolation of the GluA2 (flip) point mutants S775N and L504A. HA-tagged proteins were isolated by anti-HA immunaffinity chromatography and analysed by SDS-PAGE followed by either silver staining (left panels) or immunoblotting using an anti-HA antibody (right panels).

Remarkably, both flip mutants (S775N and L504A) behaved like the flop isoform in response to both anion substitution and addition of L-glutamate (10 mM). Specifically, the vertical compression upon switching from NaCl to either NaBr or NaI was <0.1 nm, whereas L-glutamate caused a vertical compression of >0.6 nm. These results indicate that the two residues that were mutated play key roles in controlling the structural responses of the GluA2 receptor to allosteric stimuli. The height data obtained so far for the GluA2 receptor are summarized in Fig. 5.11.

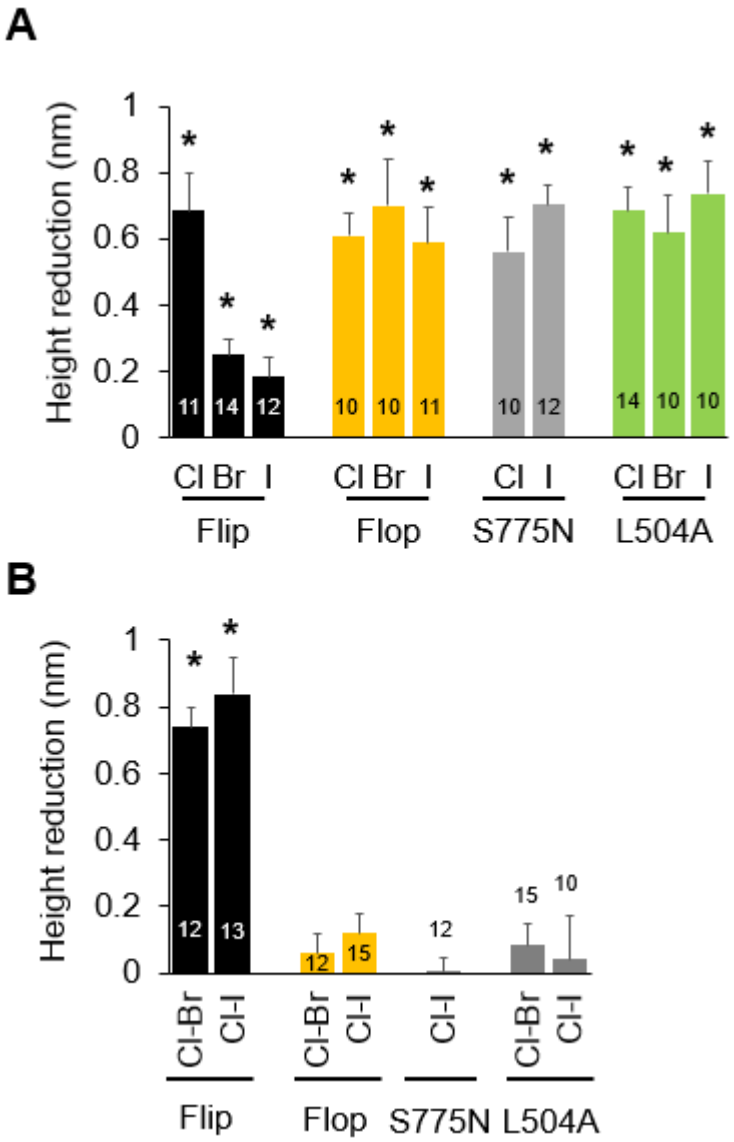

Figure 5.11. Responses of various forms of the GluA2 AMPAR to orthosteric and allosteric stimuli. (A) Height reductions in response to L-glutamate. (B) Height reductions in response to switches from NaCl to either NaBr or NaI (sample numbers indicated inside/above the bars). Asterisks indicate a significant difference ($P<0.01$, Student's paired two-tailed t-test).

5.2.6 Effect of removal of the ATD on height responses of GluA2 (flip)

The above results suggest that a single site of anion interaction with the GluA2 LBD mediates changes in receptor conformation. Nevertheless, it is difficult to formally exclude the possibility that the extracellular compression induced by bromide and iodide ions was structurally unrelated to the faster time course of desensitization observed in their presence. In this regard, the height changes measured by AFM could have been driven by movements in either the ATD or LBD layers. Meanwhile, it is clear that the sensitivity of desensitization kinetics to anions is solely attributable to allosteric effects on the LBD, because functional modulation by anions persisted in GluA2 (flip) receptors lacking their ATDs (Bowie lab, unpublished data). In an effort to link receptor compression more closely to changes in channel function, I carried out AFM measurements on GluA2 (flip) lacking the ATD (ΔATD-GluA2). Immunopurified ΔATD-GluA2 ran on silver stained gels and anti-HA immunoblots as a band at ~50 kDa, consistent with the expected reduction in size (Fig. 5.12A).

When bilayer-integrated ΔATD-GluA2 was subjected to AFM imaging, virtually no height changes could be induced (Fig. 5.12B) either by switching from NaCl to NaI (height reduction -0.05±0.08 nm; n=15) or by L-glutamate (10 mM) application in either NaCl (height reduction 0.03± 0.06 nm; n=13) or NaI (height reduction 0.13±0.1 nm; n=11).

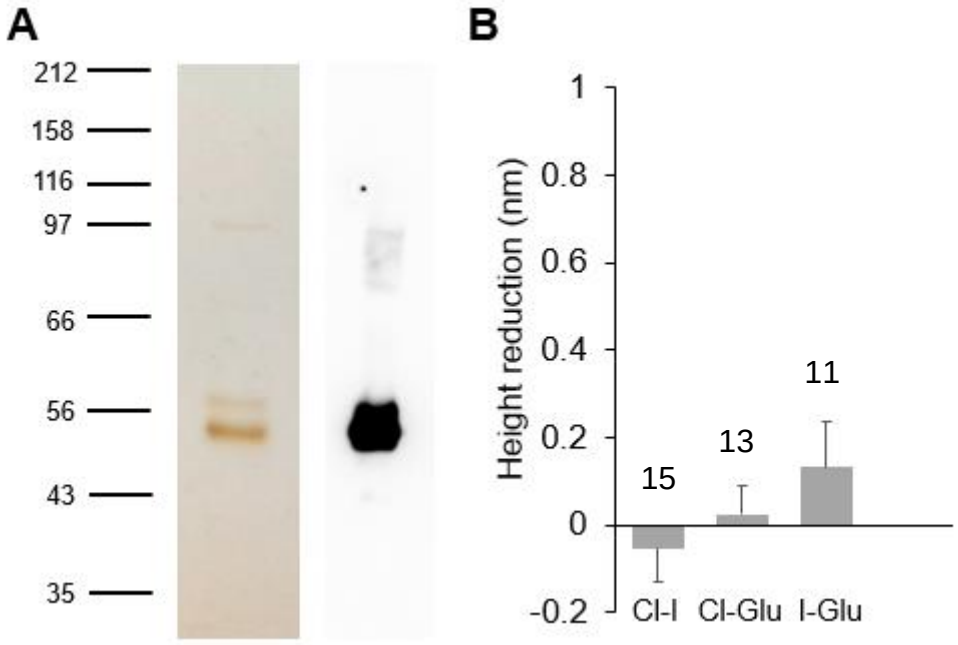

Figure 5.12. Responses of ΔATD-GluA2 (flip) to orthosteric and allosteric stimuli. (A) Isolation of ΔATD-GluA2. HA-tagged protein was isolated by anti-HA immunaffinity chromatography and analysed by SDS-PAGE followed by either silver staining (left panel) or immunoblotting using an anti-HA antibody (right panel). (B) Mean reductions in height of ΔATD-GluA2 in response to an anion switch or addition of L-glutamate (sample numbers indicated above the bars); height reductions are non-significant ($P>0.01$, Student's paired two-tailed *t*-test).

5.2.7 Effect of anion substitution and addition of L-glutamate on heights of on truncated ΔATD-GluA2-GFP (flip and flop)

In order to ensure that the lack of vertical compression in ΔATD-GluA2 (flip) receptors was not due to a limitation caused by the experimental conditions, such as the closeness of the LBD layer to the lipid membrane, I imaged GluA2 receptors (flip and flop) that contained an eGFP molecule in place of their respective ATDs.

As expected, immunopurified ΔATD-GluA2-GFP (both flip and flop) ran on silver stained gels and anti-HA immunoblots as bands at ~77 kDa (Fig. 5.13A).

The height reduction of the flip isoform in response to a switch from NaCl to NaI was partially restored by the addition of the GFP tag (0.32±0.08 nm; n=19), whereas the flop isoform still did not respond (0.02±0.05 nm; n=22). Addition of L-glutamate (10 mM) to the flip isoform caused no additional height reduction in NaI (0.06±0.10 nm; n=18). In NaCl, both flip and flop isoforms responded to addition of L-glutamate with a height reduction of ~0.3 nm (Fig. 5.13B).

The structural responsiveness of the ΔATD-GluA2-GFP (flip) construct to iodide suggests that there is no inherent property of the ATD layer that allows it to compress in response to halide ion substitution. More likely, some force that originates in the LBD is able to pull downward upon whatever protein domain is located in an N-terminal position. Consequently, it appears that anion-induced structural rearrangements do occur at the level of the LBD, but they are 'silent' within the LBD layer, when probed using AFM methods. Though the exact nature of these rearrangements is unclear at the moment, they are clearly sufficient to modulate desensitization behaviour following L-glutamate application.

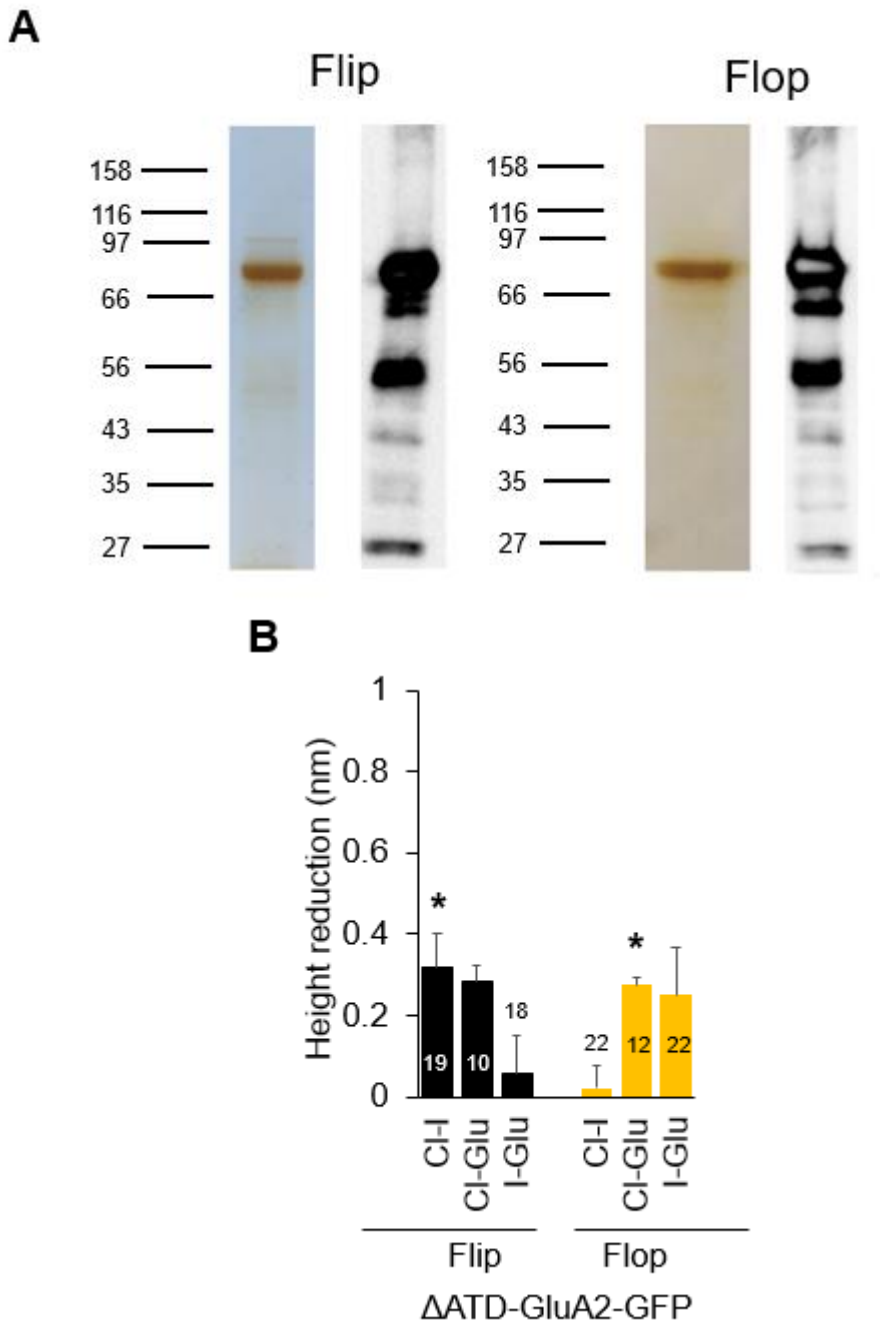

Figure 5.13. Responses of ΔATD-GluA2-GFP (flip and flop) to orthosteric and allosteric stimuli. (A) Isolation of ΔATD-GluA2-GFP. HA-tagged proteins were isolated by anti-HA immunaffinity chromatography and analysed by SDS-PAGE followed by either silver staining (left panels) or immunoblotting using an anti-HA antibody (right panels). (B) Mean reductions in height of ΔATD-GluA2-GFP in response to an anion switch or addition of L-glutamate (sample numbers indicated above the bars). Asterisks indicate a significant difference ($P<0.01$, Student's paired two-tailed *t*-test).

5.3 Discussion

A number of studies have shed light on the structural rearrangements accompanying AMPAR activation and desensitization by reporting intact, atomic-resolution GluA2 structures in several distinct, agonist-bound states (Meyerson *et al.*, 2014; Durr *et al.*, 2014). However, the conformational flexibility of full-length AMPARs both in the absence and presence of bound agonists is poorly characterized. In this Chapter, I have described attempts to explore the extent to which allosteric effectors influence the conformation of resting-state AMPARs, and the structural consequences of activation of the receptors by L-glutamate.

Because anions had previously been shown to regulate GluA1 desensitization kinetics (Bowie, 2002), I decided to use halide substitution as an allosteric manipulation. I found a relationship between halide radius and compression of intact, resting-state AMPARs that correlates with the rate of desensitization in response to L-glutamate. Furthermore, I have isolated the site of action of anions to the LBD dimer interface. A mutation at this site (S775N), within the flip/flop alternate splicing cassette, disrupts the structural (and functional) effects of anion substitution.

Following previous AFM studies on iGluRs (Balasuriya *et al.*, 2014; Suzuki *et al.*, 2013), I showed in Chapter 3 that AFM is capable of sensing a vertical compression of kainate receptors in response to agonist binding. Consistent with my results for the kainate receptor, I have shown in the present chapter that the addition of L-glutamate to either flip or flop isoforms of the GluA2 AMPAR in the presence of NaCl causes a significant reduction in receptor height that is blocked by the receptor antagonist CNQX and (in the case of flip) by the desensitization blocker CTZ. These results indicate that vertical compression occurs as the receptor enters the desensitized state, in agreement with the crystal structure proposed by Dürr *et al.* (2014), and with my own results for the KAR.

It is possible that the larger halide ions could affect the stability of the dimer interface by interacting with surrounding polar and non-polar residues (Dauter and Dauter, 2001), which could eventually interrupt important endogenous interactions between subunits. An inter-subunit anion binding site has also been reported for the acid-sensing ion channel ASIC1a (Jasti *et al.*, 2007), which also showed a faster desensitization rate in the presence of larger anions (Kusama *et al.*, 2010).

It is difficult to explain why flip GluA2 receptors were less sensitive to anions than their flop counterparts. As mentioned above, a pair of bromide ions is positioned near the base of the D1-D1 interface in the crystal structure of the LBD dimer. This anion binding site is located in a somewhat hydrophobic space surrounded by P515 and L772 from one subunit, I502 and P515 from the partner subunit, and capped by K514. More importantly, the crystal structure suggests that larger halide ions can easily access the dimer interface, and it is well known that desensitization involves destabilization of this dimer interface (Sun *et al.,* 2002). Further, it has been reported that position N775, along with N765 and A766 at the dimer interface are responsible for the relatively fast desensitization of the flop isoform compared with flip (Quirk *et al.,* 2004). These positions, then, may also contribute to the difference in the effect of anions on the two splice variants. This suggestion is supported by the effect of the S775N point mutation in GluA2 (flip) which converted its behaviour in the anion substitution experiment to that of the flop isoform. Because of its bulkiness, N775 could prevent the larger ions from disturbing the dimer interface. In addition, a hydrogen bond formed between N775 and S750 in flop, which is not present in flip, may counteract the ability of halide ions to destabilize the dimer interface.

It should also be noted that two other point mutants of the flip isoform of GluA2 (T765N and P766A) showed strong anion modulation of desensitization (Bowie lab, unpublished data). Given that these residues lie at the top of the dimer interface, it appears that the difference in vertical compression between the flip and flop isoforms can be attributed solely to residue 775. This is in agreement with the crystal structure, where the two bromide ions sit in the lower D1-D1 LBD dimer interface.

Overall, the experiments described in this chapter have identified a novel allosteric site that can ‘prime’ AMPARs to respond in a specific manner upon agonist binding. Further, as far as I am aware, this is the first time that conformational transitions between resting and desensitized states in response to allosteric effectors have been visualized under near-physiological conditions.

6. Conclusions and perspectives

In this dissertation, I report the use of fast-scan AFM imaging to monitor the dynamics of iGluRs built from GluK2 and GluA2. My results add to our understanding of the behaviour of these two types of iGluRs in response to activation. Importantly, and in contrast to recent studies using X-ray crystallography and cryo-EM, I have imaged wild type, full-length receptors integrated into lipid bilayers under near-physiological conditions, in some cases in a time-resolved manner. This has allowed me to demonstrate that KARs and AMPARs are extremely flexible structures that exhibit global structural changes in response to both orthosteric and allosteric challenges.

When I began my experiments, it had already been shown by members of my research group that the co-agonists L-glutamate and glycine trigger a ~1-nm vertical compression of the extracellular domain of the GluN1/GluN2A NMDAR integrated into supported lipid bilayers (Suzuki *et al.,* 2013). This reduction in height did not occur in the absence of the co-agonist glycine or in the presence of the selective NMDAR antagonist D-AP5, indicating that the observed structural change required receptor activation. A similar reduction in height was seen in the GluN1/GluN3 excitatory glycine receptor (Balasuriya *et al.,* 2014) in response to glycine. In my study, I showed that the KAR and the AMPAR also undergo a ~1 nm height reduction in response to activation, which in both cases was blocked by the antagonist CNQX. Hence, all three major types of iGluR undergo a similar vertical compression in response to activation.

To follow the kinetics of the height change in the KAR, I switched from taking successive individual images of the receptor particles to 'line-scanning', where the Y scanning axis was disabled and the AFM tip was scanned repeatedly back and forth over an identified receptor (time per line: 50 ms) while caged L-glutamate was photolysed. The vertical compression in response to uncaging of glutamate occurred with a time constant of a few seconds. No reduction was seen either with UV irradiation in the absence of caged glutamate or with photolysis of caged L-glutamate in the presence of CNQX. Significantly, the point mutant D776K, which does not desensitize, did not undergo the height change, whereas the mutant L783C, which may desensitize without passing through the open state, did. In non-time-resolved experiments, I also showed that the activation-induced vertical compression of the AMPAR did not occur in the presence of the desensitization blocker CTZ. Hence, for both KARs and AMPARs, the vertical compression occurs as the receptor enters the desensitized state.

Clearly, the time-scale over which the observed vertical compression is occurring (seconds) is much longer than the time-scales typically encountered in electrophysiological recordings of channel activation, deactivation and desensitization (milliseconds). It is likely, therefore, that in my experiments I am looking at structural changes that may be electrically silent.

After the activation-induced vertical compression occurs in the KAR, the receptor undergoes fluctuations in height that likely reflect switching of the receptor between two states (perhaps associated with repeated cycles of agonist binding and unbinding). Analyses of these fluctuations enabled me to estimate the thermodynamic parameters for this switching. Assuming that what I call the 'control' and 'non-control' states represent the non-desensitized and the desensitized receptor, respectively, the analysis indicates that movement into the desensitized state is energetically favoured, as predicted previously on the basis of molecular dynamic simulations (Ruan *et al*., 2017).

In AFM images, the receptors appeared as double-blob structures, with each blob representing a pair of ATDs. Using sequential imaging at a rate of 1 frame/s, I found that for both KARs and AMPA receptors, the relative mobility of the ATDs became greater after stimulation. Further, at low glutamate concentrations, the ATDs of the (rapidly desensitizing) flop splice variant of the AMPA receptor were more mobile than those of the (more slowly desensitizing) flip splice variant. It is conceivable that the greater mobility of the flop splice variant might be connected with its more short-lived functional response to activation.

In addition to the structural effects induced in the iGluRs by the orthosteric ligand L-glutamate, I found that large halide ions (bromide and iodide), acting at an allosteric site, also caused a vertical compression of the AMPAR by acting at the level of the LBDs. These structural effects of halide ions were revealed as part of a collaborative study which also showed that the same ions altered the duration of agonist-evoked channel activity, and that the anion binding site was located at the interface between LBD dimers. Importantly, this binding site is close to the site at which flip-flop alternative splicing occurs, and, consistent with this juxtaposition, both structural and functional effects of the anions were isoform-dependent. Together, these results demonstrate that resting-state allosteric interactions can 'prime' AMPA receptors for their eventual response to agonists.

Interestingly, there is a long history of using potassium bromide as an antiepileptic therapy, although the mechanism underlying its action is unknown. In fact, bromide was the first ‘modern’ treatment for epilepsy, dating from 1857 (Clouston, 1868; Pearce, 2002). However, because of the side effects of bromide therapy on the nervous system, skin, and gastrointestinal tract, nowadays it is used only as a potential ‘drug of tertiary choice’ in the treatment of epilepsy in children (Korinthenberg *et al.,* 2007). It is tempting to speculate that the modulatory effect of larger halide ions on AMPAR structure and function reported here might be relevant to the therapeutic effects of bromide. In addition, a search for other non-toxic allosteric modulators of AMPARs might now be warranted.

Now that the fast-scan imaging technique has been shown to reveal key features of iGluR behaviour, further experiments can be envisaged. For example, it is well known that both KARs and AMPARs interact in a functionally significant manner with various auxiliary proteins (e.g. TARPs and NETOs, respectively). It would be very interesting to determine how the structural dynamics of the intact receptors are affected by interactions with these auxiliary subunits. Looking more broadly, it would also be fascinating to apply a similar imaging approach to other important integral membrane signalling proteins, such as members of the G protein-coupled receptor family, and the voltage-gated ion channels.

References

Akamatsu M, Yamashita T, Hirose N, Teramoto S, Kwak S (2016). The AMPA receptor antagonist perampanel robustly rescues amyotrophic lateral sclerosis (ALS) pathology in sporadic ALS model mice. Sci Rep 6: 28649.

Alam A, Jiang Y (2009). High-resolution structure of the open NaK channel. Nat Struct Mol Biol 16: 30-34.

Alberdi E, Sánchez-Gómez MV, Torre I, Domercq M, Pérez-Samartín A, Pérez-Cerdá F, Matut C (2006). Activation of kainate receptors sensitizes oligodendrocytes to complement attack. J Neurosci 26: 3220-3228.

Alberts B, Johnson A, Lewis J, Raff M, Roberts K, Walter P (2002). Molecular Biology of the Cell, 4th edition. New York: Garland Science.

Alexander SPH, Mathie A, Peters JA (2011). Guide to Receptors and Channels (GRAC), 5th edn. Br J Pharmacol 164 (Suppl 1): S1-S324.

Andersson O, Stenqvist A, Attersand A, von Euler G (2001). Nucleotide sequence, genomic organization, and chromosomal localization of genes encoding the human NMDA receptor subunits NR3A and NR3B. Genomics 78: 178-184.

Ando T, Uchihashi T, Kodera N (2013). High-speed AFM and applications to biomolecular systems. Annu Rev Biophys 42: 393-414.

Andreadis A (2005). Tau gene alternative splicing: expression patterns, regulation and modulation of function in normal brain and neurodegenerative diseases. Biochem Biophys Acta 1739: 91-103.

Armstrong N, Gouaux E (2000). Mechanisms for activation and antagonism of an AMPA-sensitive glutamate receptor: Crystal structures of the GluR2 ligand binding core. Neuron 28: 165-181.

Armstrong N, Jasti J, Beich-Frandsen M, Gouaux E (2006). Measurement of conformational changes accompanying desensitization in an ionotropic glutamate receptor. Cell 127: 85-97.

Armstrong N, Sun Y, Chen G-Q, Gouaux E (1998). Structure of a glutamate receptor ligand binding core in complex with kainate. Nature 395: 913-917.

Aroca JD, Sanchez-Pinera P, Corbalan-Garcia S, Conesa-Zamora P, de Godos A, Gomez-Fernandez JC (2001). Correlation between the effect of the anti-neoplastic ether lipid 1-O-octadecyl-2-O-methyl-glycero-3-phosphocholine on the membrane and the activity of protein kinase C-alpha. Eur J Biochem 268: 6369-6378.

Arora A, Tamm LK (2001). Biophysical approaches to membrane protein structure determination. Curr Opin Struct Biol 11: 540-547.

Ascher, P, Marty A, Neild TO (1978). Life time and elementary conductance of the channels mediating the excitatory effects of acetylcholine in *Aplysia* neurones. J Physiol 278: 177-206.

Awobuluyi M, Yang J, Ye Y, Chatterton JE, Godzik A, Lipton SA, Zhang D (2007). Subunit-specific roles of glycine-binding domains in activation of NR1/NR3 N-methyl-D-aspartate receptors. Mol Pharmacol 71: 112-122.

Balannik V, Menniti FS, Paternain AV, Lerma J, Stern-Bach Y (2005). Molecular Mechanism of AMPA Receptor Noncompetitive Antagonism. Neuron 48: 279-288.

Balasuriya D, Takahashi H, Srivats S, Edwardson JM (2014). Activation-induced structural change in the GluN1/GluN3A excitatory glycine receptor. Biochem Biophys Res Commun 450: 1452-1457.

Baro AM, Miranda R, Alaman J, Garcia N, Binnig G, Rohrer H, et al. (1985). Determination of surface topography of biological specimens at high resolution by scanning tunnelling microscopy. Nature 315: 253-254.

Bartesaghi A, Merk A, Banerjee S, Matthies D, Wu X, Milne JL, Subramaniam S (2015). 2.2 Å resolution cryo-EM structure of β-galactosidase in complex with a cell-permeant inhibitor. Science 348: 1147-1151.

Başkaya MK, Rao AM, Donaldson D, Prasad MR, Dempsey RJ (1997). Protective effects of ifenprodil on ischemic injury size, blood-brain barrier breakdown and edema formation in focal cerebral ischemia. Neurosurgery 40: 364-370.

Belandia IU, Stokes DL (2010). Present and future of membrane protein structure determination by electron crystallography. Adv Protein Chem Struct Biol 81: 33-60.

Berget SM, Moore C, Sharp PA (1977). Spliced segments at the 5’ terminus of adenovirus late mRNA. Proc Natl Acad Sci USA 7: 3171-3175.

Berman HM, Westbrook J, Feng Z, Gilliland G, Bhat TN, Weissig H, et al. (2000). The Protein Data Bank Nucleic Acids Research 28: 235-242. URL: *www.rcsb.org.*

Bertolino M, Baraldi M, Parenti C, Braghiroli D, DiBella M, Vicini S, Costa E (1993). Modulation of AMPA/kainate receptors by analogues of diazoxide and cyclothiazide in thin slices of rat hippocampus. Receptors and Channels 1: 267-278.

Bettler B, Boulter J, Hermans-Borgmeyer I, O'Shea-Greenfield A, Deneris ES, Moll C, et al. (1990). Cloning of a novel glutamate receptor subunit, GluR5: expression in the nervous system during development. Neuron 5: 583-595.

Bettler B, Egebjerg J, Sharma G, Pecht G, Hermans-Borgmeyer I, Moll C, et al. (1992). Cloning of a putative glutamate receptor: a low affinity kainate-binding subunit. Neuron 8: 257-265.

Binnig G, Quate CF, Gerber C (1986). Atomic force microscope. Phys Rev Lett 56: 930-933.

Black DL (2003). Mechanisms of alternative pre-messenger RNA splicing. Annu Rev Biochem 72: 291-336.

Blanke ML, VanDongen AMJ (2009). Activation Mechanisms of the NMDA Receptor. In: Van Dongen AM, editor. Biology of the NMDA Receptor. Boca Raton (FL): CRC Press/Taylor & Francis, Chapter 13.

Boulter J, Hollmann M, O'Shea-Greenfield A, Hartley M, Deneris E, Maron C, Heinemann S (1990). Molecular cloning and functional expression of glutamate receptor subunit genes. Science 249: 1033-1037.

Bowie D (2002). External anions and cations distinguish between AMPA and kainate receptor gating mechanisms. J Physiol 539: 725-733.

Brown DG, Krupp JJ (2006). N-methyl-D-aspartate receptor (NMDA) antagonists as potential pain therapeutics. Curr Topics Med Chem 6: 749-770.

Buchholtz F, Schinor N, Schneider FW (2002). Stochastic nonlinear dynamics: How many ion channels are in a single neuron? J Phys Chem B 106: 5086-5090.

Cai SX (2006). Glycine/NMDAR antagonists as potential CNS therapeutic agents: ACEA-1021 and related compounds. Curr Top Med Chem 6: 651-662.

Cais O, Herguedas B, Krol K, Cull-Candy SG, Farrant M, Greger IH (2014). Mapping the interaction sites between AMPA receptors and TARPs reveals a role for the receptor N-terminal domain in channel gating. Cell Rep 9: 728-740.

Carpenter EP, Beis K, Cameron AD, Iwata S (2008). Overcoming the challenges of membrane protein crystallography. Curr Opin Struct Biol 18: 581-586.

Castillo PE, Malenka RC, Nicoll RA (1997). Kainate receptors mediate a slow postsynaptic current in hippocampal CA3 neurons. Nature 388: 182-186.

Chang PK, Verbich D, McKinney RA (2012). AMPA receptors as drug targets in neurological disease - advantages, caveats, and future outlook. Eur J Neurosci 35: 1908-1916.

Chatterton JE, Awobuluyi M, Premkumar LS, Takahashi H, Talantova M, Shin Y, et al. (2002). Excitatory glycine receptors containing the NR3 family of NMDA receptor subunits. Nature 415: 793-798.

Chaudhry C, Weston MC, Schuck P, Rosenmund C, Mayer ML (2009). Stability of ligand-binding domain dimer assembly controls kainate receptor desensitization. EMBO J 28: 1518-1530.

Chazot PL (2004). The NMDAR NR2B subunit: a valid therapeutic target for multiple CNS pathologies. Curr Med Chem 11: 389-396.

Chen Mo, Manley JL (2009). Mechanisms of alternative splicing regulation: insights from molecular and genomics approaches. Nat Rev Mol Cell Biol 10: 741-754.

Cheng Y (2015). Single-particle cryo-EM at crystallographic resolution. Cell 161: 450-457.

Choi DW (1988). Calcium-mediated neurotoxicity: relationship to specific channel types and role in ischemic damage. Trends Neurosci 11: 465-469.

Choi DW, Rothman SM (1990). The role of glutamate neurotoxicity in hypoxic-ischemic neuronal death. Annu Rev Neurosci 13: 171-182.

Chong DJ, Lerman AM (2016). Practice update: Review of anticonvulsant therapy. Curr Neurol Neurosci Rep 16: 39.

Chow LT, Gelinas RE, Broker TR, Roberts RJ (1977). An amazing sequence arrangement at the 5’ ends of adenovirus 2 messenger RNA. Cell 12: 1-8.

Christopoulos A (2002). Allosteric binding sites on cell surface receptors: novel targets for drug discovery. Nat Rev Drug Discov 1: 198-210.

Clancy S (2008). RNA splicing: introns, exons and spliceosome. Nature Education 1: 31.

Clarke VR, Ballyk BA, Hoo KH, Mandelzys A, Pellizzari A, Bath CP, et al. (1997). A hippocampal GluR5 kainate receptor regulating inhibitory synaptic transmission. Nature 389: 599-603.

Clayton A, Siebold C, Gilbert RJ, Sutton GC, Harlos K, McIlhinney RA, et al. (2009). Crystal structure of the GluR2 amino-terminal domain provides insights into the architecture and assembly of ionotropic glutamate receptors. J Mol Biol 392:1125-1132.

Clouston TS (1868). Experiments to determine the precise effect of bromide of potassium in epilepsy. J Ment Sci 14: 305-321.

Conn PJ, Christopoulos A, Lindsley CW (2009). Allosteric modulators of GPCRs: a novel approach for the treatment of CNS disorders. Nat Rev Drug Discov 8: 41-54.

Contractor A, Mulle C, Swanson GT (2011). Kainate receptors coming of age: milestones of two decades of research. Trends Neurosci 34: 154-163.

Cooper GM (2000). The Cell: A Molecular Approach. 2nd edition. Sunderland (MA): Sinauer Associates.

Copits BA, Swanson GT (2012). Dancing partners at the synapse: auxiliary subunits that shape kainate receptor function. Nature Rev Neurosci 13: 675-686.

Cossart R, Esclapez M, Hirsch JC, Bernard C, Ben-Ari Y (1998). GluR5 kainate receptor activation in interneurons increases tonic inhibition of pyramidal cells. Nat Neurosci 1: 470-478.

Crampton N, Yokokawa M, Dryden DT, Edwardson JM, Rao DN, Takeyasu K, et al. (2007). Fast-scan atomic force microscopy reveals that the type III restriction enzyme EcoP15I is capable of DNA translocation and looping. Proc Natl Acad Sci USA 104: 12755-12760.

Cull-Candy S, Kelly L, Farrant M (2006). Regulation of Ca^{2+} permeable AMPA receptors: synaptic plasticity and beyond. Curr Opin Neurobiol 16: 288-297.

Cull-Candy SG, Leszkiewicz DN (2004). Role of distinct NMDA receptor subtypes at central synapses. Sci. STKE 255: re16.

Dauter Z, Dauter M (2001). Entering a new phase: using solvent halide ions in protein structure determination. Structure 9: R21-26.

Dawe GB, Musgaard M, Andrews ED, Daniels BA, Aurousseau MR, Biggin PC, Bowie D (2013). Defining the structural relationship between kainate-receptor deactivation and desensitization. Nat Struct Mol Biol 20: 1054-1061.

de Pablo PJ, Carrión-Vázquez M (2014). Imaging biological samples with atomic force microscopy. Cold Spring Harbor Protocols: pdb. top080473.

De Rosier DJ, Klug A (1968). Reconstruction of three dimensional structures from electron micrographs. Nature 217: 130-134.

Deisenhofer J, Epp O, Miki K, Huber R, Michel H (1985). Structure of the protein subunits in the photosynthetic reaction centre of *Rhodospeudomonas viridis* at 3 Å resolution. Nature 318: 618-624.

Delorme R, Krebs M-O, Chabane N, Roy I, Millet B, Mouren-Simeoni MC, et al. (2004). Frequency and transmission of glutamate receptors GRIK2 and GRIK3 polymorphisms in patients with obsessive compulsive disorder. Neuroreport 15: 699-702.

Dingledine R, Borges K, Bowie D, Traynelis SF (1999). The glutamate receptor ion channels. Pharmacol Rev 51: 7-62.

Dorobantu LS, Goss GG, Burrell RE (2012). Atomic force microscopy: a nanoscopic view of microbial cell surfaces. Micron 43: 1312-1322.

Doyle DA, Morais Cabral J, Pfuetzner RA, Kuo A, Gulbis JM, Cohen SL, et al. (1998). The structure of the potassium channel: molecular basis of K^+ conduction and selectivity. Science 280: 69-77.

Dravid SM, Prakash A, Traynelis SF (2008). Activation of recombinant NR1/NR2C NMDA receptors. J Physiol 586: 4425-4439.

Drew D, Froderberg L, Baars L, de Gier JW (2003). Assembly and overexpression of membrane proteins in *Escherichia coli*. Biochim Biophys Acta 1610: 3-10.

Dubochet J, Adrian M, Chang JJ, Homo JC, Lepault J, McDowall AW, Schultz P (1988). Cryo-electron microscopy of vitrified specimens. Quart Rev Biophys 21: 129-228.

Dufrêne YF (2008). Towards nanomicrobiology using atomic force microscopy. Nat Rev Microbiol 6: 674-680.

Dürr KL, Chen L, Stein RA, Zorzi RD, MihaelaFolea I, Walz T, et al. (2014). Structure and dynamics of AMPA receptor GluA2 in resting, pre-open and desensitized states. Cell 158: 778-792.

Dutta S, Das S, Guhathakurta S, Sen B, Sinha S, Chatterjee A, et al. (2007). Glutamate receptor 6 gene (GluR6 or GRIK2) polymorphisms in the Indian population: a genetic association study on autism spectrum disorder. Cell Molec Neurobiol 27: 1035-1047.

Edmonds B, Gibb AJ, Colquhoun D (1995). Mechanisms of activation of glutamate receptors and the time course of excitatory synaptic currents. Annu Rev Physiol 57: 495-519.

Edwardson JM, Henderson RM (2004). Atomic force microscopy and drug discovery. Drug Discov Today 9: 64-71.

Egebjerg J, Bettler B, Hermans-Borgmeyer I, Heinemann S (1991). Cloning of a cDNA for a glutamate receptor subunit activated by kainate but not AMPA. Nature 351: 745-748.

Ehlers MD, Mammen AL, Lau L-F, Huganir RL (1996). Synaptic targeting of glutamate receptors. Curr Opin Cell Biol 8: 484-489.

Engel A, Gaub HE (2008). Structure and mechanics of membrane proteins. Annu Rev Biochem 77: 127-148.

Engel A, Müller DJ (2000). Observing single biomolecules at work with the atomic force microscope. Nat Struct Biol 7: 715-718.

Engelman DM (1971). Lipid bilayer structure in the membrane of *Mycoplasma laidlawii*. J Mol Biol 58: 153-165.

Erni R, Rossell MD, Kisielowski C, Dahmen U (2009). Atomic-resolution imaging with a sub-50-pm electron probe. Phys Rev Lett 102: 096101.

Erreger K, Chen PE, Wyllie DJ, Traynelis SF (2004). Glutamate receptor gating. Crit Rev Neurobiol 16: 187-224.

Farlow MR (2004). NMDAR antagonists. A new therapeutic approach for Alzheimer's disease. Geriatrics 59: 22-27.

Fernandez C, Wuthrich K (2003). NMR solution structure determination of membrane proteins reconstituted in detergent micelles. FEBS Letts 555: 144-150

Fischer N, Neumann P, Konevega AL, Bock LV, Ficner R, Rodnina MV, Stark H (2015). Structure of the *E. coli* ribosome-EF-Tu complex at <3 Å resolution by Cs-corrected cryo-EM. Nature 520: 567-570.

Fleck MW, Cornell E, Mah SJ (2003). Amino-acid residues involved in glutamate receptor 6 kainate receptor gating and desensitization. J Neurosci 23: 1219-1227.

Fotiadis D (2012). Atomic force microscopy for the study of membrane proteins. Curr Opin Biotechnol 23: 510-515.

Franz C, Puech P-H (2008). Atomic force microscopy: a versatile tool for studying cell morphology, adhesion and mechanics. Cell Molec Bioeng 1: 289-300.

Frenkel EJ, Roelofsen B, Brodbeck U, van Deenen LL, Ott P (1980). Lipid-protein interactions in human erythrocyte-membrane acetylcholinesterase. Modulation of enzyme activity by lipids. Eur J Biochem 109: 377-382.

Frerking M, Malenka R, Nicoll R (1998). Synaptic activation of kainate receptors on hippocampal interneurons. Nat Neurosci 1: 479-486.

Fujiyoshi Y (2011). Electron crystallography for structural and functional studies of membrane proteins. J Electron Microsc 60 (Suppl 1): S149-S159.

Furukawa H, Gouaux E (2003). Mechanisms of activation, inhibition and specificity: crystal structures of the NMDA receptor NR1 ligand-binding core. EMBO J 22: 2873-2885.

Furukawa H, Singh SK, Mancusso R, Gouaux E (2005). Subunit arrangement and function in NMDA receptors. Nature 438: 185-192.

Gan Y (2009). Atomic and subnanometer resolution in ambient conditions by atomic force microscopy. Sur Sci Rep 64: 99-121

Garcia EP, Mehta S, Blair LA, Wells DG, Shang J, Fukushima T, et al. (1998). SAP90 binds and clusters kainate receptors causing incomplete desensitization. Neuron 21: 727-739.

Gécz J (2010). Glutamate receptors and learning and memory. Nat Genet 42: 925-926.

Gerber C, Lang HP (2006). How the doors to the nano world were opened. Nat Nanotechnol 1: 3-5.

Gielen M, Siegler Retchless B, Mony L, Johnson JW, Paoletti P (2009). Mechanism of differential control of NMDA receptor activity by NR2 subunits. Nature 459: 703-707.

Goñi FM, Alonso A (2000). Spectroscopic techniques in the study of membrane solubilization, reconstitution and permeabilization by detergents. Biochim Biophys Acta 1508: 51-68.

Grandbois M, Clausen-Schaumann H, Gaub H (1998). Atomic force microscope imaging of phospholipid bilayer degradation by phospholipase A2. Biophys J 74: 2398-2404.

Grant T, Grigorieff N (2015). Measuring the optimal exposure for single particle cryo-EM using a 2.6 Å reconstruction of rotavirus VP6. eLife 4: e06980.

Greger IH, Akamine P, Khatri L, Ziff EB (2006). Developmentally regulated, combinatorial RNA processing modulates AMPA receptor biogenesis. Neuron 51: 85-97.

Greger IH, Ziff EB, Penn AC (2007). Molecular determinants of AMPA receptor subunit assembly. Trends Neurosci 30: 407-416.

Grunwald ME, Kaplan JM (2003). Mutations in the ligand-binding and pore domains control exit of glutamate receptors from the endoplasmic reticulum in *C. elegans*. Neuropharmacology 45: 768-776.

Hansen KB, Yuan H, Traynelis SF (2007). Structural aspects of AMPA receptor activation, desensitization and deactivation. Curr Opin Neurobiol 17: 281-288.

Helenius A, Simons K (1975). Solubilization of membranes by detergents. Biochim Biophys Acta 415: 29-79.

Henderson R, Baldwin JM, Ceska TA, Zemlin F, Beckmann E, Downing KH (1990). Model for the structure of bacteriorhodopsin based on high-resolution electron cryo-microscopy. J Mol Biol 213: 899-929.

Henderson R, Unwin PNT (1975). Three-dimensional model of purple membrane obtained by electron microscopy. Nature 257: 28-32.

Herb A, Burnashev N, Werner P, Sakmann B, Wisden W, Seeburg PH. (1992). The KA-2 subunit of excitatory amino acid receptors shows widespread expression in brain and forms ion channels with distantly related subunits. Neuron 8: 775-785.

Hille B (2001). Ion Channels of Excitable Membranes (3rd ed.). Sunderland, Mass: Sinauer Associates, Inc. p. 5.

Hogg RC, Buisson B, Bertrand D (2005). Allosteric modulation of ligand-gated ion channels. Biochem Pharmacol 70: 1267-1276.

Hollmann M, Hartley M, Heinemann S (1991). Ca^{2+} permeability of KA-AMPA gated glutamate receptor channels depends on subunit composition. Science 252: 851-853.

Hollmann M, Heinemann S (1994). Cloned glutamate receptors. Annu Rev Neurosci 17: 31-108.

Hollmann M, Maron C, Heinemann S (1994). N-glycosylation site tagging suggests a three transmembrane domain topology for the glutamate receptor GluR1. Neuron 13: 1331-1343.

Hollmann M, O'Shea-Greenfield A, Rodgers SW, Heinemann S (1989). Cloning by functional expression of a member of the glutamate receptor family. Nature 342: 643-648.

Horning MS, Mayer ML (2004). Regulation of AMPA receptor gating by ligand binding core dimers. Neuron 41: 379-388.

Inanobe A, Furukawa H, Gouaux E (2005). Mechanism of partial agonist action at the NR1 subunit of NMDA receptors. Neuron 47: 71-84.

Isaac JT, Ashby MC, McBain CJ (2007). The role of the GluR2 subunit in AMPA receptor function and synaptic plasticity. Neuron 54: 859-871.

Jamain S, Betancur C, Quach H, Philippe A, Fellous M, Giros B, et al. (2002). Linkage and association of the glutamate receptor 6 gene with autism. Mol Psych 7: 302.

Jane DE, Lodge D, Collingridge GL (2009). Kainate receptors: pharmacology, function and therapeutic potential. Neuropharmacol 56: 90-113.

Jansen M, Dannhardt G (2003). Antagonists and agonists at the glycine site of the NMDAR for therapeutic interventions. Eur J Med Chem 38: 661-670.

Jasti, J, Furukawa H, Gonzales EB, Gouaux E (2007). Structure of acid-sensing ion channel 1 at 1.9 Å resolution and low pH. Nature 449: 316-323.

Jiang Y, Lee A, Chen J, Cadene M, Chait BT, MacKinnon R (2002). The open pore conformation of potassium channels. Nature 417: 523-526.

Jin R, Banke TG, Mayer ML, Traynelis SF, Gouaux E (2003). Structural basis for partial agonist action at ionotropic glutamate receptors. Nat Neurosci 6: 803-810.

Jin R, ClarkS, Weeks AM, Dudman JT, Gouaux E, Partin KM (2005). Mechanism of positive allosteric modulators acting on AMPA receptors. J Neurosci 25: 9027-9036.

Jin R, Singh SK, Gu S, Furukawa H, Sobolevsky AI, Zhou J, et al. (2009). Crystal structure and association behaviour of the GluR2 amino-terminal domain. EMBO J 28: 1812-1823.

Johnson JW, Ascher P (1987). Glycine potentiates the NMDA response in cultured mouse brain neurons. Nature 325: 529-531.

Jonas P 2000. The time course of signaling at central glutamatergic synapses. News Physiol Sci 15: 83-89.

Jonas P, Sakmann B (1992). Glutamate receptor channels in isolated patches from CA1 and CA3 pyramidal cells of rat hippocampal slices. J Physiol 455: 143-171.

Jones KS, VanDongen HM, VanDongen AM (2002). The NMDA receptor M3 segment is a conserved transduction element coupling ligand binding to channel opening. J Neurosci 22: 2044-2053.

Kamiya H, Ozawa S (2000). Kainate receptor-mediated presynaptic inhibition at the mouse hippocampal mossy fibre synapse. J Physiol 523: 653-665.

Karakas E, Simorowski N, Furukawa H (2009). Structure of the zinc-bound amino-terminal domain of the NMDA receptor NR2B subunit. EMBO J 28: 3910-3920.

Karakas E, Simorowski N, Furukawa H (2011). Subunit arrangement and phenylethanolamine binding in GluN1/GluN2B NMDA receptors. Nature 475: 249-253.

Kawahara Y, Ito K, Sun H, Kanazawa I, Kwak S (2003). Low editing efficiency of GluR2 mRNA is associated with low relative abundance of ADAR2 mRNA in white matter of normal human brain. Eur J Neurosci 18: 23-33.

Keinänen K, Wisden W, Sommer B, Werner P, Herb A, Verdoorn TA, et al. (1990). A family of AMPA-selective glutamate receptors. Science 24: 556-560.

Kemp JA, McKernan RM (2002). NMDAR pathways as drug targets. Nat Neurosci 5: 1039-1042.

Kenakin T, Miller LJ (2010). Seven transmembrane receptors as shapeshifting proteins: the impact of allosteric modulation and functional selectivity on new drug discovery. Pharmacol Rev 62: 265-304.

Kendrew JC, Bodo G, Dintzis HM, Parrish RG, Wyckoff H, Phillips DC (1958). A three-dimensional model of the myoglobin molecule obtained by X-ray analysis. Nature 181: 662-666.

Kennedy MB (1997). The postsynaptic density at glutamatergic synapses. Trends Neurosci 20: 264-268.

Kim S, Kim JH, Park M, Cho IH, Yoo HJ (2007). Family-based association study between GRIK2 polymorphisms and autism spectrum disorders in the Korean trios. Neurosci Res 58: 332-335.

King AE, Lopez-Garcia JA, Cumberbatch M (1992). Antagonism of synaptic potentials in ventral horn neurones by 6-cyano-7-nitroquinoxaline-2,3-dione: a study in the rat spinal cord in vitro. Br J Pharmacol 107: 375-381.

Kirat KE, Dupres V, Dufrêne YF (2008). Blistering of supported lipid membranes induced by phospholipase D, as observed by real-time atomic force microscopy. Biochim Biophys Acta 1778: 276-282.

Kohda K, Wang Y, Yuzaki M (2000). Mutation of a glutamate receptor motif reveals its role in gating and delta2 receptor channel properties. Nat Neurosci 3: 315-322.

Koike M, Tsukada S, Tsuzuki K, Kijima H, Ozawa S. (2000) Regulation of kinetic properties of GluR2 AMPA receptor channels by alternative splicing. J Neurosci 20: 2166-2174.

Korinthenberg R, Bukart P, Woefle C, Moenting JS, Ernst JP (2007). Pharmacology, efficacy and tolerability of potassium bromide in childhood Epilepsy. J Child Neurol 22: 414-418.

Kornblihtt AR, Schor IE, Alló M, Dujardin G, Petrillo E, Muñoz MJ (2013). Alternative splicing: a pivotal step between eukaryotic transcription and translation. Nat Rev Mol Cell Biol 14: 153-165.

Krupp JJ, Vissel B, Heinemann SF, Westbrook GL (1996). Calcium-dependent inactivation of recombinant N-methyl-D-aspartate receptors is NR2 subunit specific. Mol Pharmacol 50: 1680-1688.

Kucik DF, Elson EL, Sheetz MP (1999). Weak dependence of mobility of membrane protein aggregates on aggregate size supports a viscous model of retardation of diffusion. Biophys J 76: 314-322.

Kumar J, Schuck P, Jin R, Mayer ML (2009). The N-terminal domain of GluR6-subtype glutamate receptor ion channels. Nat Struct Mol Biol 16: 631-638.

Kusama N, Harding AM, Benson CJ (2010). Extracellular chloride modulates the desensitization kinetics of acid-sensing ion channel 1a (ASIC1a). J Biol Chem 285: 17425-17431.

Kuusinen, A, Arvola M, Keinanen K (1995). Molecular dissection of the agonist binding site of an AMPA receptor. EMBO J 14: 6327-6332.

Kwak S, Hideyama T, Yamashita, T, Aizawa H (2010). AMPA receptor mediated neuronal death in sporadic ALS. Neuropathol 30: 182-188.

Kwak S, Kawahara Y (2005). Deficient RNA editing of GluR2 and neuronal death in amyotropic lateral sclerosis. J Mol Med 83: 110-120.

Kwak S, Weiss JH (2006). Calcium permeable AMPA channels in neurodegenerative disease and ischemia. Curr Opin Neurobiol 16: 281-287.

Lauri SE, Segerstråle M, Vesikansa A, Maingret F, Mulle C, Collingridge GL, et al. (2005). Endogenous activation of kainate receptors regulates glutamate release and network activity in the developing hippocampus. J Neurosci 25: 4473-4484.

Lauri SE, Vesikansa A, Segerstråle M, Collingridge GL, Isaac JT, Taira T (2006). Functional maturation of CA1 synapses involves activity-dependent loss of tonic kainate receptor-mediated inhibition of glutamate release. Neuron 50: 415-429.

Lawrence JJ, Brenowitz S, Trussell LO (2003). The mechanism of action of aniracetam at synaptic α-amino-3-hydroxy-5-methyl-4-isoxazolepropionic acid (AMPA) receptors: indirect and direct effects on desensitization. Mol Pharmacol 64: 269-278.

Lerma J, Paternain AV, Rodríguez-Moreno A, López-García JC (2001). Molecular physiology of kainate receptors. Physiol Rev 81: 971-998.

Lesoil C, Nonaka T, Sekiguchi H, Osada T, Miyata M, Afrin R, et al. (2010). Molecular shape and binding force of *Mycoplasma mobile*'s leg protein Gli349 revealed by an AFM study. Biochem Biophys Research Commun 391: 1312-1317.

Lester RA, Clements JD, Westbrook GL, Jahr CE (1990). Channel kinetics determine the time course of NMDA receptor-mediated synaptic currents. Nature 346: 565-567.

Lewis BA, Engelman DM (1983). Lipid bilayer thickness varies linearly with acyl chain length in fluid phosphatidylcholine vesicles. J Mol Biol 166: 211-217.

Liao Y, Yuan Q, Torres J, Tam JP, Liu DX (2006). Biochemical and functional characterization of the membrane association and membrane permeabilizing activity of the severe acute respiratory syndrome coronavirus envelope protein. Virology 349: 264-275.

Lichtenberg D, Ahyayauch H, Alonso A, Goñi FM (2013). Detergent solubilization of lipid bilayers: a balance of driving forces. Trends Biochem Sci 38: 85-93.

Liu SJ, Zukin RS (2007). Ca^{2+} permeable AMPA receptors in synaptic plasticity and neuronal death. Trends Neurosci 30: 126-134.

Long SK, Smith DA, Siarey RJ, Evans RH (1990). Effect of 6-cyano-2,3-dihydroxy-7-nitro-quinoxaline (CNQX) on dorsal root-, NMDA-, kainate- and quisqualate-mediated depolarization of rat motoneurones in vitro. Br J Pharmacol 100: 850-854.

Loy C, Schneider L (2006). Galantamine for Alzheimer's disease and mild cognitive impairment. Cochrane Database Syst Rev 25: CD001747.

Madden DR (2002). The structure and function of glutamate receptor ion channels. Nat Rev Neurosci 3: 91-101.

Mah SJ, Cornell E, Mitchell NA, Fleck MW (2005). Glutamate receptor trafficking: endoplasmic reticulum quality control involves ligand binding and receptor function. J Neurosci 25: 2215-2225.

Maragos WF, Penney JB, Young AB (1988). Anatomic correlation of NMDA and ^{3}H-TCP-labeled receptors in rat brain. J Neurosci 8: 493-501.

Marchal C, Mulle C (2004). Postnatal maturation of mossy fibre excitatory transmission in mouse CA3 pyramidal cells: a potential role for kainate receptors. J Physiol 561: 27-37.

Mari SA, Pessoa J, Altieri S, Hensen U, Thomas L, Morais-Cabral JH, Müller DJ (2011). Gating of the MlotiK1 potassium channel involves large rearrangements of the cyclic nucleotide-binding domains. Proc Natl Acad Sci USA 108: 20802-20807.

Marquez-Klaka B, Rettinger J, Bhargava Y, Eisele T, Nicke A (2007). Identification of an intersubunit cross-link between substituted cysteine residues located in the putative ATP binding site of the P2X1 receptor. J Neurosci 27: 1456-1466.

Marsh D (2001). Polarity and permeation profiles in lipid membranes. Proc Natl Acad Sci USA 98: 7777-7782.

Marsh D (2002). Membrane water-penetration profiles from spin labels. Eur Biophys J 31: 559-562.

Mayer ML (2005). Glutamate receptor ion channels. Curr Opin Neurobiol 15: 282-288.

Mayer ML (2011). Emerging models of glutamate receptor ion channel structure and function. Structure 19: 1370-1380.

Mayer ML, Ghosal A, Dolman NP, Jane DE (2006). Crystal structures of the kainate receptor GluR5 ligand binding core dimer with novel GluR5-selective antagonists. J Neurosci 26: 2852-2861.

Mayer ML, Westbrook GL, Guthrie PB (1984). Voltage dependent block by Mg^{2+} of NMDA responses in spinal cord neurones. Nature 309: 261-263.

Meldrum B, Garthwaite J (1990). Excitatory amino acid neurotoxicity and neurodegenerative disease. Trends Pharmacol Sci 11: 379-387.

Meyerson JR, Kumar J, Chittori S, Rao P, Pierson J, Bartesaghi A, et al. (2014). Structural mechanism of glutamate receptor activation and desensitization. Nature 514: 328-334.

Midgett CR, Madden DR (2008). The quaternary structure of a calcium permeable AMPA receptor: conservation of shape and symmetry across functionally distinct subunit assemblies. J Mol Biol 382: 578-584.

Missale C, Fiorentini C, Busi C, Collo G, Spano PF (2006). The NMDA/D1 receptor complex as a new target in drug development. Curr Topics Med Chem 6: 801-808.

Mitra K, Ubarretxena-Belandia I, Taguchi T, Warren G, Engelman DM (2004). Modulation of the bilayer thickness of exocytic pathway membranes by membrane proteins rather than cholesterol. Proc Natl Acad Sci USA 101: 4083-4088.

Monaghan DT, Jane DE (2009). Pharmacology of NMDA Receptors. In: Van Dongen AM, editor. Biology of the NMDA Receptor. Boca Raton (FL): CRC Press/Taylor & Francis, Chapter 12.

Monyer H, Burnashev N, Laurie DJ, Sakmann B, Seeburg PH (1994). Developmental and regional expression in the rat brain and functional properties of four NMDA receptors. Neuron 12: 529-540.

Mosbacher J, Schoepfer R, Monyer H, Burnashev N, Seeburg PH, Ruppersber JP (1994). A molecular determinant for sub millisecond desensitization in glutamate receptors. Science 266: 1059-1062.

Motazacker MM, Rost BR, Hucho T, Garshasbi M, Kahrizi K, Ullmann R, et al. (2007). A defect in the ionotropic glutamate receptor 6 gene (GRIK2) is associated with autosomal recessive mental retardation. Am J Human Genet 81: 792-798.

Mothet JP, Parent AT, Wolosker H, Brady RO Jr, Linden DJ, Ferris CD, et al. (2000). D-serine is an endogenous ligand for the glycine site of the N-methyl-D-aspartate receptor. Proc Natl Acad Sci USA 97: 4926-4931.

Mulle C, Sailer A, Pérez-Otaño I, Dickinson-Anson H, Castillo PE, Bureau I, et al. (1998). Altered synaptic physiology and reduced susceptibility to kainate-induced seizures in GluR6-deficient mice. Nature 392: 601-605.

Müller D J, Sass HJ, Muller S, Büldt G, Engel A. (1999). Surface structures of native bacteriorhodopsin depend on the molecular packing arrangement in the membrane. J Mol Biol 285: 1903-1909.

Müller DJ (2008). AFM: A nanotool in membrane biology. Biochemistry 47: 7986-7998.

Müller DJ, Baumeister W, Engel AJ (1996). Conformational change of the hexagonally packed intermediate layer of *Deinococcus radiodurans* monitored by atomic force microscopy. J Bacteriol 178: 3025-3030.

Müller DJ, Engel A (1999). Voltage and pH-induced channel closure of porin OmpF visualized by atomic force microscopy. J Mol Biol 285: 1347-1351.

Müller DJ, Engel A (2007). Atomic force microscopy and spectroscopy of native membrane proteins. Nat Protocols 2: 2191-2197.

Muto T, Tsuchiya D, Morikawa K, Jingami H (2007). Structures of the extracellular regions of the group II/III metabotropic glutamate receptors. Proc Natl Acad Sci USA 104: 3759-3764.

Nagle JF, Tristram-Nagle S (2000). Structure of lipid bilayers. Biochim Biophys Acta 1469: 159-195.

Nakagawa T (2011). The biochemistry, ultrastructure, and subunit assembly mechanism of AMPA receptors. Mol Neurobiol 42: 161-184.

Nakagawa T, Cheng Y, Ramm E, Sheng M, and Walz T (2005). Structure and different conformational states of native AMPA receptor complexes. Nature 433: 545-549.

Nakagawa T, Cheng Y, Sheng M, and Walz T (2006). Three-dimensional structure of an AMPA receptor without associated stargazin/TARP proteins. Biol Chem 387: 179-187.

Nakano K, Tozuka Y, Yamamoto H, Kawashima Y, Takeuchi H (2008). A novel method for measuring rigidity of submicron-size liposomes with atomic force microscopy. Int J Pharmaceutics 355: 203-209.

Naur P, Hansen KB, Kristensen AS, Dravid SM, Pickering DS, Olsen L, et al. (2007). Ionotropic glutamate-like receptor delta 2 binds D-serine and glycine. Proc Natl Acad Sci USA 104: 14116-14121.

Nayeem N, Zhang Y, Schweppe DK, Madden DR, Green T (2009). A nondesensitizing kainate receptor point mutant. Mol Pharmacol 76: 534-542.

Nielsen LK, Risbo J, Callisen T H, Bjørnholm T (1999). Lag-burst kinetics in phospholipase A_2 hydrolysis of DPPC bilayers visualized by atomic force microscopy. Biochim Biophys Acta 1420: 266-271.

Nimigean CM (2006). A radioactive uptake assay to measure ion transport across ion channel-containing liposomes. Nat Protocols 1: 1207-1212.

Nowak L, Bregestovski P, Ascher P, Herbet A, Prochiantz A (1984). Magnesium gates glutamate-activated channels in mouse central neurones. Nature 307: 462-465.

O'Neill MJ, Murray TK, Whalley K, Ward MA, Hicks CA, Woodhouse S, et al. (2004). Neurotrophic actions of the novel AMPA receptor potentiator, LY404187, in rodent models of Parkinson's disease. Eur J Pharmacol 486: 163-174.

Oesterhelt F, Oesterhelt D, Pfeiffer M, Engel A, Gaub HE, Müller DJ (2000). Unfolding pathways of individual bacteriorhodopsins. Science 288: 143-146.

Opella SJ, Marassi FM (2004). Structure determination of membrane proteins by NMR spectroscopy. Chem Rev 104: 3587-3606.

Ostermeier C, Michel H (1997). Crystallization of membrane proteins. Curr Opin Struct Biol 7: 697-701.

Palmada M, Centelles JJ (1998). Excitatory amino acid neurotransmission. Pathways for metabolism, storage and reuptake of glutamate in brain. Front Biosci 3: d701-718.

Paoletti P (2011). Molecular basis of NMDA receptor functional diversity. Eur J Neurosci 33: 1351-1365.

Parot P, Dufrêne YF, Hinterdorfer P, LeGrimellec C, Navajas D, Pellequer JL, Scheuring S (2007). Past, present and future of atomic force microscopy in life sciences and medicine, J Mol Recognit 20: 418-431.

Partin KM, Bowie D, Mayer ML (1995). Structural determinants of allosteric regulation in alternatively spliced AMPA receptors. Neuron 14: 833-843.

Partin KM, Fleck MW, Mayer ML (1996). AMPA receptor flip/flop mutants affecting deactivation, desensitization, and modulation by cyclothiazide, aniracetam, and thiocyanate. J Neurosci. 16: 6634-6647.

Partin KM, Patneau DK, Mayer ML (1994). Cyclothiazide differentially modulates desensitization of alpha-amino-3-hydroxy-5-methyl-4-isoxazolepropionic acid receptor splice variants. Mol Pharmacol 46: 129-138.

Pasternack A, Coleman SK, Fethiere J, Madden DR, LeCaer JP, Rossier J, et al. (2003). Characterization of the functional role of the N-glycans in the AMPA receptor ligand-binding domain. J Neurochem 84: 1184-1192.

Pasternack A, Coleman SK, Jouppila A, Mottershead DG, Lindfors M, Pasternack M, Keinanen K (2002). Alpha-amino-3-hydroxy-5-methyl-4-isoxazolepropionic acid (AMPA) receptor channels lacking the N-terminal domain. J Biol Chem 277: 49662-49667.

Paternain AV, Morales M, Lerma J (1995). Selective antagonism of AMPA receptors unmasks kainate receptor-mediated responses in hippocampal neurons. Neuron 14: 185-189.

Paternostre MT, Roux M, Rigaud JL (1988). Mechanisms of membrane protein insertion into liposomes during reconstitution procedures involving the use of detergents. 1. Solubilization of large unilamellar liposomes (prepared by reverse-phase evaporation) by triton X-100, octyl glucoside, and sodium cholate. Biochemistry 27: 2668-2677.

Patneau DK, Vyklicky L Jr, Mayer ML (1993). Hippocampal neurons exhibit cyclothiazide-sensitive rapidly desensitizing responses to kainate. J Neurosci 13: 3496-3509.

Pawson T, Scott JD (1997). Signaling through scaffold, anchoring, and adaptor proteins. Science 278: 2075-2080.

Pearce JM. (2002). Bromide, the first effective antiepileptic agent. J Neurol Neurosurg Psychiatry 72: 412

Pedersen SE, Cohen JB (1990). d-Tubocurarine binding sites are located at a-g and a-d subunit interfaces of the nicotinic acetylcholine receptors. Proc Natl Acad Sci USA 87: 2785-2789.

Penn AC, Williams SR, Greger IH (2008). Gating motions underlie AMPA receptor secretion from the endoplasmic reticulum. EMBO J 27: 3056-3068.

Pickard BS, Malloy MP, Christoforou A, Thomson PA, Evans KL, Morris SW, et al. (2006). Cytogenetic and genetic evidence supports a role for the kainate-type glutamate receptor gene, GRIK4, in schizophrenia and bipolar disorder. Mol Psych 11: 847-857.

Plested AJR, Mayer ML (2009). AMPA receptor ligand binding domain mobility revealed by functional cross linking. J Neurosci 29: 11912-11923.

Priel A, Selak S, Lerma J, Stern-Bach Y (2006). Block of kainate receptor desensitization uncovers a key trafficking checkpoint. Neuron 52: 1037-1046.

Purves D, Augustine GJ, Fitzpatrick D, Hall WC, LaMantia AS, McNamara JO, White LE (2008). Neuroscience, 4th ed. Sunderland, Massachusetts: Sinauer Associates, Inc.

Quirk JC, Nisenbaum ES (2003). Multiple molecular determinants for allosteric modulation of alternatively spliced AMPA receptors. J Neurosci 23: 10953-10962.

Quirk JC, Siuda ER, Nisenbaum ES (2004). Molecular determinants responsible for differences in desensitization kinetics of AMPA receptor splice variants. J Neurosci 24: 11416-11420.

Rachline J, Perin-Dureau F, Le Goff A, Neyton J, Paoletti P (2005). The micromolar zinc-binding domain on the NMDA receptor subunit NR2B. J Neurosci 25: 308-317.

Ramachandran GN, Ramakrishnan C, Sasisekharan V (1963). Stereochemistry of polypeptide chain configurations. J Mol Biol 7: 95-99.

Rawicz W, Olbrich KC, McIntosh T, Needham D, Evans E (2000). Effect of chain length and unsaturation on elasticity of lipid bilayers. Biophys J 79: 328-339.

Riedel G, Platt B, Micheau J (2003). Glutamate receptor function in learning and memory. Behav Brain Res 140: 1-47.

Rigaud JL, Levy D (2003). Reconstitution of membrane proteins into liposomes. Meth Enzymol 372: 65-86.

Rigaud JL, Pitard B, Levy D (1995). Reconstitution of membrane proteins into liposomes: application to energy-transducing membrane proteins. Biochim Biophys Acta 1231: 223-246.

Robert A, Armstrong N, Gouaux JE, Howe JR (2005). AMPA receptor binding cleft mutations that alter affinity, efficacy, and recovery from desensitization. J Neurosci 25: 3752-3762.

Rodríguez-Moreno A, Herreras O, Lerma J (1997). Kainate receptors presynaptically downregulate GABAergic inhibition in the rat hippocampus. Neuron 19: 893-901.

Rogers SW, Hughes TE, Hollmann M, Gasic GP, Deneris ES, Heinemann S (1991). The characteriation and localization of the glutamate receptor subunit GluR1 in the rat brain. J Neurosci 11: 2713-2724.

Rothman SM, Olney JW (1987). Excitotoxicity and the NMDA receptor. Trends Neurosci 10: 299-302.

Ruan Y, Miyagi A, Wang X, Chami M, Boudker O, Scheuring S (2017). Direct visualization of glutamate transporter elevator mechanism by high-speed AFM. Proc Natl Acad Sci USA 114: 1584-1588.

Safferling M, Tichelaar W, Kümmerle G, Jouppila A, Kuusinen A, Keinänen K, Madden DR (2001) First images of a glutamate receptor ion channel: oligomeric state and molecular dimensions of GluRB homomers. Biochemistry 40: 13948-13953.

Sampaio AS, Fagerness J, Crane J, Leboyer M, Delorme R, Pauls DL, Stewart SE (2011). Association between polymorphisms in GRIK2 gene and obsessive-compulsive disorder: a family-based study. CNS Neurosci Therap 17: 141-147.

Santos S, Barcons V, Christenson HK, Josep F, Neil H. Thomson NH (2011). The intrinsic resolution limit in the atomic force microscope: implications for heights of nano-scale features. PLoS ONE 6:: e23821.

Schiffer H, Heinemann S (2007). Association of the human kainate receptor GluR7 gene (GRIK3) with recurrent major depressive disorder. Am J Med Genet Part B: Neuropsychiatric Genet 144: 20-26.

Schneider S, Lärmer J, Henderson R, Oberleithner H (1998). Molecular weights of individual proteins correlate with molecular volumes measured by atomic force microscopy. Pflügers Archiv 435: 362-367.

Seddon AM, Curnow P, Booth PJ (2004). Membrane proteins, lipids and detergents: not just a soap opera. Biochim Biophys Acta 1666: 105-117.

Shen H-H, Lithgow T, Martin L (2013). Reconstitution of membrane proteins into model membranes: seeking better ways to retain protein activities. Int J Mol Sci 14: 1589-1607.

Shibata M, Yamashita H, Uchihashi T, Kandori H, Ando T (2010). High-speed atomic force microscopy shows dynamic molecular processes in photo activated bacteriorhodopsin. Nat Nanotechnol 5: 208-212.

Shinozaki Y, Sumitomo K, Tsuda M, Koizumi S, Inoue K, Torimitsu K (2009). Direct observation of ATP-induced conformational changes in single P2X4 receptors. PLoS Biol 7: e1000103.

Shuang M, Liu J, Jia MX, Yang JZ, Wu SP, Gong XH, et al. (2004). Family-based association study between autism and glutamate receptor 6 gene in Chinese Han trios. Am J Med Genet Part B: Neuropsychiatric Genet 131: 48-50.

Singleton P (1999). Bacteria in Biology, Biotechnology and Medicine (5th ed.). New York: Wiley.

Skotheim RI, Nees M (2007). Alternative splicing in cancer: noise, functional, or systematic? Int J Biochem Cell Biol 39: 1432-1449.

Smith TC, Howe JR (2000). Concentration-dependent substate behaviour of native AMPA receptors. Nat Neurosci 3: 992-997.

Smolders I, Bortolotto ZA, Clarke VR, Warre R, Khan GM, O'Neill MJ, et al. (2002). Antagonists of GLUK5-containing kainate receptors prevent pilocarpine-induced limbic seizures. Nat Neurosci 5: 796-804.

Sobolevsky AI, Rosconi MP, Gouaux E (2009). X-ray structure, symmetry and mechanism of an AMPA-subtype glutamate receptor. Nature 462: 745-756.

Sommer B, Keinanen K, Verdoorn TA, Wisden W, Burnashev N, Herb A, et al. (1990). Flip and flop: a cell specific functional switch in glutamate operated channels of the CNS. Science 249: 1580-1585.

Sommer B, Köhler M, Sprengel R, Seeburg PH (1991). RNA editing in brain controls a determinant of ion flow in glutamate gated channels. Cell 67: 11-19.

Stamm S, Ben-Ari S, Rafalska I, Tang Y, Zhang Z, Toiber D, Thanaraj TA, Soreq H (2005). Function of alternative splicing. Gene 344: 1-20.

Standley S, Baudry M (2000). The role of glycosylation in ionotropic glutamate receptor ligand binding, function, and trafficking. Cell Mol Life Sci 57: 1508-1516.

Stern-Bach Y, Bettler B, Hartley M, Sheppard PO, O'Hara PJ, Heinemann SF (1994) Agonist selectivity of glutamate receptors is specified by two domains structurally related to bacterial amino acid-binding proteins. Neuron 13:1345-1357.

Stern-Bach Y, Russo S, Neuman M, Rosenmund CA (1998). Point mutation in the glutamate binding site blocks desensitization of AMPA receptors. Neuron 21: 907-918.

Stewart AP, Haerteis S, Diakov A, Korbmacher C, Edwardson JM (2011). Atomic force microscopy reveals the architecture of the epithelial sodium channel (ENaC). J Biol Chem 286: 31944-31952.

Straub C, Hunt DL, Yamasaki M, Kim KS, Watanabe M, Castillo PE, Tomita S (2011). Distinct functions of kainate receptors in the brain are determined by the auxiliary subunit Neto1. Nature Neurosci 14: 866-873.

Sun Y, Olson R, Horning M, Armstrong N, Mayer M, Gouaux E (2002). Mechanism of glutamate receptor desensitization. Nature 417: 245-53.

Sutcliffe MJ, Wo ZG, Oswald RE (1996). Three-dimensional models of non-NMDA glutamate receptors. Biophys J 70: 1575-1589.

Suzuki Y, Goetze TA, Stroebel D, Balasuriya D, Yoshimura SH, Henderson RM, et al. (2013). Visualization of structural changes accompanying activation of N-methyl-D-aspartate (NMDA) receptors using fast-scan atomic force microscopy imaging. J Biol Chem 288: 778-784.

Suzuki Y, Higuchi Y, Hizume K, Yokokawa M, Yoshimura SH, Yoshikawa K, et al. (2010). Molecular dynamics of DNA and nucleosomes in solution studied by fast-scanning atomic force microscopy. Ultramicroscopy 110: 682-688.

Swartz KJ (2004). Towards a structural view of gating in potassium channels. Nat Rev Neurosci 5: 905-916.

Teague EC, Scire FE, Baker SM, Jensen SW (1982). Three-dimensional stylus profilometry. Wear 83: 1-12.

Tian M, Ye S (2016). Allosteric regulation in NMDA receptors revealed by the genetically encoded photo-cross-linkers. Sci Rep 6, 34751.

Tichelaar W, Safferling M, Keinänen K, Stark H, Madden DR (2004). The three-dimensional structure of an ionotropic glutamate receptor reveals a dimer-of-dimers assembly. J Mol Biol 344: 435-442.

Tomiyama M, Rodríguez-Puertas R, Cortés R, Pazos A, Palacios JM, Mengod G (2002). Flip and flop splice variants of AMPA receptor subunits in the spinal cord of amyotrophic lateral sclerosis. Synapse 45: 245-9.

Trauble H, Haynes DH (1971). The volume change in lipid bilayer lamellae at the crystalline-liquid crystalline phase transition. Chem Phys Lipids 7: 324-335.

Traynelis SF, Wollmuth LP, McBain CJ, Menniti FS, Vance KM, Ogden KK, et al. (2010). Glutamate receptor ion channels: structure, regulation, and function. Pharmacol Rev 62: 405-496.

Valluru L, Xu J, Zhu Y, Yan S, Contractor A, Swanson GT (2005). Ligand binding is a critical requirement for plasma membrane expression of heteromeric kainate receptors. J Biol Chem 280: 6085-6093.

Vignes M, Collingridge GL (1997). The synaptic activation of kainate receptors. Nature 388: 179-182.

Vissel B, Royle G, Christie B, Schiffer H, Ghetti A, Tritto T, et al. (2001). The role of RNA editing of kainate receptors in synaptic plasticity and seizures. Neuron 29: 217-227.

Wahl MC, Will CL, Luhrmann R (2009). The spliceosome: design principles of a dynamic RNP machine. Cell 136: 701-718.

Wallin E, von Heijne G (1998). Genome-wide analysis of integral membrane proteins from eubacterial, archaen, and eukaryotic organisms. Protein Sci 7: 1029-1038.

Watkins JC, Jane DE (2006). The glutamate story. Br J Pharmacol 147 Suppl 1: S100-108.

Wenthold RJ, Petralia RS, Blahos JI, Niedzielski AS (1996). Evidence for multiple AMPA receptor complexes in hippocampal CA1/CA2 neurons. J Neurosci 16: 1982-1989.

Werner P, Voigt M, Keinänen K, Wisden W, Seeburg PH (1991). Cloning of a putative high-affinity kainate receptor expressed predominantly in hippocampal CA3 cells. Nature 351: 742-744.

Weston MC, Gertler C, Mayer ML, Rosenmund C (2006). Interdomain interactions in AMPA and kainate receptors regulate affinity for glutamate. J Neurosci 26: 7650-7658.

White S (2017). Membrane proteins of known 3D structure. Retrieved from http://blanco.biomol.uci.edu/mpstruc/.

Whited AM, Park PS (2014). Atomic force microscopy: A multifaceted tool to study membrane and their interactions with ligands. Biochim Biophys Acta 1838: 56-68.

Wilding TJ, Huettner JE (1996). Antagonist pharmacology of kainate- and alpha-amino-3-hydroxy-5-methyl-4-isoxazolepropionic acid-preferring receptors. Mol Pharmacol 49: 540-546.

Williams K (2009). Extracellular Modulation of NMDA Receptors. In: Van Dongen AM, ed. Biology of the NMDA Receptor. Boca Raton (FL): CRC Press/Taylor & Francis, Chapter 11.

Wood PL (2005). The NMDAR complex: a long and winding road to therapeutics. IDrugs 8: 229-235.

Wright A, Vissel B (2012). The essential role of AMPA receptor GluA2 subunit RNA editing in the normal and diseased brain. Frontiers Mol Neurosci 5: 34.

Wyllie DJ, Béhé P, Colquhoun D (1998). Single-channel activations and concentration jumps: comparison of recombinant NR1a/NR2A and NR1a/NR2D NMDA receptors. J Physiol 510: 1-18.

Yamada KA, Tang CM (1993). Benzothiadiazides inhibit rapid glutamate receptor desensitization and enhance glutamatergic synaptic currents. J Neurosci 13: 3904-3915.

Yao Y, Harrison CB, Freddolino PL, Schulten K, Mayer ML (2008). Molecular mechanism of ligand recognition by NR3 subtype glutamate receptors. EMBO J 27: 2158-2170.

Yellen G (2002). The voltage-gated potassium channels and their relatives. Nature 419: 35-42.

Yokokawa M, Carnally SM, Henderson RM, Takeyasu K, Edwardson JM (2010). Acid-sensing ion channel (ASIC) 1a undergoes a height transition in response to acidification. FEBS Lett 584: 3107-3110.

Yokokawa M, Takeyasu K (2011). Motion of the Ca^{2+}-pump captured. FEBS J 278: 3025-3031.

Yokokawa M, Wada C, Ando T, Sakai N, Yagi A, Yoshimura SH, Takeyasu K (2006). Fast-scanning atomic force microscopy reveals the ATP/ADP-dependent conformational changes of GroEL. EMBO J 25: 4567-4576.

Yonkunas M, Kurnikova M (2011) Characterizing the energetic states of the GluR2 ligand binding domain core-dimer. Biophys J 100: L5-7.

Yuan H, Erreger K, Dravid SM, Traynelis SF (2005). Conserved structural and functional control of N-methyl-D-aspartate receptor gating by transmembrane domain M3. J Biol Chem 280: 29708-29716.

Yuan H, Hansen KB, Vance KM, Ogden KK, Traynelis SF (2009). Control of NMDA receptor function by the NR2 subunit amino-terminal domain. J Neurosci 29: 12045-12058.

Zaccara G, Giovannelli F, Cincotta M, Iudice A (2013). AMPA receptor inhibitors for the treatment of epilepsy: the role of perampanel. Expert Rev Neurother 13: 647-55.

Zhang W, St-Gelais F, Grabner CP, Trinidad JC, Sumioka A, Morimoto-Tomita M, et al. (2009). A transmembrane accessory subunit that modulates kainate-type glutamate receptors. Neuron 61: 385-396.

Zhang Z, Lotti F, Dittmar K, Younis I, Wan L, Kasim M, Dreyfuss G (2008). SMN deficiency causes tissue-specific perturbations in the repertoire of snRNAs and widespread defects in splicing. Cell 133: 585-600.

Zhou Y, Morais-Cabral JH, Kaufman A, MacKinnon R (2001) Chemistry of ion coordination and hydration revealed by a K^+ channel-Fab complex at 2.0 Å resolution. Nature 414: 43-48.